Material and technique development for ultrasound optical tomography using spectral hole burning filters

Bengtsson, Alexander

2022

Document Version:
Publisher's PDF, also known as Version of record

Material and technique development for ultrasound optical tomography using spectral hole burning filters

ALEXANDER BENGTSSON
FACULTY OF ENGINEERING | LUND UNIVERSITY

Material and technique development for ultrasound optical tomography using spectral hole burning filters

Material and technique development for ultrasound optical tomography using spectral hole burning filters

by Alexander Bengtsson

LUND
UNIVERSITY

Thesis for the degree of Doctor of Philosophy
Thesis advisors: Prof. Stefan Kröll, Dr. Lars Rippe
Faculty opponent: Dr. Anne Louchet-Chauvet

To be presented, with the permission of the Faculty of Engineering of Lund University, for public criticism in the Rydberg lecture hall (Rydbergsalen) at the Department of Physics on Friday, the 20th of May 2022 at 9:15.

Organization
LUND UNIVERSITY
Division of Atomic Physics
Department of Physics
P.O. Box 118
SE–221 00 LUND, Sweden

Document name
DOCTORAL DISSERTATION
Date of disputation
2022-05-20
Sponsoring organization

Author(s)
Alexander Bengtsson

Title and subtitle
Material and technique development for ultrasound optical tomography using spectral hole burning filters

Abstract
The molecular sensitivity provided by optical photons has potential advantages in medical diagnostics, for example, in distinguishing healthy from cancerous tissue. However, scattering resulting from inhomogeneities in the refractive index of tissues prevents spatially resolved optical measurements in biological material, except at very shallow depths. This thesis presents research on a medical imaging technique called ultrasound optical tomography (UOT), which overcomes the limit on resolution resulting from scattering by combining photons and ultrasound. Photons are locally frequency shifted (tagged) by ultrasonic waves inside the tissue. Optical contrast can be obtained with ultrasonic spatial resolution by detecting these tagged photons. In this work, the tagged photons were detected using narrowband optical passband filters created in rare-earth-ion-doped crystals using spectral hole burning techniques.

The thesis presents UOT measurements using Pr^{3+}:Y_2SiO_5 filters operating at 606 nm, which characterize the signal strength under various well-controlled experimental conditions. Improved understanding of the performance of an optimized UOT set-up based on spectral hole burning was obtained by fitting experimental data with theoretical models, indicating that imaging depths of several centimetres should be possible in biological tissues.

A theoretical comparison of the many UOT methods described in the literature is presented. The findings indicate that spectral hole burning filters may have better contrast-to-noise scaling, and thus potentially greater imaging depths, than other UOT methods such as digital off-axis holography, photorefractive holography, and speckle contrast imaging.

A major challenge for spectral-hole-burning filter-based UOT to become useful for *in vivo* applications, is to identify and develop crystals capable of supporting the required high-contrast filters at wavelengths within the optical window for tissue ($\sim 650 - 950$ nm). Experimental values of the filter contrast obtained in UOT measurements in this wavelength range have so far been limited to 14 dB. Based on spectroscopic measurements, Tm^{3+}:LaF_3 is proposed as a candidate for UOT filtering at 690 and 797 nm. Measurements show that a filter contrast above 50 dB is possible at the 690 nm transition for a collimated laser beam. The high filter contrast of Tm^{3+}:LaF_3 is expected to be important for the future development of UOT using spectral hole burning filters.

Key words
Biomedical imaging, ultrasound optical tomography, acousto-optical tomography, rare-earth-ion-doped crystals, spectral hole burning, slow light filters, Tm^{3+}:LaF_3

Classification system and/or index terms (if any)

Supplementary bibliographical information
Language
English

ISSN and key title
0281-2762, Lund Reports on Atomic Physics, LRAP 580
ISBN
978-91-8039-224-2 (print)
978-91-8039-223-5 (pdf)

Recipient's notes
Number of pages
221
Price
Security classification

Signature 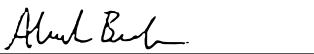 Date 2022-04-07

Material and technique development for ultrasound optical tomography using spectral hole burning filters

by Alexander Bengtsson

LUND
UNIVERSITY

A doctoral thesis at a university in Sweden takes either the form of a single, cohesive research study (monograph) or a summary of research papers (compilation thesis), which the licentiate student has written alone or together with one or several other author(s).

In the latter case the thesis consists of two parts. An introductory text puts the research work into context and summarizes the main points of the papers. Then, the research publications themselves are reproduced, together with a description of the individual contributions of the authors. The research papers may either have been already published or are manuscripts at various stages (in press, submitted, or in draft).

Funding information: This work has received financial support from several sources, but it has mainly and in particular received support from the Knut & Alice Wallenberg Foundation.

Department of Physics, Faculty of Engineering, Lund University

ISBN: 978-91-8039-224-2 (print)
ISBN: 978-91-8039-223-5 (pdf)
ISSN: 0281-2762
Lund Reports on Atomic Physics, LRAP 580 (2022)

Printed in Sweden by Media-Tryck, Lund University, Lund 2022

Contents

Abstract

The molecular sensitivity provided by optical photons has potential advantages in medical diagnostics, for example, in distinguishing healthy from cancerous tissue. However, scattering resulting from inhomogeneities in the refractive index of tissues prevents spatially resolved optical measurements in biological material, except at very shallow depths. This thesis presents research on a medical imaging technique called ultrasound optical tomography (UOT), which overcomes the limit on resolution resulting from scattering by combining photons and ultrasound. Photons are locally frequency shifted (tagged) by ultrasonic waves inside the tissue. Optical contrast can be obtained with ultrasonic spatial resolution by detecting these tagged photons. In this work, the tagged photons were detected using narrowband optical passband filters created in rare-earth-ion-doped crystals using spectral hole burning techniques.

The thesis presents UOT measurements using Pr^{3+}:Y_2SiO_5 filters operating at 606 nm, which characterize the signal strength under various well-controlled experimental conditions. Improved understanding of the performance of an optimized UOT set-up based on spectral hole burning was obtained by fitting experimental data with theoretical models, indicating that imaging depths of several centimetres should be possible in biological tissues.

A theoretical comparison of the many UOT methods described in the literature is presented. The findings indicate that spectral hole burning filters may have better contrast-to-noise scaling, and thus potentially greater imaging depths, than other UOT methods such as digital off-axis holography, photorefractive holography, and speckle contrast imaging.

A major challenge for spectral-hole-burning filter-based UOT to become useful for *in vivo* applications, is to identify and develop crystals capable of supporting the required high-contrast filters at wavelengths within the optical window for tissue ($\sim 650 - 950$ nm). Experimental values of the filter contrast obtained in UOT measurements in this wavelength range have so far been limited to 14 dB. Based on spectroscopic measurements, Tm^{3+}:LaF_3 is proposed as a candidate for UOT filtering at 690 and 797 nm. Measurements show that a filter contrast above 50 dB is possible at the 690 nm transition for a collimated laser beam. The high filter contrast of Tm^{3+}:LaF_3 is expected to be important for the future development of UOT using spectral hole burning filters.

List of publications

This thesis is based on the following publications, referred to by their Roman numerals:

I **Characterization and modeling of acousto-optic signal strengths in highly scattering media**
A. Bengtsson, D. Hill, M. Li, M. Di, M. Cinthio, T. Erlöv, S. Andersson-Engels, N. Reistad, A. Walther, L. Rippe, and S. Kröll
Biomedical Optics Express, 2019, 10(11), pp. 5565-5584

II **A simple experimental method for measuring the thermal sensitivity of single-mode fibers**
S. Bondza, A. Bengtsson, S. P. Horvath, A. Walther, S. Kröll, and L. Rippe
Review of Scientific Instruments, 2020, 91(10), pp. 105114

III **Acousto-optic interaction strengths in optically scattering media using high pressure acoustic pulses**
D. Hill, A. Bengtsson, T. Erlöv, M. Cinthio, and S. Kröll
Biomedical Optics Express, 2021, 12(6), pp. 3196-3213

IV **First principle simulation package for arbitrary acousto-optic interaction in scattering materials**
D. Hill, A. Bengtsson, T. Erlöv, M. Cinthio, and S. Kröll
in European Conferences on Biomedical Optics 2021 (ECBO), OSA Technical Digest (Optica Publishing Group, 2021), paper ES1C.6.

V **Suppression of Non-Radiative Relaxation in Tm^{3+}-doped Materials for Oxygenation-Sensitive Ultrasound-Optical Tomography**
A. D. Marsh, A. Bengtsson, P. J. T. Woodburn, L. Rippe, S. Kröll, C. W. Thiel, and R. L. Cone
Manuscript in preparation

VI **Comparison of contrast-to-noise ratios of different detection methods in ultrasound optical tomography**
A. Bengtsson, D. Hill, K. Shortiss, L. Rippe, and S. Kröll
Submitted manuscript

Acknowledgements

The research presented in this thesis would not have been possible without important contributions from many people. First, I would like to thank my main supervisor Stefan Kröll for the opportunity to do a Ph.D. project in the group, and for always having time to discuss and give valuable comments and guidance on my work. I would also like to thank my co-supervisor Lars Rippe for providing a lot of excellent input throughout my whole Ph.D. project, and for teaching me several things that will be useful in my future career. I would also like to express my gratitude to David Hill, with whom I have spent many hours in the lab. David has heavily contributed to all the UOT experiments, and a part of the spectroscopic investigations presented in this thesis. Kevin Shortiss has significantly contributed to both the UOT imaging and the high-contrast filter measurements, for which I'm grateful. I would like to thank Charles Thiel and Rufus Cone for inviting me to their lab at Montana State University for the initial Tm^{3+}:LaF_3 measurements. I am very pleased to have worked with Aaron Marsh and Tino Woodburn during my visit, which taught me a lot about how to do spectroscopy on rare-earth-ion-doped crystals, and the measurement results were important for the continuation of my Ph.D. work. I would also like to thank Aaron and Tino for being very friendly and showing me around Bozeman, Yellowstone, and other parts of Montana. I would like to thank Meng Li and Mengqiao Di, whose contributions were important to our first UOT measurements. They, together with Nina Reistad, also provided the recipe and characterization of the tissue-mimicking phantoms used throughout the present work. The expertise regarding everything related to ultrasound provided by Magnus Cinthio and Tobias Erlöv was greatly appreciated. So was the medical expertise provided by Emilie Krite Svanberg. I would like to thank Roger Macfarlane, and Yin Hang, for kindly providing Tm^{3+}:LaF_3 crystals for spectroscopic investigations. I'm also grateful to Saskia Bondza for the excellent work she did during her master's project that I co-supervised. Finally, I would also like to thank all the other members of the Quantum Information Group, both present and former: Andreas Walther, Mohammed Alqedra, Adam Kinos, Hafsa Syed, Chunyan Shi, Sebastian Horvath, Marcus Lindén, David Gustavsson, and Abdullah Abdelatief. All of you has provided useful comments and help at multiple stages of my work, and have also contributed to a pleasant work environment.

Populärvetenskaplig sammanfattning på svenska

Bildgivande tekniker inom medicinsk diagnostik som magnetisk resonanstomografi (MRI), röntgen, ultraljud, etc. är väldigt viktiga i dagens samhälle, och har bidragit till att öka både livslängden och livskvaliteten för många människor. Beroende på vilken vävnadstyp man vill avbilda, fungerar teknikerna olika bra, eftersom det är olika fysikaliska mekanismer som ger upphov till bildkontrasten. Tekniker som använder ljus har en molekulär kontrast som inte kan fås med andra tekniker, och har därför vissa fördelar. Till exempel, så är ljus väldigt bra för att detektera hemoglobinmolekylen i blodet, och är det stor skillnad på hur ljus interagerar med syresatt och icke syresatt hemoglobin. Det kan man bland annat använda för att skilja på frisk och cancersjuk vävnad. En teknik som använder ljus för att avbilda hjärnan skulle vara väldigt användbar för att öka vår förståelse för hur hjärnan fungerar, och för sjukdomar som till exempel stroke, för att nämna några användningsområden.

Det finns dock ett stort problem med att använda ljus för att ta bilder inne i kroppen. Till skillnad från radiovågorna som används för MRI, röntgenstrålning, och ultraljud, som färdas rakt igenom vävnad, så sprids ljus kraftigt. Redan efter att ha färdats några millimeter inne i vävnaden så är ljusets färdriktning helt slumpmässig. Eftersom man inte vet vilken väg ljuset färdats, tappar man rumsupplösning, och man kan inte återskapa en skarp bild. För närvarande finns det därför inte någon medicinsk teknik som använder ljus för att ta skarpa bilder av hjärnan eller andra djupliggande organ i kroppen.

Denna avhandling handlar om en teknik som heter ultrasound optical tomography (UOT) som kombinerar laserljus med ultraljud för att kringgå problemet med dålig upplösning på grund av spridning. Målet för UOT är möjliggöra medicinsk avbildning med ljus flera centimeter in i kroppen. Figur 1 visar hur en UOT-mätning fungerar. Laserljus och en ultraljudspuls skickas in i vävnaden. Laserljuset sprids över ett stort vävnadsområde. Ultraljudspulsen däremot kan fokuseras till en liten volym. En bråkdel av laserljuset passerar genom, och växelverkar med ultraljudspulsen, vilket gör att ljuset ändrar frekvens (alltså färgen på ljuset ändras). I Figur 1 visas det frekvensskiftade ljuset med blå pilar, och det icke frekvensskiftade bakgrundsljuset, alltså det ljus som inte passerat genom ultraljudspulsen och ändrat frekvens, med gröna pilar. Även om vi inte vet vilken väg det frekvensskiftade ljuset som kommer ut ifrån kroppen har tagit, så vet vi att det måste ha gått genom ultraljudspulsen, eftersom det frekvensskiftade ljuset enbart genererats i den volym som ultraljudspulsen upptar. Om man mäter intensiteten på det frekvensskiftade ljuset när man skickar ultraljudspulser till flera olika ställen i vävanden, så kan man en pixel i taget, skapa en bild där kontrasten kommer ifrån ljuset och upplösningen kommer från ultraljudet.

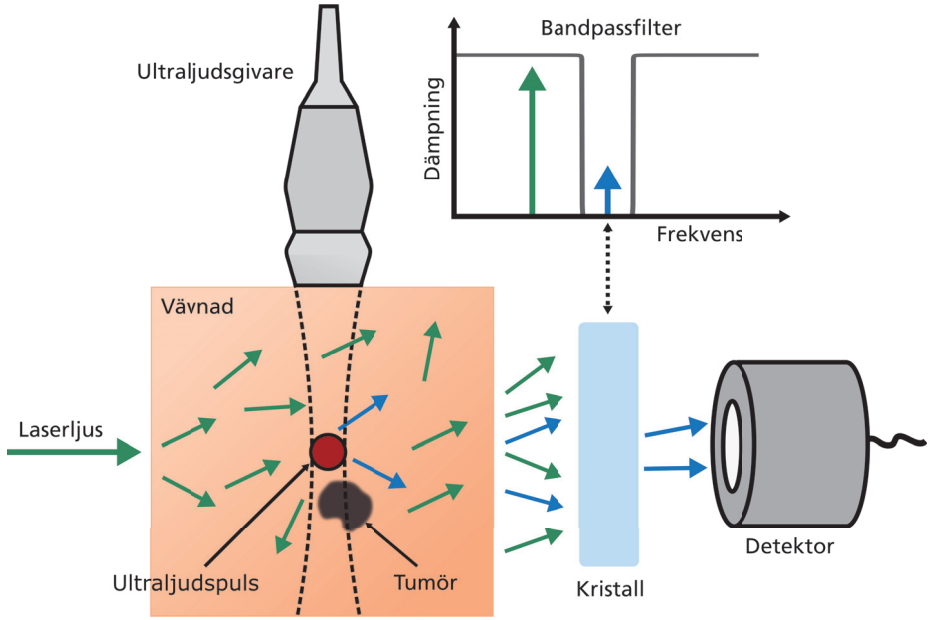

Figur 1: Under en UOT-mätning skickas både laserljus (gröna pilar) och ultraljudspulser (röd skiva) in i kroppen. Laserljuset sprids över ett stort vävnadsområde, men en liten del av ljuset går genom, och växelverkar med ultraljudspulsen, vilket gör att ljuset ändrar frekvens (blå pilar). Om man bara detekterar det frekvensskiftade ljuset kan man ta bilder med ljus djupt inne i kroppen. Man kan separera det frekvensskiftade ljuset (blå pilar) från bakgrundljuset (gröna pilar) med bandpassfilter som skapats i kristaller som innehåller joner av sällsynta jordartsmetaller.

Frekvensändringen som ultraljudspulsen ger upphov till är dock extremt litet jämfört med frekvensen på laserljuset (ungefär en del på hundra miljoner). Dessutom, så kan bakgrundsljusets intensitet, vara hundratusen gånger högre än intensitet på den frekvensskiftade signalen vi vill mäta för att kunna ta en UOT-bild. Vi måste alltså blockera det starka bakgrundsljuset, som inte innehåller någon användbar information, eftersom det ljuset inte passerat genom ultraljudspulsen. Detta är väldigt tekniskt utmanande, och även om UOT-konceptet har funnits sedan 1993, och flera olika metoder för att detektera signalen har undersökts, har man inte lyckats utveckla tekniken till ett stadie där den kan användas på sjukhus.

I Lund så undersöker vi hur man kan använda kristaller som innehåller joner av sällsynta jordartmetaller för att filtrera ut den frekvensskiftade signalen. Genom att belysa jonerna i kristallen med laserljus med samma frekvens som signalen, så kan man få dem att bli genomskinliga för signalen, samtidigt som de blockerar backgrundsljuset. Man kan skapa ett så kallat bandpassfilter i dessa kristaller, som visar sig ha unika egenskaper. Filtren kan ha väldigt small bandbredd, hög dämpning, och fungerar oberoende av vilken riktning ljuset har genom kristallen, vilket är väldigt användbart då det spridda ljuset lämnar vävnaden i alla riktningar. Att samtidigt ha dessa tre filtere-

genskaper är inte möjligt med någon annan typ av filter som finns idag.

I denna avhandling presenteras forskning på ny typ av kristall (Tm^{3+}:LaF_3) för UOT. Resultaten visar på en stor potentiell förbättring i filterprestande jämfört med tidigare använda kristaller. Vidare, så presenteras även UOT-mätningar på vävnadsfantomer i syfte att bättre förstå hur signalstyrkan beror på olika experimentparametar, vilket förbättrar vår förståelse för hur ett optimerat UOT-system kan presentera. Resultaten tyder på att UOT med hjälp av våra kristaller, skulle kunna användas för att ta bilder på mycket större djup än vad som är möjligt med andra tekniker idag, och till exempel, så skulle man kunna hitta tumören som ligger gömd flera centimeter ner i vävnaden i Figur 1.

Material and technique development for ultrasound optical tomography using spectral hole burning filters

Chapter 1

Introduction

Imaging techniques are very important in modern medicine, and have contributed to increasing both the life span and quality of life for many patients. Technologies such as ultrasound, X-rays, and magnetic resonance imaging (MRI), etc., are used to image deep inside the human body at hospitals around the world. These modalities have different contrast mechanisms and resolution, making them suitable for different medical diagnostic applications.

Ultrasound, for example, produces images of anatomical structures by measuring the reflections of acoustic waves from tissues with different acoustic impedance. Blood flow can also be visualized by measuring the Doppler shifts in the reflected acoustic waves, but the functional imaging capabilities of ultrasound are limited. The contrast in conventional X-ray imaging is based on differences in the atomic number of the constituents of various kinds of tissue. Tissues containing elements with a relatively high atomic number, such as bone (containing calcium), attenuate X-rays more strongly than soft tissues. Similarly to ultrasound, X-rays are primarily good for providing structural information. MRI is based on the use of radio frequency (RF) waves to probe the magnetic properties of hydrogen nuclei, and can provide both structural information and some functional information, such as blood flow. MRI is especially useful for imaging soft tissues and can, for example, differentiate between white and grey brain matter. However, MRI is expensive, and the imaging rate is slow.

Optical imaging techniques are sensitive to the local chemical composition of tissue, and thus provide spectral information not available with other imaging modalities. The possibility of targeting specific molecules in tissue has several potential advantages. For example, light is sensitive to both deoxyhaemoglobin (Hb) and oxyhaemoglobin (HbO_2). Quantification of the concentrations of Hb and HbO_2 allows

the oxygen saturation and blood volume to be determined, which, for example, are useful indicators in differentiating between healthy and cancerous tissue.

However, a major problem associated with optical imaging techniques is maintaining the resolution with increasing tissue penetration depth. Unlike X-rays, ultrasound, and RF waves, which propagate ballistically through tissue, light is strongly scattered. Below depths of ~1 mm, the path of the light in tissue is random, leading to loss of spatial resolution in conventional optical methods. Nonetheless, optical imaging techniques are very useful in many diagnostic applications.

Microscopy can be used to study the optical absorption of thin tissue samples (up to ~1 mm), where the photon trajectories only deviate minimally, allowing for high spatial resolution. Thin tissue sections can thus be examined under a microscope for evidence of cancer. Diffuse optical tomography can be used, for example, to characterize breast tumours. This technique employs multiple near-infrared light sources and detectors. The diffuse transmission from each of the light sources to each of the detectors is measured, allowing images to be reconstructed. However, the spatial resolution is limited to approximately 1/3 of the imaging depth [1]. Optical contrast techniques that provide better spatial resolution at depths of several centimetres are thus desirable.

1.1 Imaging beyond the optical scattering limit

Methods that combine light and ultrasound are being developed to extend optical imaging depths in biological tissues beyond the limit imposed by light scattering. Apart from the molecular contrast provided by such methods, the energies involved in both ultrasound and optical imaging are safe, in contrast to ionizing X-rays.

Current state-of-the-art ultrasound-assisted optical imaging of tissues is performed using photoacoustic tomography (PAT) [2]. In this method, the target tissue is irradiated with nanosecond laser pulses. The laser pulse is absorbed by molecules in the tissue, and the energy is converted into heat, causing thermoelastic expansion. This generates ultrasonic waves that can be detected with one or more ultrasound transducers to form an image. PAT provides molecular contrast images with a resolution of about 1/200 of the imaging depth [2]. This allows biological structures with a wide range of sizes to be studied, and sub-millimetre resolution is thus achievable at depths of a few centimetres. *In vivo* studies have shown promising results for PAT as a diagnostic tool for breast cancer [3]. The technique is also being investigated for human brain imaging [4], as well as other applications in biology and medicine [2]. PAT systems for both clinical and pre-clinical research are commercially available.

Another, less mature, ultrasound-assisted optical imaging technique is known as ultrasound optical tomography (UOT) (or acousto-optical tomography) [5, 6]. In UOT, the tissue is irradiated with both laser light and ultrasound pulses. A fraction of the scattered light passes through the ultrasound pulse and acquires a frequency shift via the acousto-optic effect. Optical contrast images with ultrasound resolution can be constructed by detecting the frequency-shifted light, while scanning the region of interest with the ultrasound pulse. Several coherent methods have been developed to detect the UOT signal. Although promising results have been obtained using tissue phantoms, the speckled light field resulting from multiple wave interference, and its rapid temporal decorrelation due to internal tissue motion, have made it difficult to translate these techniques to *in vivo* applications. Incoherent filtering of the UOT signal using spectral hole burning materials is insensitive to speckle deccorrelation, but requires a more complex set-up and cryogenic cooling. Unlike PAT, there are, to the best of the author's knowledge, no commercially available UOT systems. However, theoretical calculations by Walther et al. [7] indicate that an optimized spectral hole-burning-based UOT system would outperform PAT in terms of the contrast-to-noise ratio, and could thus be used to image deeper into tissue, or would provide a better contrast-to-noise ratio at shallow depths. Applications of UOT could include the detection and monitoring of cancer tumours, or imaging of the frontal part of the heart muscle [7] or the human brain [8]. However, further research is required on both the materials and the technique before this potentially powerful imaging tool can be applied *in vivo*.

1.2 Aim and outline

The aim of the research presented in this thesis was to further develop the UOT technique towards imaging in biological tissues at depths of several centimetres. Spectral hole burning filters [9, 10], which are created using optical pumping techniques in rare-earth-ion-doped crystals, were used for signal detection. An important part of this work was the identification and development of filter materials capable of supporting high-contrast filters at wavelengths suitable for biomedical applications.

Chapter 2 briefly discusses the interaction between light and tissue, while Chapter 3 provides the background to rare-earth-ion-doped crystals. Chapter 4 describes the basic principles of UOT, and presents a comparison between different detection methods (**Paper VI**), and UOT measurements made using spectral hole burning filters at 606 nm (**Papers I, III** & **IV**). Chapter 5 presents investigations into novel spectral hole burning materials for UOT at wavelengths suitable for biomedical applications (**Paper V**). Chapter 6 provides a summary and future outlook. Appendix A describes the design of an optical pulse shaping system, and a method for measuring the optical

path length change of optical fibres with temperature (**Paper II**).

Chapter 2

Light propagation in tissue

Biomedical optics relies on a good understanding of how photons propagate through and interact with various kinds of tissue. Biological tissue is very complex and may contain many constituents such as cells, proteins, lipids, etc., with a wide range of sizes, and a generally unknown distribution. The optical properties of different tissues can therefore vary by as much as an order of magnitude and the values presented in the literature can vary considerably for the same type of tissue. A review of the optical properties of tissues can be found in Ref. [11]. This chapter is mainly concerned with the absorption and scattering of light in tissue. Knowledge of these properties of tissue will be important in subsequent chapters, as they greatly affect the imaging depth achievable with the UOT technique, and must be considered when estimating the imaging capabilities of the technique (Chapter 4), and when choosing suitable operating wavelengths for *in vivo* application (Chapter 5).

2.1 Optical absorption in tissue

Optical absorption is the process in which matter takes up the energy of an incoming photon. This energy can, for example, be converted into heat, or re-radiated as fluorescence. The absorption coefficient, μ_a, is the probability of an absorption event occurring per unit distance travelled in a material, such that the transmittance T for a path length L_p, is described by the Beer-Lambert law.

$$T = e^{-\mu_a L_p} \tag{2.1}$$

Several different constituents of tissue are responsible for the absorption of optical photons. The absorption spectra for some common tissue constituents are shown in

Figure 2.1. At wavelengths below ~ 650 nm, the absorption coefficients of deoxyhaemoglobin (Hb) and oxyhaemoglobin (HbO_2) in the blood are very high, which severely limits the photon penetration depth achievable, and renders these wavelengths unsuitable for deep tissue optical imaging. The absorption coefficient of water is low in the visible region. However, for wavelengths in the near-infrared region the absorption by water is significant. This leads to the so-called tissue optical windows or therapeutic windows, in which the maximum optical penetration depth is achieved. Figure 2.1 highlights the first optical window between ~ 650 – 950 nm, which is the wavelength range mainly considered for the research presented in this thesis. However, a second optical window between 1100 – 1350 nm, as well as a third and fourth window at even longer wavelengths are also discussed in the literature [12].

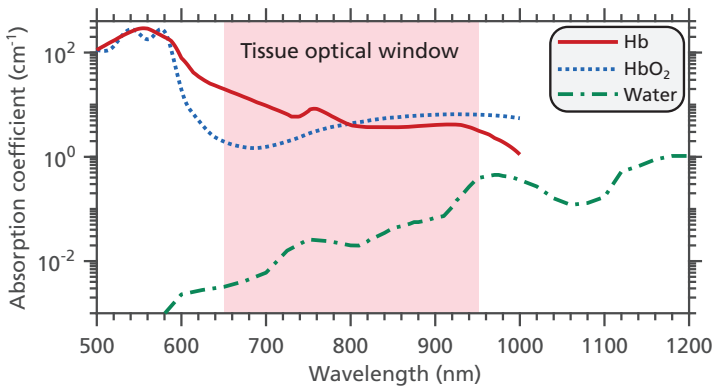

Figure 2.1: Absorption spectra for some important tissue constituents. The Hb and HbO_2 spectra are plotted using the data compiled by Prahl [13]. The water spectrum was originally measured by Hale et al. [14] and retrieved from Prahl [15]. Note that the y-axis is logarithmic.

It can be seen in Figure 2.1 that there is a considerable difference in the optical absorption spectra of Hb and HbO_2. In the ~ 650 – 700 nm region, the absorption coefficient of Hb is about one order of magnitude greater than that of HbO_2. At about 800 nm, the absorption coefficients for Hb and HbO_2 are equal, a so-called isosbestic point. At longer wavelengths, the absorption coefficient of HbO_2 is greater. The differences in these spectra allow two or more wavelengths to be combined to quantify the relative concentrations of Hb and HbO_2, and thus calculate the tissue oxygen saturation.

Different kinds of tissue have different amounts of blood, water, and fat, etc., resulting in different absorption spectra. The spectrum of generic tissue can be estimated by summing the individual tissue constituent spectra [11]. For example, for a tissue where only Hb, HbO_2, and water contribute to absorption, the spectrum can be calculated as:

$$\mu_a(\lambda) = B_v S_{O_2} \mu_a^{oxy} + B_v (1 - S_{O_2}) \mu_a^{deoxy} + W \mu_a^{wat} \tag{2.2}$$

where B_v is the average blood volume fraction, S_{O_2} is the oxygen saturation, W is the water content, and λ is the wavelength. The absorption spectra for Hb, HbO2, and water are denoted μ_a^{deoxy}, μ_a^{oxy}, and μ_a^{wat}, respectively. An example of such a spectrum is shown in Figure 2.2, where the tissue is assumed to have an average blood volume fraction of 4% and oxygen saturation of 85%. This is similar to muscle tissue, but other constituents such as connective tissue, fat, and myoglobin (a protein) could also contribute to light absorption [7]. In the example shown in Figure 2.2, water mainly starts to contribute to the absorption at wavelengths longer than 900 nm. At shorter wavelength the absorption is almost exclusively caused by blood.

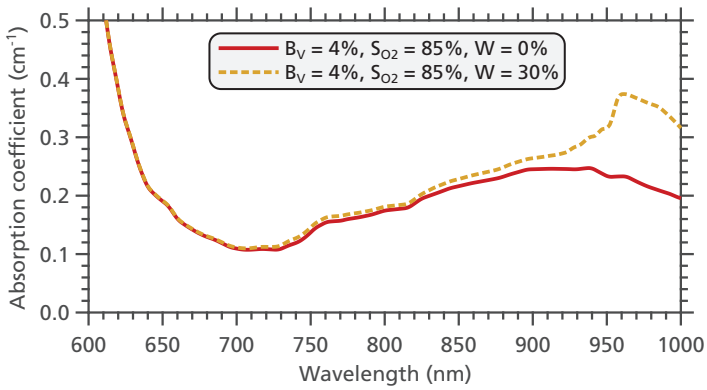

Figure 2.2: Absorption spectra for generic tissues calculated based on Equation (2.2). The blood volume fraction, oxygen saturation, and water content of the tissue are denoted B_v, S_{O_2}, and W, respectively.

2.2 Optical scattering in tissue

Light scattering is the process causing a photon to deviate from a straight trajectory due to inhomogeneities in the refractive index of the tissue, and is the dominant light-tissue interaction in the near-infrared optical region. When light enters a thick tissue, the photons will follow multiple paths as shown in Figure 2.3, and will leave the tissue with random directions and phases. It is this randomization of photon paths in tissue that prevents spatially resolved optical imaging at greater tissue depths, and make techniques such as UOT, which overcome this problem, interesting to pursue.

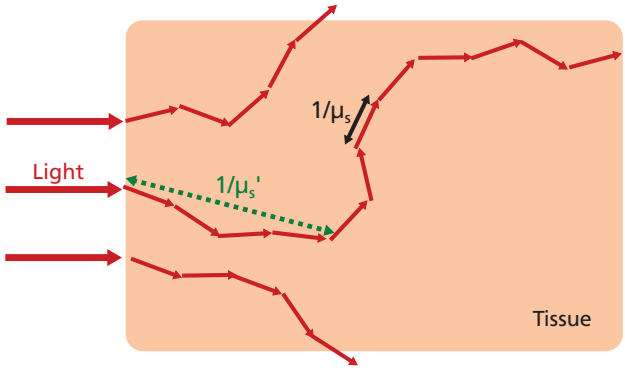

Figure 2.3: Optical photons are strongly scattered by tissue and therefore propagate over many different paths. The scattering mean free path ($1/\mu_s$) and transport mean free path ($1/\mu_s'$) discussed below are illustrated in the figure.

The multiple scattering events that occur in tissue and their complex microscopic structure motive a statistical description of the scattering properties of tissue. The scattering coefficient, μ_s, is introduced to describe the probability that a scattering event occur per unit path length. Its inverse is called the scattering mean free path, and is the average distance a photon can travel in tissue between scattering events. The size of the scattering particles is mostly of the order of the optical wavelength or larger, and from Mie theory it follows that the scattering then occurs mostly in the forward direction. An averaged parameter called the anisotropy factor $g = \langle \cos\theta \rangle$ is introduced to describe the relative amount of forward scattering, where θ is the deflection angle from the original trajectory due to the scattering event. If $g = 0$, the scattering is isotropic, and if $g = 1$, scattering occurs only in the forward direction (i.e., there is no scattering). For biological tissues $g \sim 0.7{-}0.9$. The reduced scattering coefficient is expressed by combining μ_s and g.

$$\mu_s' = \mu_s(1 - g) \tag{2.3}$$

The inverse of the reduced scattering coefficient is called the transport mean free path, and is the average distance a photon can propagate in a tissue before its propagation direction is randomized. The reduced scattering coefficient decreases for longer wavelength and its wavelength dependence can be written [11]:

$$\mu_s' = a_s\left(\frac{\lambda}{\lambda_0}\right)^{-b_s} \tag{2.4}$$

where λ_0 is a reference wavelength, a_s is μ_s' at λ_0, and b_s is called the scattering power. The reduced scattering coefficient is plotted for breast and muscle tissue in Figure 2.4 based on Equation (2.4) and average values of a_s and b_s given by Jacques [11]. It can be seen that the reduced scattering coefficient is typically ~ 10 cm^{-1}. Photons

therefore propagate ~ 1 mm before their path becomes randomized, and this is therefore typically the limit for conventional optical imaging techniques. Tissues with a higher amount of fat, such as breast tissue, are generally expected to be more strongly scattering compared to, for example, muscle tissue. Variations in tissue scattering can be indicative tissue health status. The UOT technique investigated in the presented thesis work can image differences in optical scattering [16].

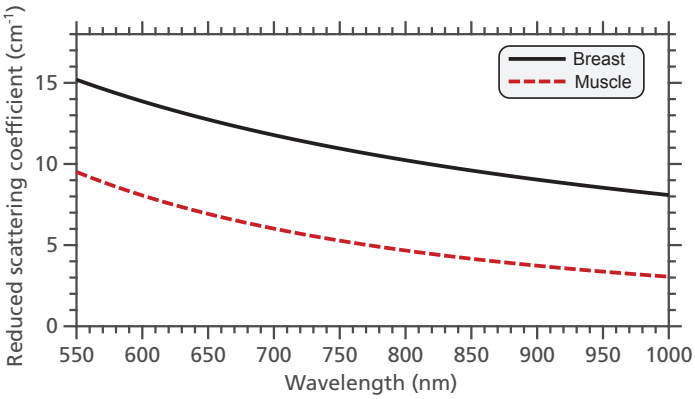

Figure 2.4: Reduced scattering coefficient of breast and muscle tissue plotted using Equation (2.4) based on averaged parameters given by Jacques [11].

2.3 Speckle

As photons propagate over many different paths through tissue, multiple wave interference causes a speckle pattern of bright and dark spots to be formed, as shown in Figure 2.5. For thick tissue samples, the speckles are expected to be uncorrelated with random phases and are de-polarized. The size of these speckles on the tissue surface is of the order of the optical wavelength assuming that the numerical aperture of the speckle grain in the output plane is one. The smallest possible speckle size that can be imaged on a camera is then inversely proportional to the numerical aperture of the detection set-up. Living tissues are dynamic, and the scattering particles will move with time due to physiological motion such as blood flow. This causes the speckle pattern to move, that is, it decorrelates. This decorrelation typically takes place on time scales of $\sim 0.1 - 1$ ms in human tissue [17], and decreases for thicker tissues due to the increased number of scattering events. This has been demonstrated *in vivo* in the mouse brain by Qureshi et al. [18].

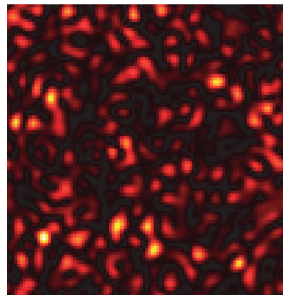

Figure 2.5: Theoretical speckle pattern formed due to multiple wave interference, calculated using the algorithm presented by Duncan et al. [19].

The motion of scattering particles can be quantified by analysing the temporal and spatial statistics of speckle patterns. This is done in laser speckle contrast imaging to image blood flow [20]. The motion is, however, a problem in many ultrasound optical tomography methods, as a single acousto-optic signal has to be acquired within the correlation time, as will be further discussed in Chapter 4.

Chapter 3

Rare-earth-ion-doped crystals

The rare-earth elements are scandium, yttrium and the 15 lanthanides included in Figure 3.1. Several of the rare-earth elements were discovered in and are named after the Swedish mining village Ytterby. Their abundance in the Earth's crust varies, but they are not necessarily as rare as their name may suggest. Cerium, for example, is around the 25th most abundant element [21]. Promethium on the other hand is radioactive, and therefore does not occur naturally. Rare-earth elements are used for a wide range of important applications in today's society. Erbium-doped amplifiers enable long-range optical fibre communication, and thus the modern internet. Rare-earth elements are also used in electronic components, lasers, magnets, medical devices, fluorescent lamps, etc.

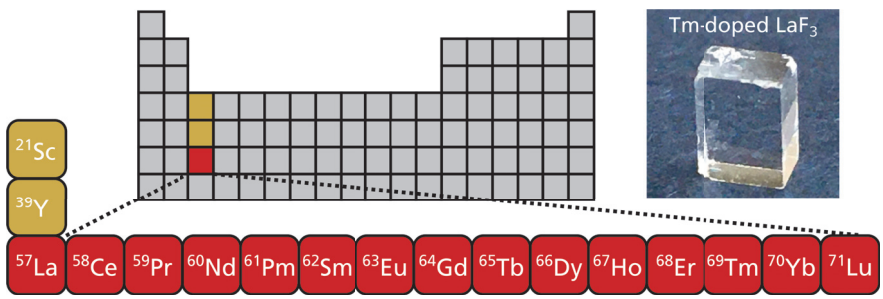

Figure 3.1: The rare-earth elements and their position in the periodic table. The photograph shows an LaF_3 crystal doped with thulium. The figure was inspired by Ref. [22].

Inorganic crystals doped with rare-earth elements offer unique properties when cooled to < 5 K, such as extremely narrow optical transition linewidths and very long lifetimes of hyperfine states. Such materials, are currently being investigated for quantum

information and quantum communication applications [23], laser frequency stabilization [24, 25], RF spectrum analysis [26], and UOT [9, 27–29], the medical imaging technique that is the topic of this thesis.

This chapter gives a brief overview of rare-earth-ion-doped crystals, and presents the phenomena observed in these materials that are important for the UOT technique. This includes spectral hole burning and slow light, which are important concepts for detecting the UOT signal in the present work. Multi-phonon relaxation is also briefly discussed, as it is relevant for the studies of UOT filter crystals with low maximum phonon energies presented in Chapter 5. Further details on the spectroscopic properties of rare-earth-ion-doped crystals can be found, for example, in Ref. [30].

3.1 Energy level structure

Rare-earth elements often occupy triply ionized charge states when doped into crystalline hosts. The electron configuration of most lanthanides is then $[\mathrm{Xe}]4f^N$, where N is the number of valence electrons. The transitions relevant in the work presented in this thesis occur between states within the 4f shell. The completely filled 5s and 5p shells extend spatially further out than the 4f shell, shielding the 4f electrons from environmental perturbations. Their energy levels therefore remain very similar to the free ion energy levels. Although 4f-4f transitions are forbidden in the free ion (since the parity of the state is unchanged), the small perturbations caused by the crystal field distorts the inversion symmetry, making these transitions weakly allowed.

Figure 3.2 shows the general energy level structure of rare-earth-ion-doped crystals. Coulombic interactions split the $4f^N$ configuration into terms labelled ^{2S+1}L. Each term is further split by the spin-orbit interaction into levels labelled $^{2S+1}L_J$. L, S, and J are the total orbital angular momentum, the total spin angular momentum, and the total angular momentum, respectively. The electric field of the host crystal splits each level into a maximum of $2J+1$ crystal field levels. For ions with an odd number of electrons and thus half-integer spin S, so-called Kramers ions, the crystal field levels remain at least doubly degenerate. For ions with an even number of electrons, the degeneracy can be completely lifted. The crystal field levels can be further split by additional interactions, such as hyperfine, nuclear quadrupole or Zeeman interactions. For the applications relevant for the presented thesis work, it is transitions between the lowest energy crystal field level in the ground state to the lowest energy crystal field level in an excited state that display the desired properties such as narrow transition linewidths. These are the so called lowest-to-lowest transitions. Unless otherwise stated, it is understood that it is these transitions that are being referred to. Frequency splittings and population redistribution among hyperfine levels will become relevant

concepts in subsequent chapters.

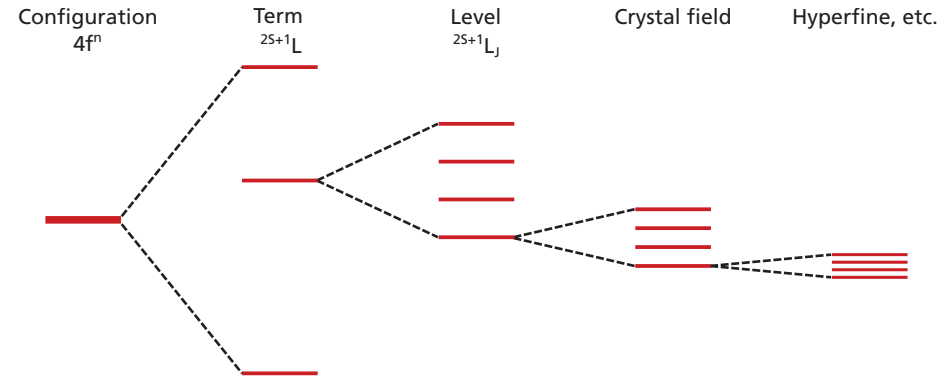

Figure 3.2: General energy level structure of rare-earth-ion-doped inorganic crystals. The interaction strength decreases when going from left to right in the figure.

3.2 Transition linewidth

A two-level transition has an associated frequency width over which it absorbs and emits radiation. For a single rare-earth dopant in a crystal, this frequency width, called the homogeneous linewidth Γ_h, can be extremely narrow. Linewidths down to ~ 100 Hz have been measured in Er^{3+}:Y_2SiO_5 and Eu^{3+}:Y_2SiO_5 [31, 32], which are the most narrow optical linewidths measured in solids. The homogeneous transition linewidth can be written:

$$\Gamma_h = \frac{1}{\pi T_2} = \frac{1}{2\pi T_1} + \Gamma_{other} \tag{3.1}$$

where T_2 is the coherence time, and T_1 is the radiative lifetime of the excited state. T_1 thus ultimately limits the linewidth. The long excited state lifetimes observed in rare-earth-doped materials (up to several ms), correspond to very narrow T_1-limited linewidths. However, even at cryogenic temperatures, the lifetime limit is seldom fully met, due to other mechanisms causing linewidth broadening, which in Equation (3.1) are encapsulated in Γ_{other}. Examples of broadening mechanisms are phonon absorption, emission, and scattering, and spin flips, etc.

3.2.1 Inhomogeneous broadening

In a doped crystal, the rare-earth-ions randomly replace host ions in the crystal lattice. The ionic radius of the rare-earth-ions will not exactly match that of the host ions they

replace, which causes local distortion of the crystal lattice, and the dopant ions experience slightly different surrounding electric fields. At cryogenic temperatures, the resulting Stark shifts in the transition frequencies can be orders of magnitude larger than the homogeneous linewidth of a single ion. This gives rise to inhomogeneously broadened transitions, as shown in Figure 3.3. The inhomogeneous linewidth, Γ_{ih}, typically ranges from ~ 1 GHz up to ~ 100 GHz depending on the rare-earth-ion-doped material. The peak absorption coefficient is denoted α_0, which varies widely between rare-earth-ion-doped materials and transitions, and depends on the rare-earth doping concentration. The absorption coefficient usually increases linearly with doping concentration to a certain level where it saturates, and eventually a point is reached where adding more of the rare-earth-dopant only increases the inhomogeneous linewidth. An example of a rare-earth-ion-doped crystal with high absorption is $^{171}Yb^{3+}$:YVO_4, in which a transition with $\alpha_0 = 450$ cm^{-1} has been measured for a doping concentration of 100 ppm [33].

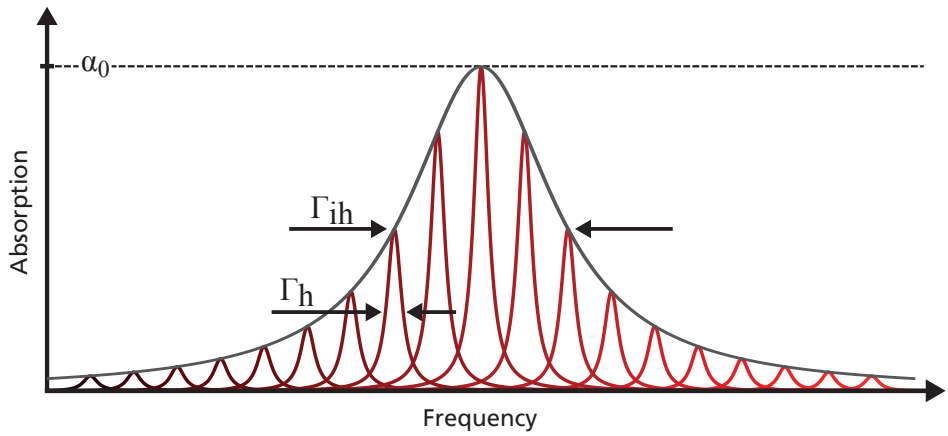

Figure 3.3: At cryogenic temperatures the rare-earth optical transitions are inhomogeneouosly broadened with linewidth Γ_{ih}. The homogeneous linewidth Γ_h can be orders of magnitude narrower. The peak absorption coefficient is denoted α_0.

3.3 Spectral hole burning

The inhomogeneously broadened transitions allow optical pumping of a narrow frequency range of the absorption profile. Consider a three-level system consisting of a ground, excited, and metastable state, as shown in Figure 3.4(a). The lifetime of the metastable state is much longer than the lifetime of the excited state. Initially, all ions occupy the ground state. When a rare-earth-ion-doped material is irradiated with narrow-linewidth laser light with frequency f_0, ions within a narrow frequency band of the inhomogeneous absorption profile, will be transferred to the excited state. This

results in a decrease in the absorption at the laser frequency, called a spectral hole, as shown in Figure 3.4(b). The minimum spectral hole width is limited by the homogeneous linewidth of the rare-earth ion. On timescales shorter than the excited state lifetime, the spectral hole is the result of population storage in the excited state. In the current example, the population decays from the excited state into the long-lived metastable state. Eventually, all ions may be transferred into the metastable state, and the spectral hole is due to population storage in the metastable state. Spectral hole lifetimes vary by several orders of magnitude, depending of the nature of the metastable state. In Eu^{3+}:Y_2SiO_5, an impressive spectral hole lifetime of ~ 1 month has been measured due to population storage in the hyperfine levels in the ground state [34, 35].

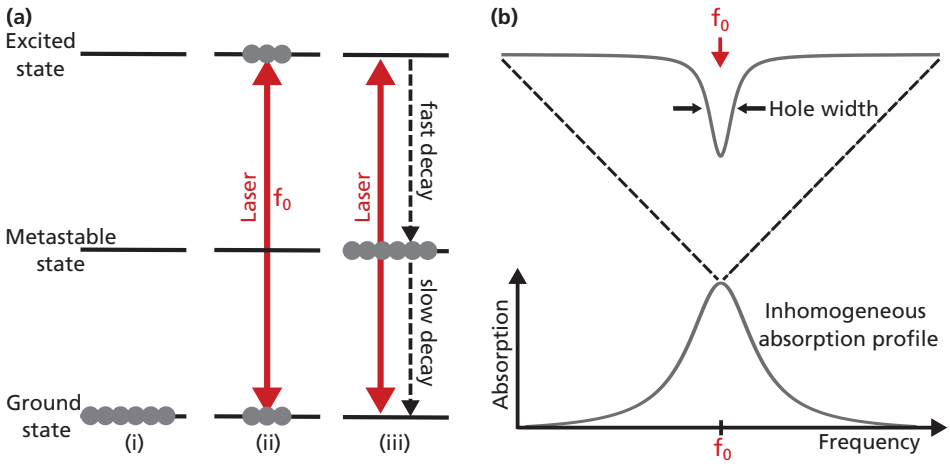

Figure 3.4: Principle of spectral hole burning in a three level system with a ground, excited, and metastable state. (a) Only ions at frequency f_0 are considered. (i) Initially, the ions absorbing at f_0 populate the ground state. (ii) Applying a laser field of frequency f_0 transfers ions to the excited state. (iii) From the excited state the ions can decay to and be stored in the long-lived metastable state. This process generates a dip in the inhomogeneous absorption profile of the material at the laser frequency f_0, called a spectral hole as shown in (b).

3.3.1 Hyperfine hole burning

For systems with two or more closely lying ground and/or excited states, more complex patterns of spectral holes can be observed. For example, consider a system with two ground states and two excited states as shown in Figure 3.5. The splitting of the ground (Δg) and excited states (Δe) are much smaller than both the inhomogeneous broadening and the thermal energy, $k_B T$, where k_B is the Boltzmann constant and T the absolute temperature. The ground states are therefore equally populated in the absence of external influence. If a laser field with frequency f_0 is applied, it will be simultaneously resonant with all four transition, in four different so-called classes of

ions, due to the inhomogeneous broadening. For each class of ions the laser field will empty the ground state from which it is resonant, via the excited state, transferring the ions to the other ground state, as shown in Figure 3.5(a). The decrease in absorption at the original laser frequency f_0 is the main spectral hole. However, there is also less absorption at transition frequencies of $f_0 \pm \Delta e$ (indicated by green arrows in Figure 3.5(a)), resulting in the appearance of so-called side holes. Similarly, the redistribution of population results in an increase in absorption at transition frequencies $f_0 \pm \Delta g$, $f_0 \pm (\Delta e + \Delta g)$, and $f_0 \pm (\Delta e - \Delta g)$, (indicated by blue arrows in Figure 3.5(a)), which are called antiholes. Spectral hole burning can be a powerful spectroscopic tool for measuring the splitting of the excited and ground states, since the frequency positions of the side hole and antihole depend on the splitting of the ground and excited states.

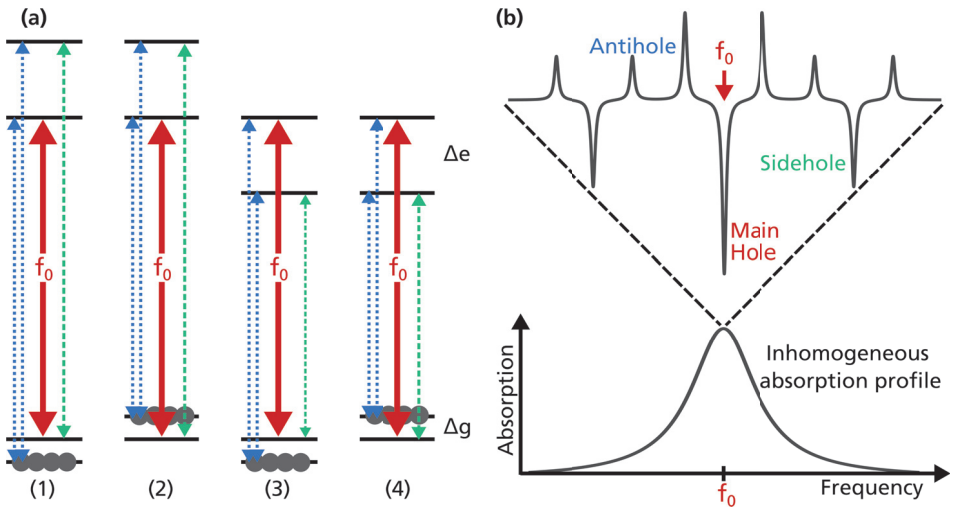

Figure 3.5: (a) The laser at frequency f_0 is simultaneously resonant with four transitions, one in each of the four classes of ions, due to the inhomogeneously broadened absorption profile. The redistribution of ions between the ground states due to the applied laser field results in a main spectral hole at f_0, side holes at transitions indicated by the green arrows, and antiholes at transitions indicated by the blue arrows. (b) Typical spectral hole pattern with side holes and antiholes on either side of the main hole.

3.4 Slow light

The speed of light in vacuum, c, is the ultimate limit on any information-carrying signal, and has been defined since 1983 as exactly 299 792 458 m/s. From a human perspective, this is an almost incomprehensible speed, and light could, for example, travel seven times around the Earth in slightly less than one second. There are, however, ways of significantly reducing the speed of light, in order to obtain so-called

slow light, by creating spectral regions with very high dispersion. This is possible, for example, using spectral hole burning in crystals, Bose-Einstein condensates [36], or hot atomic gases [37]. Potential applications for slow light include telecommunications [38], laser frequency stabilization [24], and medical imaging with UOT [9].

A monochromatic electromagnetic field propagating through a material with refractive index n, interacts with the atoms in the material, causing the electrons around the nuclei to oscillate, and these in turn will radiate their own electromagnetic fields. The total contribution from all electrons is a field with lower amplitude that lags behind the incoming electromagnetic field. The total electromagnetic field propagating through the material will be the sum of the incoming and electron-induced fields and it does so at a speed $v_p = c/n$, called the phase velocity.

However, electromagnetic radiation is never truly monochromatic, but contains a range of different frequency components. Consider an optical pulse as shown in Figure 3.6. The maximum amplitude of the pulse occurs at the position where the frequency components that make up the pulse maximally constructively interferes. If the medium through which the optical pulse is propagating is absorptive, it must also have a frequency-dependent refractive index. This is necessary because the absorption of frequency components of a pulse must involve phase changes of other components to not contradict causality [39].

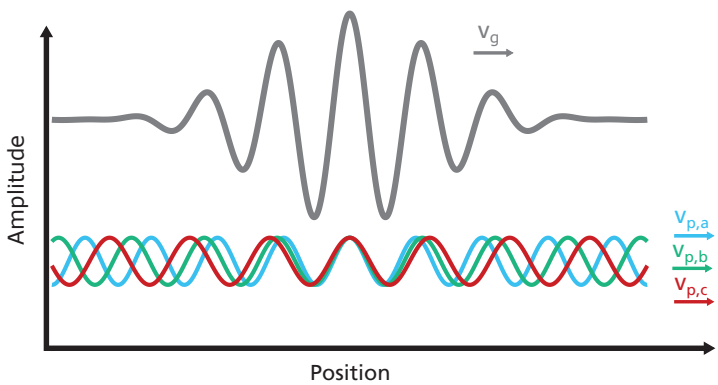

Figure 3.6: A pulse and three of its frequency components. In the case of a frequency-dependent refractive index, the different components will propagate at different phase velocities $v_{p,a}$, $v_{p,b}$, and $v_{p,c}$. However, the pulse propagates at the group velocity v_g, which may be different from the phase velocities.

Due to the frequency-dependent refractive index, the individual frequency components of the pulse will propagate at different phase velocities, which may all be close to c. However, the sum of the frequency components, which is the actual pulse, can propagate at a significantly different speed. The group velocity is the speed of the

maximum of the envelope of the pulse, and is given by:

$$v_g = \frac{c}{n + \omega \frac{\partial n}{\partial \omega}} \tag{3.2}$$

where ω is the angular frequency. For a visible optical pulse propagating through a piece of normal glass, which has its absorption in the ultraviolet wavelength range, the term $\omega \frac{\partial n}{\partial \omega}$ is negligible, and the pulse will travel at a speed very close to c/n. For an optical pulse propagating inside a spectral hole, it is possible to have almost zero absorption at the frequency of the spectral hole, and high absorption less than a MHz away. The Kramers-Kronig relations can be used to calculate the frequency-dependent refractive index across such a spectral hole. As illustrated in Figure 3.7, there will be a rapid increase in the refractive index with frequency within the passband of the spectral hole. The term $\omega \frac{\partial n}{\partial \omega}$ in Equation (3.2) can then be very large, and group velocities several orders of magnitude lower than c are possible. For a square-shaped spectral hole with width Γ_{hole}, the group velocity can be approximated to [24]:

$$v_g = \frac{\pi^2 \Gamma_{\text{hole}}}{\alpha_{\text{out}}} \tag{3.3}$$

where α_{out} is the absorption coefficient outside the spectral hole. As will be seen in Chapter 4, this slowing of light due to strong dispersion inside spectral holes can be used for medical imaging with UOT.

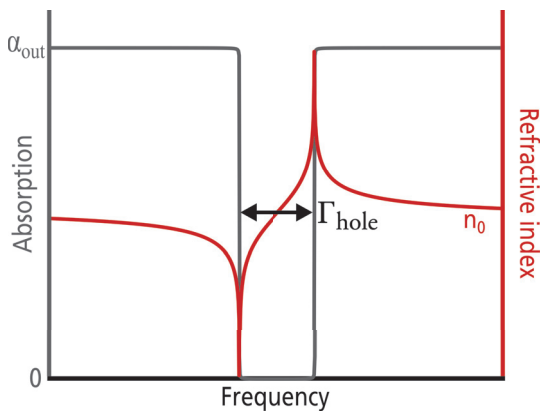

Figure 3.7: A square-shaped spectral hole (grey) and the real part of the refractive index (red). A rapid increase in refractive index with frequency can be seen within the passband of the spectral hole. The refractive index of the host crystal is denoted n_0.

3.5 Multi-phonon relaxation in rare-earth-doped crystals

The constituents that make up a crystal, for example, ions, are arranged in a highly structured three-dimensional pattern held together by inter-atomic forces, forming a

crystal lattice. The ions can vibrate around their equilibrium positions, generating mechanical waves in the lattice. Phonons are quanta of such crystal lattice vibration. A crystal will have a characteristic phonon spectrum, and a maximally allowed phonon frequency, called the phonon cut-off frequency, ω_D. In the Debye model of phonons, the cut-off frequency is expected to be [40, 41]:

$$\omega_D \propto N_v^{1/3} \sqrt{\frac{M}{\rho}} \tag{3.4}$$

where N_v is the number of ions per unit volume, M is the elastic modulus, and ρ is the density.

In a rare-earth-ion-doped crystal, an upper $^{2S+1}L_J$ energy level can decay to a lower $^{2S+1}L_J$ level by emitting multiple phonons that carry away the energy difference between two levels. Phonon relaxation rates decrease exponentially with the number of phonons required to bridge the energy gap, E_{gap}. Generally, if $E_{gap} \lesssim 5\hbar\omega_D$, the phonon relaxation rate dominates over the radiative relaxation rate [42–44], leading to short lifetimes and broad homogeneous linewidths, see Equation (3.1). As the energy gap increases above $\sim 5\hbar\omega_D$, the phonon relaxation rate rapidly becomes negligible. The rare-earth transitions that are usually investigated for spectral hole burning applications therefore typically have $E_{gap} > 5\hbar\omega_D$.

If it is desirable to use rare-earth transitions with small energy gaps, while maintaining long lifetimes, the choice of crystal host must be carefully considered. Choosing a host crystal with a lower phonon cut-off frequency would suppress phonon relaxation, since the relaxation process would have to involve a larger number of phonons to bridge the gap, which is a process with a lower probability. As can be seen from Equation (3.4), softer and denser crystals, such as fluorides and alkali lead halides, generally have lower phonon cut-off frequencies, which could potentially enable spectral hole burning applications on transitions not possible with the harder and less dense oxides.

Chapter 4

Ultrasound optical tomography

Ultrasound optical tomography (UOT) is currently being developed to image optical contrast deep inside scattering media, such as tissue, at depths of several centimetres. Reviews on this topic have been published [5, 6]. This chapter describes the basic principles and potential medical applications of UOT. The results presented in **Paper VI**, on the comparison of contrast-to-noise ratios of various signal detection methods for UOT, are summarized. Both published (**Papers I**, **III**, & **IV**) and unpublished UOT measurements using spectral hole burning filters in Pr^{3+}:Y_2SiO_5 are presented.

The principle of UOT is shown schematically in Figure 4.1. Optical and ultrasonic pulses at frequencies f_L and f_{US}, respectively, are applied to the tissue. The optical photons are scattered multiple times, and their directions of propagation are rapidly randomized. Ultrasound on the other hand, is orders of magnitude less scattered by tissue, which allows for narrow focusing (~mm). The ultrasound pulses cause a spatially localized periodic variation of the refractive index and movement of the scattering centres. The optical path lengths of photons propagating through the ultrasound pulse will be modulated at the ultrasound frequency, leading to a frequency shift, and sidebands of the carrier at multiples of $\pm f_{US}$. The ultrasound-modulated photons are called tagged photons, while the photons at the original laser frequency are called untagged photons. The number of tagged photons emerging from the tissue depends on the local photon fluence, and the optical and acoustic properties of the insonified tissue volume. Optical contrast images can therefore be formed by spatially scanning the tissue with the ultrasound pulse while counting the tagged photons for each ultrasound pulse position. An example of a one-dimensional (1D) image is shown in the lower part of Figure 4.1. Here, a region of tissue with a higher optical absorption coefficient than the background tissue is scanned with the ultrasound pulse. This is seen as a decrease in the number of detected tagged photons. Two- and three-dimensional

images can be obtained by adding other scanning axes.

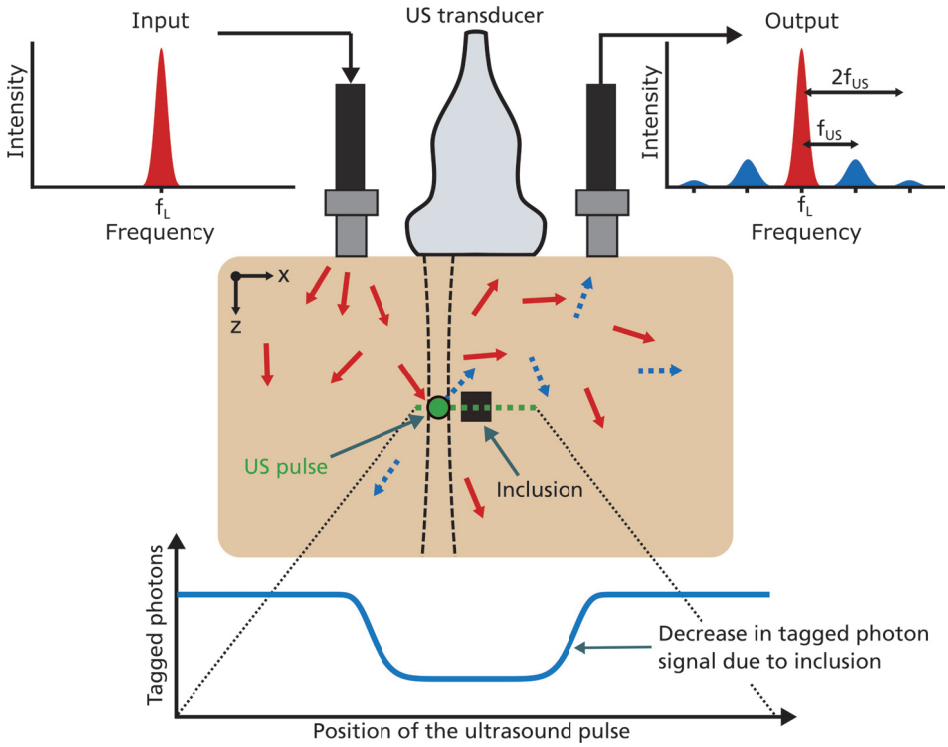

Figure 4.1: Principle of ultrasound optical tomography. Photons with a frequency f_L (red arrows) enter the tissue. A fraction of these photons traverses the ultrasound (US) pulse and are frequency shifted by multiples of the ultrasound frequency f_{US} (blue dashed arrows). Detection of the shifted photons enables spatially resolved optical contrast measurements inside the tissue. Scanning the tissue with the ultrasound pulse across an inclusion with higher optical absorption than the background tissue (along the green dashed line), gives a one-dimensional image in which the inclusion is seen as a decrease in the number of tagged photons (lower part of figure).

4.1 Methods of detecting tagged photons

A number of methods of detecting tagged photons have been developed since the first experimental demonstration of UOT in 1993 [45]. However, several challenges have prevented the translation of promising experimental results on tissue-mimicking phantoms to *in vivo* application.

As only a small fraction of the photons traverse the ultrasound pulse and become tagged, the fraction of tagged to untagged photons is low, typically $10^{-3} - 10^{-5}$. This means that a weak signal must be detected on top of a much stronger background. The photons are also emitted from a large external tissue area in all directions. Since

the emission etendue (the area multiplied by the solid angle) is large, the detection system etendue must also be large for efficient detection.

For coherent detection methods, the speckled optical field generated in the tissue, and its temporal decorrelation, which in living tissue occurs on time scales of $\sim 0.1 - 1$ ms due to internal movement [17], becomes a problem. In early studies fast single-element detectors were used to measure the intensity modulation of speckles due to the beating between tagged and untagged photons [46, 47]. However, the phases of each speckle grain are random, and although a detector with a large area can collect more photons, the increased number of speckle grains reduces the effective modulation depth, leading to poor signal-to-noise ratio (SNR).

Parallel detection of the individual speckles using multi-pixel detectors (cameras) was developed to improve the SNR [48]. However, several camera frames have to be acquired to reconstruct the UOT signal. The low frame rates of cameras with high pixel counts make such methods susceptible to speckle decorrelation, and they are currently not suitable for *in vivo* measurements. Signal detection based on a single image is thus of interest. This is possible with laser speckle contrast schemes [49, 50], but the SNR is low due to the random nature of speckles. Instead, methods such as single-shot off-axis holography developed recently [8] could provide higher sensitivity. Cameras capable of lock-in detection in each pixel giving the modulated signal could also be used [51]. However, these lock-in cameras currently suffer from low pixel counts of ~ 0.1 mega-pixels (Mpx), and thus have a comparatively low etendue.

Photorefractive-crystal-based detection [52, 53] employs a single-element detector and can offer a larger etendue than current camera-based methods. Impressive imaging depths have been demonstrated in phantoms with tissue-like optical properties [54], but the method still suffers from speckle deccorelation due to the $\sim$ ms photorefractive response time of the crystals.

Problems associated with speckle decorrelation can be avoided with incoherent filtering methods as the tagged photon flux is measured directly by matching the filter passband with the frequency of the tagged photons. For an optical wavelength of 800 nm and an ultrasound frequency of 5 MHz, the optical shift due to the ultrasound is about 10^{-5} nm. The filters must thus be extremely narrowband and have high suppression of untagged photons. This is possible with Fabry-Perot interferometers [55, 56]. However, this approach suffers from low signal due to the low detection etendue of Fabry-Perot interferometers capable of providing sufficiently narrow filter passbands (etendue < 1 mm^{2}sr).

Filters based on spectral hole burning in rare-earth-ion-doped crystals (see Section 3.3) have been used for UOT [9, 27–29] due to their capability of supporting ~ 1 MHz bandwidth filters that accept photons from a $\sim 2\pi$ solid angle over a ~ 1 cm^2 area,

thus resulting in a large etendue (similar to that in photorefractive detection). The disadvantages of spectral hole burning filters are that the filter wavelength is limited by the available suitable rare-earth transitions, and the need to cool the filter crystals to cryogenic temperatures, leading to comparatively bulky set-ups.

Several methods have thus been used for the detection of tagged photons, although it is not clear which is the most suitable methods for future UOT devices and medical applications. In order to shed light on the strengths and weaknesses of various methods, the contrast-to-noise ratios (CNRs) of various methods, including spectral hole burning, single-shot off-axis holography, speckle contrast, and photorefractive holography, were compared (**Paper VI**).

After briefly introducing the concept of the CNR, the following subsections present the spectral hole burning, single-shot off-axis holography, speckle contrast, and photorefractive holography methods. Attention will be focused on the spectral hole burning method, since it is central to the work presented in this thesis. The relative imaging performance of the methods is then compared in terms of CNR.

4.1.1 Contrast-to-noise ratio

The SNR is often used to quantify the quality of a signal. However, the ability to detect changes in the signal is more relevant for UOT. Therefore, the CNR is used instead, and is defined as:

$$\mathrm{CNR} = \frac{\text{contrast}}{\text{noise}} = \frac{|S_\mathrm{A} - S_\mathrm{B}|}{\sqrt{\sigma_\mathrm{A}^2 + \sigma_\mathrm{B}^2}} \tag{4.1}$$

where $|S_\mathrm{A} - S_\mathrm{B}|$ is the difference in the signal from two tissue regions A and B with different optical properties. For example, there may be a tumour in region A, and healthy tissue in region B. The two signals have standard deviations σ_A and σ_B, respectively. The further use of the A and B subscripts refers to the here mentioned two tissue regions. To distinguish image features in a UOT measurement, such as a tumour, the CNR should be above one, and preferably significantly greater than one.

4.1.2 Spectral hole burning filters

The spectral hole burning phenomenon described in Section 3.3 is used to detect the tagged photon signal. The optical signal leaving the tissue (tagged and untagged photons) is shown in Figure 4.2(a). Prior to a UOT measurement, spectral holes are prepared at the tagged photon frequencies, as shown in Figure 4.2(b). The untagged

photons outside the spectral holes are absorbed by the rare-earth ions in the crystal, while the tagged photons are transmitted. The tagged photons are also slowed down compared to the untagged photons due to the slow light effect induced by the rapid increase in refractive index with frequency within the filter passband, as discussed in Section 3.4. The later arrival time of tagged photons at the detector thus allows for further suppression of untagged photons using time gating, see Figure 4.2(c).

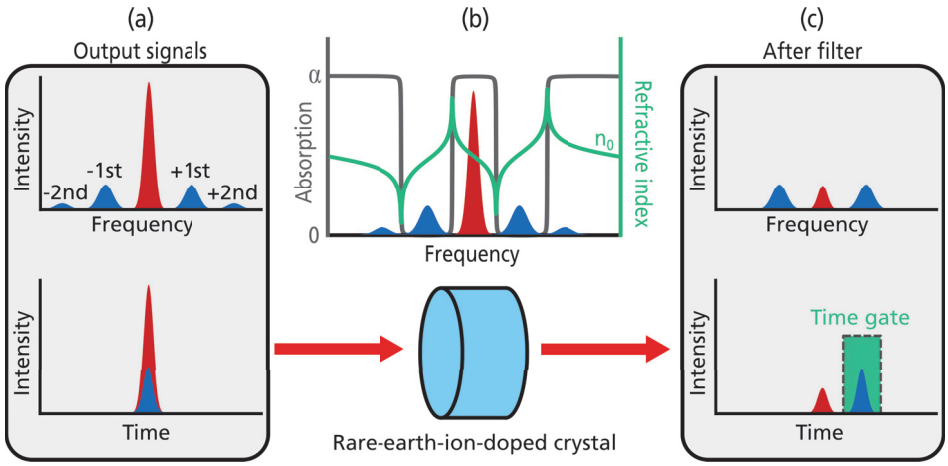

Figure 4.2: Principle of tagged photon detection using spectral hole burning in rare-earth-ion-doped crystals. (a) Optical signals leaving the tissue. The tagged (blue) and untagged (red) photons leave the tissue at the same time. The ratio of tagged to untagged photons is low (much lower than illustrated in the figure). (b) The photons from the tissue are passed through the filter crystal with the passband matching the frequency of one or several the tagged photon sidebands. (c) After the filter, the untagged photons are greatly reduced in number and arrive promptly at the detector. The tagged photons are transmitted and delayed in time, which enables the use of time gating to remove any further untagged photons not absorbed by the ions in the filter crystal.

In the UOT measurements described in the literature either absorptive filtering [27–29], or absorptive combined with slow light filtering [9] have been used. When the slow light effect is combined with time gating, the filters are often called slow light filters. Note that such filters can be created at a single tagged sideband, or at two (or more) tagged sidebands, as shown in Figure 4.2(b), to increase the tagged signal strength.

The difference in signal (i.e., the contrast) when probing two different tissue locations with ultrasound, while assuming that filters are prepared at the frequencies of the ±1st order tagged photons is:

$$\text{Contrast} = 2S_c\eta_{\text{det}}|N_{\text{T,A}} - N_{\text{T,B}}| \tag{4.2}$$

where $N_{\text{T,A}}$ and $N_{\text{T,B}}$ are the number of +1st order tagged photons emitted from the tissue per unit area at the two probe locations. The tissue area from which photons are collected is denoted S_c, and η_{det} is the detection efficiency, which includes the detector

quantum efficiency, and all other sources of photon loss between the tissue and the detector. Assuming shot-noise-limited detection, the noise is the square root of the total number of photons detected, both tagged and untagged, for the two ultrasound probe pulse locations:

$$\text{Noise} = \sqrt{2S_c\eta_{\text{det}}(N_{\text{T,A}} + N_{\text{T,B}} + T_{\text{U}}N_{\text{U}})} \tag{4.3}$$

where T_{U} is the transmittance of untagged photons through the filter crystal, and N_{U} is the number of untagged photons emitted from the tissue per unit area. The CNR can thus be written as:

$$\text{CNR}_{\text{SHB}} = \sqrt{2S_c\eta_{\text{det}}}\frac{|N_{\text{T,A}} - N_{\text{T,B}}|}{\sqrt{N_{\text{T,A}} + N_{\text{T,B}} + T_{\text{U}}N_{\text{U}}}} \tag{4.4}$$

To improve the CNR, it is thus desirable to minimize $T_{\text{U}}N_{\text{U}}$ by reducing the transmittance of untagged photons by the filter to a level where the noise is dominated by the shot noise of the tagged photons. The filter contrast required to be in this regime depends on the medical application, imaging depth, and detection geometry. As expected, it is advantageous to collect the signal from a large tissue area with a high detection efficiency.

A filter transmittance of untagged photons of $T_{\text{U}} \sim 10^{-3}$ has been used for UOT [9], and the measurements presented in Chapter 5 of this thesis suggest that $T_{\text{U}} \sim 10^{-6}$ may be possible, with the potential for further improvement. For the CNR comparison presented in **Paper VI**, $T_{\text{U}} = 10^{-3}$ or $T_{\text{U}} = 10^{-8}$ was assumed, where the latter is an optimistic, but not unreasonable value of the future performance based on our current understanding. A custom-designed UOT cryostat (from My Cryo Firm) delivered to our group shortly before submitting this thesis has 5.1 cm diameter windows, and allows for 5.1 cm diameter lenses to be mounted inside it. The cryostat is therefore expected to have excellent optical throughput. Detectors and crystals of centimetre size are available. A collection area of 1 cm^2 is deemed possible, and therefore used in the CNR calculations. If the numerical aperture (NA) of the detection set-up is assumed to be 0.7, the signal loss due to the limited collection angle is estimated as $\sin^2(45°) = 0.5$. Photomultiplier tube detectors can have quantum efficiencies of ~ 15% (up to wavelengths of ~ 800 nm). A detection efficiency of $\eta_{\text{det}} = 7.5\%$ was therefore assumed.

4.1.3 Single-shot off-axis holography

Single-shot off-axis holography was recently used for UOT measurements by Liu et al. [8]. The optical field leaving the tissue (tagged and untagged photons) is polarized and illuminates a camera. The camera is also illuminated with a reference field with the

same frequency as one of the tagged sidebands at an angle relative to the field leaving the tissue. Several camera pixels cover each speckle grain, such that the interference fringes in each speckle are resolved. Images are acquired using an exposure that is long compared to the ultrasound period, or a multiple of the ultrasound period, such that the beating between the untagged and reference fields averages out. A 2D fast Fourier transform (FFT) is performed on the recorded camera image. The interference term between the tagged and reference photon fields is shifted away from the centre of Fourier space. The tagged field can then be reconstructed by cropping this region and performing an inverse 2D FFT.

Based on the SNR expression given by Liu et al. [8], which assumes that the amplitude of the untagged and reference fields on the camera are equal and much greater than the amplitude of the tagged field, and that a rectangular iris is used in front of the camera, the shot-noise-limited CNR can be written as:

$$\mathrm{CNR}_{\mathrm{HOL}} = \sqrt{N_{\mathrm{px}}} \frac{\eta_{\mathrm{det}} |\bar{N}_{\mathrm{T,A}} - \bar{N}_{\mathrm{T,B}}| / n_{\mathrm{px}}}{\sqrt{4\eta_{\mathrm{det}} (\bar{N}_{\mathrm{T,A}} + \bar{N}_{\mathrm{T,B}}) / n_{\mathrm{px}} + 2}} \tag{4.5}$$

where $\bar{N}_{\mathrm{T,A}}$ and $\bar{N}_{\mathrm{T,B}}$ are the average number of +1st order tagged photons per speckle at the tissue surface for the two ultrasound pulse probe locations A and B, N_{px} is the total number of camera pixels, and n_{px} is the number of camera pixels covering each speckle. There are two possible CNR scaling regimes, depending on which of the factors $4\eta_{\mathrm{det}}(\bar{N}_{\mathrm{T,A}} + \bar{N}_{\mathrm{T,B}})/n_{\mathrm{px}}$ or 2 in the denominator is larger. The scaling is better at shallow tissue depths where $4\eta_{\mathrm{det}}(\bar{N}_{\mathrm{T,A}} + \bar{N}_{\mathrm{T,B}})/n_{\mathrm{px}}$ can be larger. Increasing the camera pixel count to detect more speckles, and/or improving the detection efficiency will improve the CNR.

The following set-up parameters were chosen for the theoretical CNR comparison presented in **Paper VI**. To the best of the author's knowledge, currently available low-noise, ~ kHz frame rate cameras have sensors with a few Mpx. A 1 Mpx or a 50 Mpx camera was assumed, with a pixel quantum efficiency of 60%. The signal is maximized when the speckle size is 4 pixels wide [8], and it was therefore assumed that $n_{\mathrm{px}} = 16$. For off-axis holography, the number of photons per speckle (per camera pixel) is relevant. Setting the NA of the detection set-up to 0.7, means that the signal loss due to the limited collection angle is again estimated to be 0.5. However, the smallest possible speckle area that can be recorded on the camera should be proportional to $1/\mathrm{NA}^2$. For an NA of 0.7, the smallest possible speckle on the camera is therefore twice the speckle area at the tissue surface. Thus, the number of photons per speckle on the tissue surface and on the detector is identical. The polarizer used in front of the camera in the off-axis holography set-up reduces the signal by half, which, when combined with the pixel quantum efficiency, gives $\eta_{\mathrm{det}} = 30\%$.

4.1.4 Speckle contrast

The speckle contrast is defined as the standard deviation of the speckle pattern divided by the mean intensity. When an ultrasound pulse enters the tissue, the speckle contrast will decrease, i.e., the speckle pattern will become blurred. The decrease in contrast depends on the ratio of tagged to untagged photons. A camera is used to record the speckle pattern with a single exposure that is either long compared with the ultrasound period, or an integer number of ultrasound periods, as in the case of single-shot off-axis holography above. The exposure should be short compared to the speckle decorrelation time, since tissue movement also reduces the speckle contrast.

For $N_T \ll N_U$, and the ideal case of linearly polarized speckle patterns with contrast close to unity, Resink et al. [57] derived the following expression for the decreased speckle contrast.

$$C = 1 - \frac{2N_T}{N_U} \tag{4.6}$$

This expression is similar to that presented by Li et al. [49]. It should be noted that the speckle contrast is usually significantly less than unity in experiments. The algorithm presented by Duncan et al. [19] was used to estimate the noise due to statistical variation in speckle contrast for speckle patterns where the speckle size was two pixels wide. The standard deviation of the contrast of many simulated speckle patterns was found to be $\approx \sqrt{1/N_{px}}$. The CNR can therefore be expressed as follows.

$$\mathrm{CNR}_{SC} = \sqrt{2N_{px}}\frac{|N_{T,A} - N_{T,B}|}{N_U} \tag{4.7}$$

Thus, the CNR is improved by increasing the number of camera pixels used in order to detect more speckles. As only statistical variations in the speckle contrast are considered in Equation (4.7), this should be considered as an upper limit on the CNR. Although the detection efficiency η_{det} is not included in Equation (4.7), it must also be optimized for the speckle contrast method, since sources of camera noise at low light levels and at high readout rates will probably be relevant.

A similar camera to that used in single-shot off-axis holography could be used in the speckle contrast method, and a 1 Mpx or a 50 Mpx camera was therefore assumed in the CNR analysis in **Paper VI**.

4.1.5 Photorefractive detection

Materials such as crystals and polymers [58], that exhibit the photorefractive effect can be used to detect either tagged or untagged photons in UOT. A set-up that detects

untagged photons (and thus indirectly tagged photons) was included in **Paper VI**, and will therefore be discussed here.

The scattered output from the tissue (tagged and untagged) and a reference beam at the same frequency as the untagged photons are overlapped at an angle in the photorefractive material. Interference generates spatially varying intensity in the material, which alters the refractive index through the photorefractive effect. The reference beam is diffracted by the refractive index grating with an efficiency η_{pr} and interferes with the scattered field on a single-point detector. The tagged photons are indirectly detected by turning the ultrasound on and off and comparing the two signals. Assuming negligible deccorelation of the tagged photon field, Gross et al. [59] derived an expression for the difference in intensity when the ultrasound is on and off: $\Delta I = 2\eta_{\mathrm{pr}}|E_{\mathrm{T}}|^2$, where E_{T} is the amplitude of the +1st order tagged photon field. The image contrast can thus be written as:

$$\text{Contrast} = 2S_{\mathrm{c}}\eta_{\mathrm{det}}\eta_{\mathrm{pr}}|N_{\mathrm{T,A}} - N_{\mathrm{T,B}}| \tag{4.8}$$

The total intensity without ultrasound is $I = |E_{\mathrm{U}} + E_{\mathrm{D}}|^2$, where E_{U} is the amplitude of the untagged photon field in the absence of the ultrasound, and E_{D} is the amplitude of the diffracted field, with $E_{\mathrm{D}} \simeq \eta_{\mathrm{pr}}E_{\mathrm{U}}$ [59]. The noise can thus be written:

$$\text{Noise} = \sqrt{2S_{\mathrm{c}}\eta_{\mathrm{det}}N_{\mathrm{U}}(1+\eta_{\mathrm{pr}})^2} \tag{4.9}$$

and the CNR can then be expressed as:

$$\mathrm{CNR_{PR}} = \sqrt{2S_{\mathrm{c}}\eta_{\mathrm{det}}}\frac{\eta_{\mathrm{pr}}|N_{\mathrm{T,A}} - N_{\mathrm{T,B}}|}{\sqrt{N_{\mathrm{U}}(1+\eta_{\mathrm{pr}})^2}} \tag{4.10}$$

To improve the CNR, it is thus desirable to optimize η_{pr}, and to collect signal from as large a tissue area as possible, with maximum detection efficiency. It should be noted that light in the reference beam scattered in the direction of the detector by crystal imperfections is a potential source of noise not considered above.

Photorefractive materials with response times of the order 100 ms have been used in several UOT experiments [52, 54, 60], however, these are not suitable for *in vivo* measurements since the decorrelation of speckles in tissues is much faster. However, materials with faster response times have been used for photorefractive detection. A response time of 1 ms and $\eta_{\mathrm{pr}} = 15\%$ are possible using GaAs crystals [53], and $Sn_2P_2S_6$:Te crystals have a response time of a few ms [61]. For the CNR analysis in **Paper VI** $\eta_{\mathrm{pr}} = 15\%$ or $\eta_{\mathrm{pr}} = 35\%$ was used. The accurate prediction of potentially improved photorefractive response times and efficiencies is, however, outside the scope of this work. Similarly to spectral hole burning, a collection area $S_{\mathrm{c}} = 1$ cm^2 should

be reasonable bearing in mind the available crystal and detector sizes for photorefractive detection. With a value of NA of 0.7, the signal loss due to the limited collection angle is again 0.5. As the photorefractive method detects small signal variations on a relatively high background, a photo diode with a quantum efficiency of 80% can be used. Thus, a detection efficiency of $\eta_{\mathrm{det}} = 40\%$ was assumed.

4.2 Comparison of contrast-to-noise ratios of UOT methods

This section presents a comparison of the CNR of the spectral hole burning, single-shot off-axis holography, photorefractive detection, and speckle contrast methods.

4.2.1 Calculating tagged and untagged signal strength

The Monte Carlo and ultrasound tagging code package described in **Papers III** and **IV** was used to simulate the tagged and untagged photons. Only a brief overview of the simulation process is given here, and the reader is referred to the relevant papers, and the simulation code available online [62]. Readers who are interested in further details can consult the Ph.D. thesis by David Hill, who developed the code, which should be available from the Department of Physics at Lund University after December 2022. Note that the simulations carried out in the present work are similar to those of Huang et al. [63].

The Monte Carlo method [64] is used to generate photon packet paths from an input to a detection area through a simulation domain with a given scattering coefficient μ_{s}, anisotropy factor, g, refractive index, and zero absorption. The ultrasonically induced changes in the local refractive index and the scattering locations are then calculated, and used to determine how the ultrasound field modulates the optical path length of each photon packet. The power spectrum of each photon path is calculated, and photon absorption is accounted for via the Beer-Lambert law [Equation (2.1)] based on the photon packet trajectory. The total spectrum is obtain by calculating the mean of the spectra of all detected photon packets, and used to calculate the transmittance of tagged and untagged photons from the input to the detection area.

The simulation geometry shown in Figure 4.3 was used in the comparison of CNRs presented in **Paper VI**. An optical wavelength of 800 nm was assumed. The simulated tissue had a scattering coefficient of $\mu_{\mathrm{s}} = 50\ \mathrm{cm}^{-1}$, an absorption coefficient of $\mu_{\mathrm{a}} = 0.2\ \mathrm{cm}^{-1}$, an anisotropy factor of $g = 0.9$, and a refractive index of $n = 1.3$. These properties are similar to those of muscle tissue (see Chapter 2). An inclusion measuring $3 \times 3 \times 3\ \mathrm{mm}^3$ with the same optical properties as the background tissue,

except for $\mu_a = 0.4\ \text{cm}^{-1}$, was added at an imaging depth, z. Such an inclusion could be, but is not necessarily, a region of cancerous tissue.

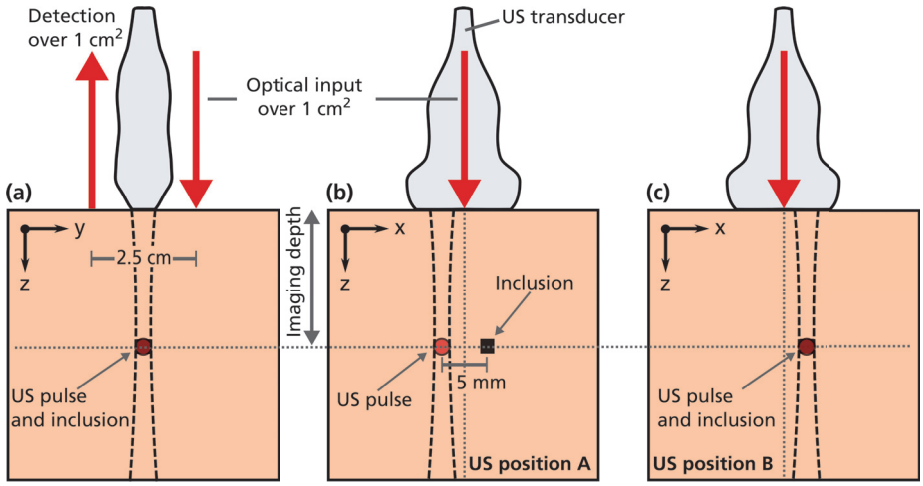

Figure 4.3: Simulation geometry used to compare the CNR of various UOT detection methods. (a) z-y view (b) z-x view when the ultrasound (US) pulse is in position A. (c) z-x view when the ultrasound pulse is in position B.

It was assumed that a UOT image of 30×30 voxels was acquired in 1 s. The maximum permissible laser exposure of 300 mW/cm^2 for average radiation at 800 nm [65] limits the total number of input photons for image acquisition to $\sim 10^{18}$. The number of photons delivered to the tissue per image voxel was therefore 10^{15} in the present case. The photon packets were launched and detected over areas of 1 cm^2 separated by 2.5 cm. The transmittance of tagged and untagged photons from the input to detection was calculated with an ultrasound field at position A and B, as shown in Figure 4.3(b) and (c), respectively. The ultrasound field was assumed to have a centre frequency of 3 MHz, a peak pressure of 2 MPa, and a Gaussian pressure distribution with dimensions of $3 \times 3 \times 3$ mm^3 at full-width-at-half-maximum (FWHM). The number of tagged and untagged photons emitted through the detection area for ultrasound field locations A and B was calculated by multiplying the calculated transmittances by the number of input photons (10^{15}), and then used as input for the expression of CNR for the respective method. The calculations were repeated with the ultrasound field and inclusion at various imaging depths. A speckle diameter of 600 nm was used to calculate the number of photons per speckle at the tissue surface, which should be suitable for the 800 nm laser wavelength [66]. The set-up parameters specific to each UOT method have been given above in the sections describing each method.

As discussed in **Paper VI**, the simulated tagged and untagged photon signals depend

on several input parameters. The simulated signals depend exponentially on the optical scattering and absorption coefficients, and these therefore have a large impact on the CNRs. As in the case of other imaging modalities, a trade-off is necessary between image resolution (determined by the ultrasound volume) and imaging depth. The maximum permissible laser exposure to human tissue is given per cm^2, so the total laser input power can be increased above that used here by illuminating a larger tissue area. The CNRs can be improved by allowing longer measurement times and averaging. The detection efficiency has a small effect on the CNRs. However, the relative imaging performance of each detection method is given in this comparison, which should not be greatly affected by changes in the parameters mentioned above.

4.2.2 Results and discussion

The main results of this comparison of CNR are shown in Figure 4.4. It can be seen that spectral hole burning has the potential to image greater tissue depths than the other methods investigated. This is due to better CNR scaling, and the large detection etendue. At imaging depths < 2 cm, the noise is dominated by the shot noise of the tagged photons with both the 30 dB ($T_U = 10^{-3}$) and 80 dB ($T_U = 10^{-8}$) filters, hence the CNR is the same. At imaging depths > 2 cm, the shot noise of the untagged photons starts to dominate with the 30 dB filter, leading to a change in CNR scaling, while in the case of the 80 dB filters the noise is still dominated by tagged photons down to a depth of ~ 5 cm. The simulated maximal imaging depth for this case is 3.3 cm with the 30 dB filter and 4.5 cm with the 80 dB filter. This highlights the importance of improving the filter contrast beyond the 30 dB that has been used in experiments so far. It should, however, be noted that a transmission geometry (where input and detection are on opposite sides of the tissue) would relax the required filter contrast for being in the regime where the noise is dominated by tagged photons. In transmission mode, the numbers of both tagged and untagged photons will decrease with increasing thickness of the imaged tissue. This is not the case in the reflection mode used here (Figure 4.3), where only the number of tagged photons decreases with imaging depth.

The untagged photons dominate the noise in the case of the photorefractive detection set-up presented here. Although the method has the same etendue and better detector efficiency than spectral hole burning in the current example, the CNR is therefore not as good as in the spectral hole burning method. Note that in the presented simulation geometry, the ~ 2.3 cm imaging depth achieved equates to a shortest photon path from the optical input to detection of ~ 5.3 cm. Since the untagged photons dominate the noise in photorefractive detection, transmission mode would be more favourable, and further studies could be performed to evaluate this. The conclusion

drawn from the results is that photorefractive detection could likely be used to image tissue thicknesses significantly greater than ~ 5.3 cm in transmission geometry, assuming that the other simulation parameters are the same. Photorefractive detection thus has good potential for high CNRs at significant tissue depths.

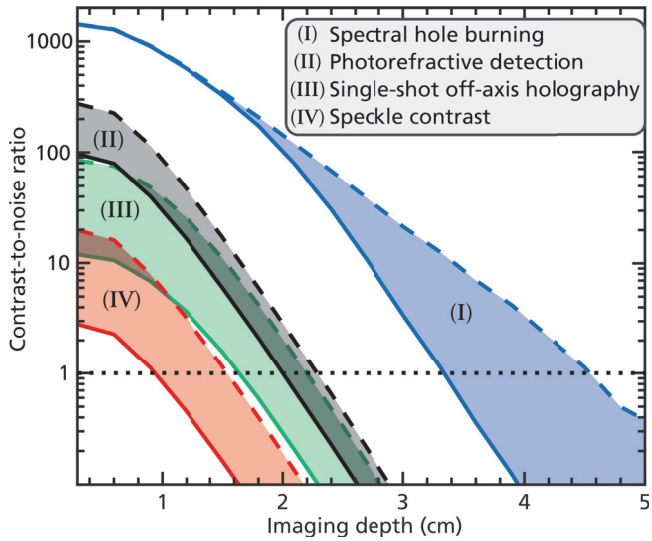

Figure 4.4: Contrast-to-noise ratios of the methods investigated. Note that the scale on the y-axis is logarithmic. **(I)** Spectral hole burning assuming an untagged filter transmittance of $T_U = 10^{-3}$ (solid blue line) and $T_U = 10^{-8}$ (dashed blue line). **(II)** Photorefractive detection assuming a photorefractive efficiency of $\eta_{pr} = 0.10$ (solid black line) and $\eta_{pr} = 0.35$ (dashed black line). **(III)** Single-shot off-axis holography assuming a camera pixel count of $N_{px} = 1$ Mpx (solid green line) and $N_{px} = 50$ Mpx (dashed green line) **(IV)** Speckle contrast assuming $N_{px} = 1$ Mpx (solid red line) and $N_{px} = 50$ Mpx (dashed red line). To be able to distinguish a difference in absorption, the CNR must be greater than 1, indicated by the horizontal dotted black line.

The camera-based methods (off-axis holography and speckle contrast) have a lower detection etendue than the other methods investigated. However, the etendue (and thus the CNR) could be improved by increasing the pixel count in the camera. The accurate prediction of the future performance of high-pixel-count, low-noise, $\gtrsim 1$ kHz frame rate cameras is outside the scope of this work, however, some observations can be made. Increasing the pixel count will lead to the generation of large amounts of data that must be transferred from the camera and then analysed (for example, by performing 2D FFTs in off-axis holography). The spectral hole burning and photorefractive methods produce much less data, and the analysis is simpler due to the use of single-element detectors. The UOT frame rate is important since averaging improves the CNR, and it is important that these methods are not slowed down when increasing camera pixel counts. In off-axis holography, the average number of tagged photons detected per pixel is always less than ~ 1 in the current example. The method is therefore in the unfavourable CNR scaling regime (see Section 4.1.3). Even if the method

had a similar etendue to that in spectral hole burning, the same imaging depths could not be achieved. The speckle contrast method exhibit the lowest CNR of the methods investigated. The random variations in speckle contrast rapidly becomes larger than the signal with increasing imaging depth. The optimistic assumptions made in deriving Equation (4.7) mean that the imaging depth is potentially overestimated.

As concluded in **Paper VI**, the spectral hole burning method appears to be very promising for UOT in terms of imaging deeper inside the human body, provided that high-contrast filters at wavelengths suitable for biomedical applications can be identified.

4.3 Ultrasound optical tomography using Pr^{3+}:Y_2SiO_5 filters

The $^3H_4$-$^1D_2$ transition in Pr^{3+}:Y_2SiO_5 has several favourable spectroscopic properties that have enabled the preparation of 53 dB contrast filters for a collimated laser beam [10] and ~ 30 dB contrast filters for experimental UOT [9]. Although the 606 nm operating wavelength of such filters is not optimal for imaging in real biological tissues, due to poor penetration depth, measurements on tissue phantoms are useful for the further development of the UOT technique in general.

4.3.1 Preparing spectral hole burning filters in Pr^{3+}:Y_2SiO_5

Yttrium orthosilicate, Y_2SiO_5, has been frequently used as a rare-earth-ion host for applications at cryogenic temperatures due to the narrow homogeneous linewidths often observed in this host. This is because the most abundant isotopes of Si and O have no nuclear magnetic moment, and yttrium has a low nuclear magnetic moment of $-0.137\mu_N$, where μ_N is the nuclear magneton [34]. This minimizes homogeneous linewidth broadening for the rare-earth dopants due to spin flips by host ions. The crystal system of Y_2SiO_5 is monoclinic, and the crystal is thus biaxial, with three principal axes labelled D_1, D_2, and C_2, with slightly different refractive indices [67]. Rare-earth ions occupy two different sites of C_1 symmetry with a ~ 2 nm difference in transition wavelength. All further discussion considers ions at site 1 with transition frequencies around 494.726 THz (vacuum wavelength of 605.977 nm).

Pr^{3+} has nuclear spin $I = 5/2$, and each electronic level can therefore split into six hyperfine states. However, in the absence of a magnetic field, there are three doubly degenerate levels. An energy level diagram showing the hyperfine structure of site 1 of the $^3H_4$-$^1D_2$ transition is shown in Figure 4.5(a). The optical homogeneous linewidth is Γ_h ~ 2 kHz [68], and the hyperfine states can have lifetimes of ~ 100 s [69]

(magnetic field and temperature dependent). For a doping concentration of 0.05%, the peak absorption coefficients are 3.6 cm^{-1}, 47 cm^{-1}, and < 0.1 cm^{-1}, of light polarized along D_1, D_2, and C_2, respectively [70].

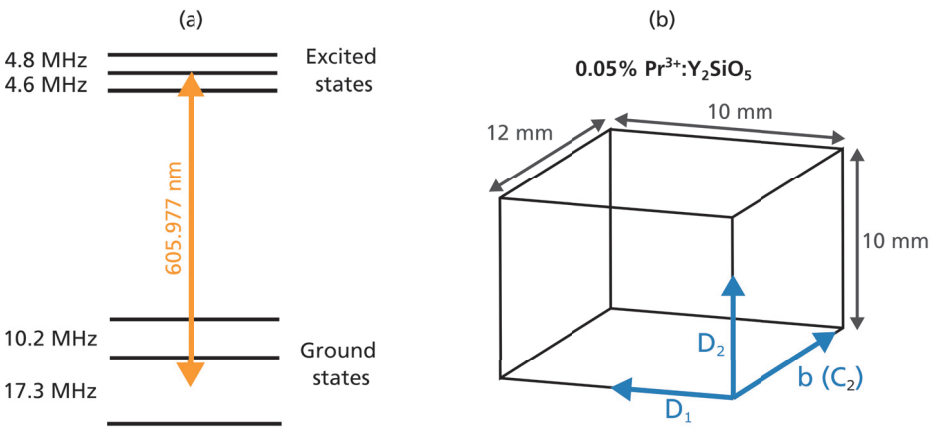

Figure 4.5: (a) Energy level structure of the $^3H_4$-$^1D_2$ transition. (b) Orientation and dimensions of the $0.05\%Pr^{3+}:Y_2SiO_5$ crystal used for UOT measurements.

The $0.05\%Pr^{3+}:Y_2SiO_5$ crystal used in this work is a cuboid with dimensions $10 \times 10 \times 12$ mm^3. The sides are cut parallel to the principal axes, as shown in Figure 4.5(b). Note that the C_2 principal axis is parallel to the crystal b-axis, and is therefore often denoted as the b-axis instead. In a UOT experiment, the beam to be filtered should preferably propagate along the b-axis, due to the low absorption of light polarized along this axis. Since the absorption is only high for light polarized along D_2, it is necessary to use a polarizer before the crystal to achieve good filter contrast. Configurations with crossed crystals may eliminate the need for polarizers [10], but have not yet been investigated.

To prepare 1 MHz wide square-shaped UOT filters, a frequency-scanned pulse called a hyperbolic-square-hyperbolic or sechscan pulse was used [71]. This is a hyperbolic secant (sechyp) pulse with a linear frequency scan in the middle. The pulse parameters were chosen based on simulations and experiments by M. Di, see her Master's thesis for more details [72]. The linear frequency scan was 0.92 MHz during 92 µs. The intensity profile for the sechyp envelope (FWHM) was 8 µs, and the sechyp frequency width was 80 kHz. The total pulse duration was 140 µs. In total, 2000 or 3900 such pulses separated by 200 µs were used to create the filters in the UOT experiments described in Section 4.3.4 and Section 4.3.5, respectively. The diameter of the laser beam was slightly larger than 10 mm, and the peak power was ~ 10 mW. The polarization was aligned parallel to the D_2 axis.

4.3.2 Tissue-mimicking phantoms

Phantoms that mimic the properties of biological tissues are important in UOT measurements, and for characterizing medical imaging systems in general. The tissue-mimicking phantoms used in the present work were made using deionized water, agar powder, Intralipid-20% (a fat emulsion), and India ink, and inspired by the procedure described by Cubeddu et al. [73].

To prepare phantoms with homogeneous optical properties, agar powder and deionized water (1 g per 97.5 ml) was first mixed in a glass beaker. The mixture was heated under magnetic stirring to ~ 95°C, and kept at this temperature for about 1 hour. The heating was thereafter turned off, while the stirring continued. When the mixture had cooled to ~ 45°C, the desired amounts of Intralipid-20% and India ink was added. The mixture was stirred for another 30 minutes at ~ 45°C, before being transferred to a container and stored in a refrigerator to allow solidification. The photon time-of-flight system developed by the Biophotonics Group at Lund University [74] was used to determine the absorption coefficient and reduced scattering coefficient (μ_a and μ_s') of the phantom. Typically, Intralipid-20% and water were mixed in the ratio 1 : 39 to obtain solid phantoms with a reduced scattering coefficient of about 6 cm^{-1} at 606 nm. Reference values for the optical absorption and reduced scattering of Intralipid and India-ink-based liquid phantoms can be found in the literature [75].

To prepare phantoms with optically absorbing inclusions, the above procedure was performed layer by layer. A bottom layer was first prepared and solidified. An absorbing inclusion was cut to the desired dimensions from a separate phantom prepared with the same scattering properties, but a different absorption coefficient. The absorbing inclusion was placed on the bottom layer. A mixture with the same optical properties as the bottom layer was then prepared, and poured over the inclusion and bottom layer, and then allowed to solidify. Examples of tissue-mimicking phantoms containing optically absorbing inclusions are shown in Figure 4.6.

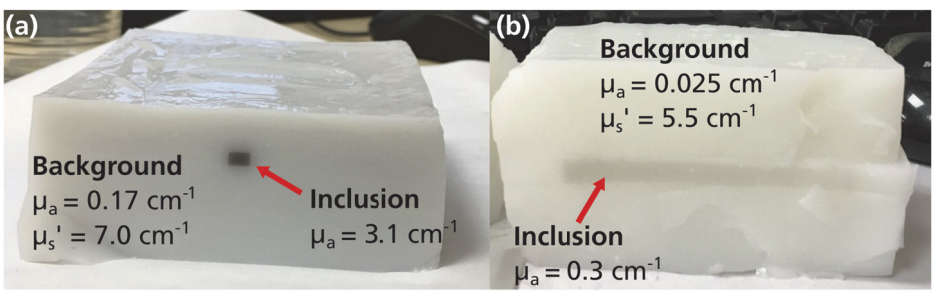

Figure 4.6: Examples of tissue-mimicking phantoms cut to make the inclusion visible. (a) A tissue-like phantom containing an inclusion. (b) Typical phantom used in the UOT experiments.

4.3.3 Ultrasound field

The ultrasonic source was an EPIQ-7 ultrasound scanner used with the X5-1 or L12-3 transducers (Philips Medical Systems (PMS), Bothell, WA, USA). The ultrasound pulses used in each UOT experiment were characterized by mounting the transducer and a needle hydrophone in a water tank. The acoustic pressure was measured by systematically scanning the hydrophone.

4.3.4 Characterization and modelling of signal strengths

Theoretical models that accurately predict the strengths of tagged and untagged signals are useful for improving our understanding of the potential imaging capabilities of an optimized UOT set-up. Such models were developed and validated against experimental measurements, and the results presented in **Papers I, III, & IV**. To ensure accurate comparisons with theory, it is important to perform the experiments under well controlled conditions, with a good understanding of each part of the set-up. This includes characterizing the optical loss in each part of the set-up, the detector efficiency, the acoustic pressure distribution of the ultrasound pulse, and the optical properties of the tissue-mimicking phantoms. The main UOT experiments are presented below. Details concerning each component can be found in the papers; **Paper I** in particular.

Experimental set-up

The experiments presented in **Papers I, III, & IV** were carried out in the transmission geometry illustrated in Figure 4.7. The laser system provided sub-kHz linewidth light at the $^3H_4$-$^1D_2$ transition wavelength. Optical pulse shaping was performed using acousto-optic modulators. A flip mirror was used to switch between the burn and probe beams that were used to prepare the crystal filter, and probe the phantom, respectively. The filter was prepared using 2000 of the pulses described in Section 4.3.1. The transmission in the filter passband was 60%, while the attenuation at a frequency detuning of ≥ 1.6 MHz was > 30 dB. After the filter had been prepared, the phantom was probed up to 100 times, after which the filter was refreshed. Each ultrasound pulse was synchronized so as to arrive at the centre of the phantom at the same time as an optical pulse with a peak power of 25 mW, and duration of 1 µs was incident on the phantom. The phantom had dimensions of $7.0 \times 7.0 \times d_\mathrm{p}$ cm^3, where d_p is the phantom thickness, and homogeneous optical properties (as given in the figure captions). A light guide in direct contact with the phantom together with lenses was used to collect the photons emitted from the phantom, and direct them towards

the crystal mounted inside the cryostat (Spectromag 4000-8, Oxford Instruments) at 2.17 K. Since Pr^{3+}:Y_2SiO_5 only has high absorption along the D_2 axis, and thus only provides a good filter for one optical polarization, polarizers were used before and after the cryostat. A mechanical shutter was used to protected the signal detector, a photomultiplier tube (PMT), from overexposure during filter preparation.

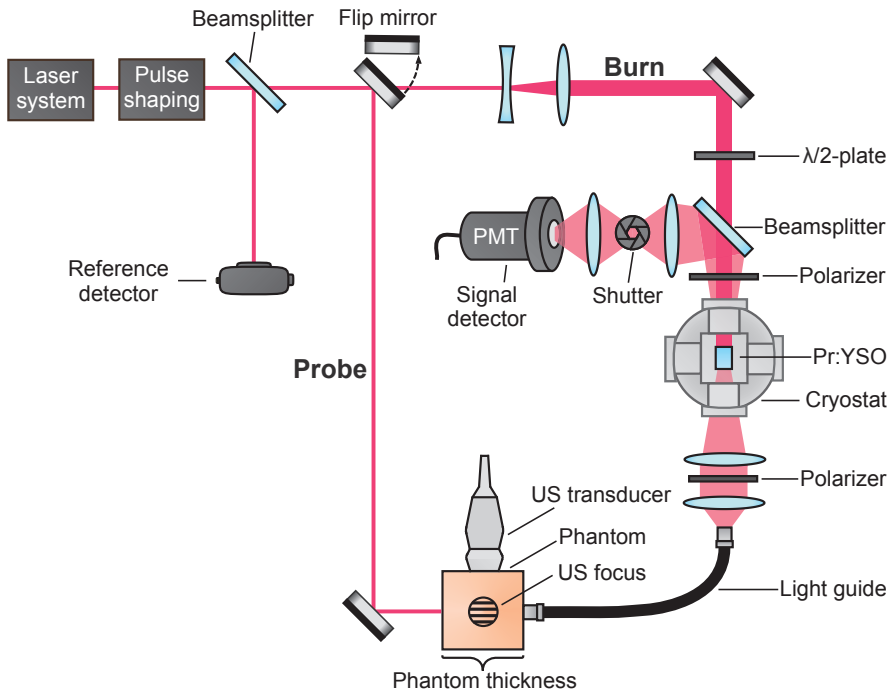

Figure 4.7: Experimental set-up used to measure ultrasound (US) tagged signals in transmission mode. Reprinted with permission from **Paper I** ©Optica Publishing Group.

The optical throughput of the set-up was very low. Measurements showed that only 0.05% of the photons emitted from the light guide were incident on the PMT detector. The major factor contributing to photon loss was the cryostat. This is a large instrument with small windows, and is far from optimal for applications requiring a high etendue. The anode radiant sensitivity of the PMT detector was measured with a 10 mm diameter top-hat beam to mimic the UOT experiment. This allowed conversion of the detector output current to incident optical power. Based on the measured anode radiant sensitivity, the quantum efficiency was calculated to be 1.7%. This set-up was thus far from ideal in terms of detection efficiency. The detection efficiency was greatly improved in the experiments presented in Section 4.3.5, and further improvements are discussed in Section 4.4.

Dependence of signal strength on phantom thickness

The tagged signals detected from a 3.5 and a 6.8 cm thick phantom are shown in Figure 4.8(a) and (b), respectively. It was verified that ultrasound-tagged photons were detected by switching the ultrasound source on and off. Time zero in Figure 4.8(a) and (b) corresponds to the arrival time of the probe pulse at the reference detector. The untagged photons not absorbed by the crystal also arrived very close to time zero. However, the tagged photons were delayed by about 5.6 µs. Therefore, the speed of light in the filter material was ~ 2000 m/s. Although the signal strengths were low due to the low efficiency of the set-up, Figure 4.8(a) shows that the high-contrast filter allowed for almost background-free measurements of the tagged signal. This was used to characterize the tagged signal strength for different phantom thicknesses, as shown in Figure 4.8(c). The untagged signal strength was also measured by preparing the filter at the frequency of the untagged photons.

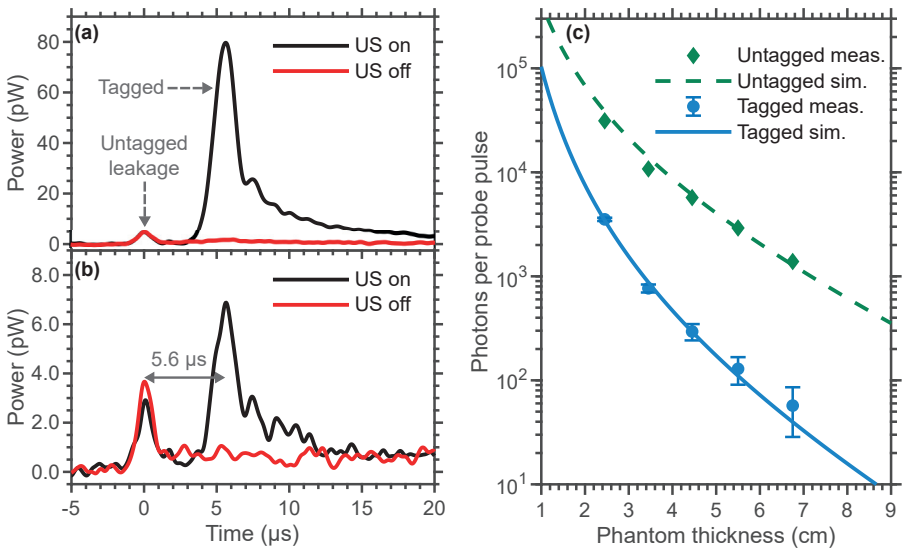

Figure 4.8: (a) Optical power incident on the detector when using a 3.5 cm thick phantom. (b) Optical power incident on the detector when using a 6.8 cm thick phantom. Note the difference in power scales. (c) Tagged and untagged signals from phantoms of various thicknesses. The phantoms used for the measurements presented in this figure had $\mu_a = 0.008$ cm^{-1} and $\mu_s' = 6.1$ cm^{-1}. The ultrasound pulse had a centre frequency of 1.6 MHz, a peak compression and rarefaction pressure of 4.3 and 2.0 MPa, respectively, and dimensions $4 \times 4 \times 2$ mm^3 (at half-pressure). The signals were obtained by averaging 1000 probe pulses. The error bars in (c) display the standard error. The standard errors for the untagged photons are smaller than the symbols and therefore not included. Adapted with permission from **Paper I** ©Optica Publishing Group.

The measured tagged and untagged signal strengths were compared to calculations using the 1D diffusion approximation with extrapolated boundary conditions. The untagged signal levels were modelled according to Wang [76]. Note that this calcula-

tion contains no fitting parameters. The tagged signal was modelled with the approach described by Walther et al. [7]. The photon fluence [cm^{-2}] due to a small-diameter laser beam was calculated at the position of the ultrasound pulse. The fluence was multiplied by a factor κ, which determined the number of tagged photons located at the ultrasound position. Note that the cross-sectional area of the ultrasound pulse is significantly smaller than 1 cm^2, and that κ should not directly be interpreted as the fraction of photons that pass through the ultrasound pulse that become tagged. The 1D diffusion approximation was once again used to calculate the flux across the phantom boundary at the light guide position. The transmittance of the set-up was then taken into account to obtain the results shown in Figure 4.8(c). Good agreement was obtained between the simulation and experimental data with $\kappa = 0.026$ cm^2.

The experimentally fitted model was used to calculate the tagged signal strengths in a theoretically optimized set-up using optical properties similar to muscle (μ_a = 0.2 cm^{-1} and $\mu_s' = 5$ cm^{-1}, see Chapter 2) and breast tissue ($\mu_a = 0.05$ cm^{-1} and $\mu_s' = 11$ cm^{-1} [77]). In the optimized set-up, it was assumed that the transmission from the light guide output to the detector (see Figure 4.7) was improved to 20%. The laser power was increased to the medical safety limit assuming a 1 cm^2 area of laser irradiation and a 25 kHz probe repetition rate. The filter transmittance of the $\pm$1st order tagged photons was set to 100%.

The calculated tagged signals for this optimized set-up are shown in Figure 4.9, indicating that 100 tagged photons would be incident on the detector per probe pulse through 9 cm of muscle and 12 cm of breast tissue. The ultrasound pulse depth was assumed to be half the tissue thickness in the calculations (as in the experimental measurements). If the filter is assumed to suppress the untagged photons to a point where the noise is dominated by tagged photons, the shot-noise limited SNR for a single-point measurement could be estimated as the square root of the total number of detected tagged photons. Assuming a 15% detector quantum efficiency and the average of 200 signals (which would take 8 ms at the 25 kHz probe rate), an SNR of about 55 could be obtained for the calculated signal level of 100 tagged photons per probe pulse. It should be borne in mind that the ability to detect changes in the signal is more relevant in UOT (see discussion on CNR in Section 4.1.1). However, the potential of signals of ~ 100 tagged photons per probe pulse through ~ 10 cm thick tissues (~ 5 cm ultrasound depth) seems promising. As concluded in **Paper I**, these results allow us to assert the potential to image deep inside human tissue with great confidence, and is important for future experimental and theoretical comparisons.

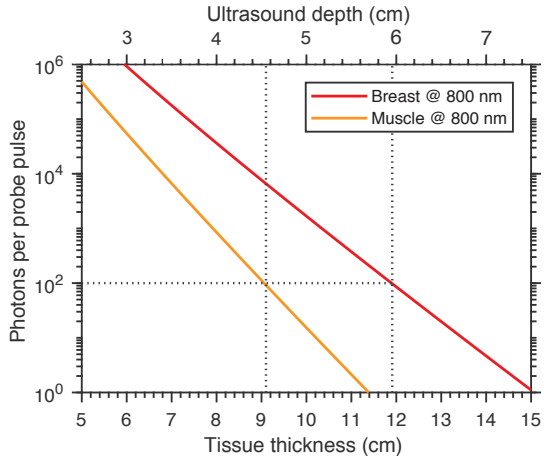

Figure 4.9: Simulated number of tagged photons incident on the detector per probe pulse for an optimized UOT transmission geometry. The ultrasound depth from which tagged photons are generated was set to half the tissue thickness. Reprinted with permission from **Paper I** ©Optica Publishing Group.

Signal strength for arbitrary acoustic fields

A limitation of the results presented in **Paper I**, is that they are based on the free parameter, κ, describing the efficiency of the tagging process, which depends on the particular ultrasound pulse used (acoustic peak pressure, volume, frequency, etc.). A model that calculates the signal strengths from first principle for arbitrary acoustic fields is desirable. This was investigated by measuring the intensities of the +1st and +2nd order tagged sidebands, and untagged carriers, as a function of acoustic peak pressure for various ultrasound pulse volumes and frequencies, and comparison with simulations. The results are presented in **Papers III & IV**.

The tagged fraction η_{n} was defined as:

$$\eta_{\mathrm{n}} = \frac{I_{\mathrm{n}}}{I_{\mathrm{Ref}}} \tag{4.11}$$

where I_{n} is the intensity measured in the n-th sideband, and I_{Ref} is the intensity measured in the untagged carrier without the ultrasound pulse present in the phantom. The total tagged fraction η_{all} was defined as:

$$\eta_{\mathrm{all}} = \frac{I_{\mathrm{Ref}} - I_{\mathrm{o}}}{I_{\mathrm{Ref}}} \tag{4.12}$$

Examples of measurements using a 1.6 MHz centre frequency ultrasound pulse with dimensions $4 \times 4 \times 2$ mm^3 (at half pressure) are shown in Figure 4.10. The measured

values are compared with simulations from first principle using the Monte Carlo-based tagging model briefly described in Section 4.2.1. For further details, see **Paper III**, and the simulation code [62]. In general, good agreement was seen between the simulation (blue lines) and the measured values (symbols) for the tagged fractions. However, at higher ultrasound peak pressures (> 1 MPa), there was a discrepancy between the measured and simulated values of the total tagged fraction η_{all}. Further measurements using smaller ultrasound volumes and/or a 3.5 MHz ultrasound centre frequency showed similar results, with good agreement between the simulated and measured values of η_1 and η_2, but a lower value of η_{all} than the measured values (**Paper III**). As yet, there is no explanation for this discrepancy, and this must be further investigated.

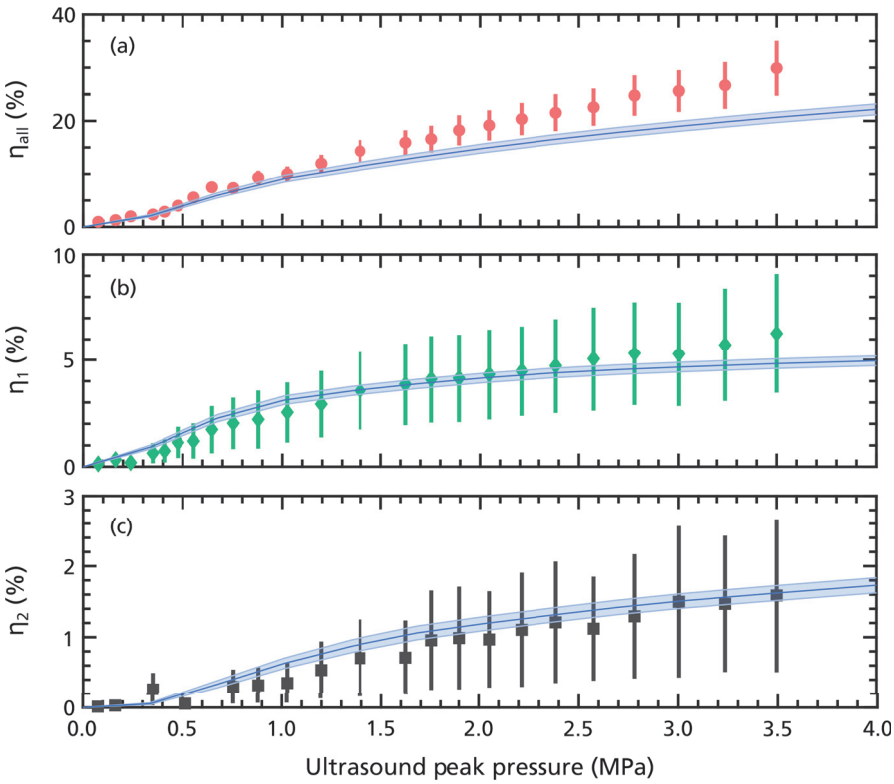

Figure 4.10: Tagged fraction in (a) all sidebands (b) the +1st order sideband (c) the +2nd order sideband. The symbols are experimental data, with error bars showing one standard deviation. The blue lines are the simulated tagged fractions with the shaded area showing the standard error. An ultrasound pulse with a centre frequency of 1.6 MHz, and dimensions of $4 \times 4 \times 2$ mm^3 (at half pressure) was used. The phantom was $d_p = 3.8$ cm thick, with $\mu_a = 0.008$ cm^{-1} and $\mu_s' = 6.4$ cm^{-1}. The signals for each ultrasound peak pressure was obtained by averaging 1000 probe pulses. Adapted with permission from **Paper III** ©Optica Publishing Group.

The ~ 30% decrease in the carrier intensity when applying the ultrasound field seen in

Figure 4.10(a), means that a very large fraction of photons passing through the ultrasound pulse are tagged. This was initially surprising. However, a study by Huang et al. [63] also showed high tagging efficiencies. In their measurements, 70% of the photons that traversed the ultrasound were tagged using a 1 MHz ultrasound frequency with 0.47 MPa peak pressure.

The results in Figure 4.10 also show that there can be significant signal in the 2nd order tagged sidebands. These are photons that are shifted twice by the fundamental ultrasound frequency, or once by the harmonic of the ultrasound pulse. There may also be some signal in the 3rd order sidebands, although these photons were not measured. Preparing filters that transmit both the ±1st and ±2nd order tagged photons could thus be considered to maximize the signal. Imaging with 2nd order tagged photons has been performed to achieve better spatial resolution [78]. Using the 2nd order would also reduce the requirements on the spectral hole burning filter bandwidth, and could be investigated further.

Measurements of the tagged fractions were presented above, and in **Paper III**. However, it should be noted that the Monte Carlo-based tagging simulation can be used to calculate the absolute number of tagged and untagged photons (as done in the CNR comparison presented in **Paper VI**). The Monte Carlo-based tagging simulation was compared to the results shown in Figure 4.8 (in unpublished calculations by D. Hill). The Monte Carlo simulation underestimated the number of +1st order tagged and untagged photons by a factor of < 1.5 compared to the experimental measurements and diffusion equation calculations. A first-principle model that predicts the tagged and untagged UOT signals to this accuracy is useful for theoretical investigations of the imaging capabilities of UOT in various medical applications. **Paper IV** describes how the model could be extended, from simulating single-point measurements, to 1D images (or more) of inhomogeneously absorbing tissues.

4.3.5 Imaging of optically absorbing inclusions

This section presents preliminary data from UOT imaging experiments on optically absorbing inclusions inside scattering phantoms. Transmission mode has been used in UOT measurements using spectral hole burning detection presented in the literature, whereas reflection mode was used here, as it was deemed more generally applicable for most medical applications.

Experimental set-up

The same laser and pulse shaping system was used in these experiments as in the transmission mode measurements presented in Section 4.3.4. There are, however, some key differences, as shown in Figure 4.11. A significantly higher collection efficiency was achieved by using a small, high etendue cryostat (Optistat CFV, Oxford Instruments), and preparing the filter in the crystal with a laser beam propagating at 90° to the UOT signal beam. About 6% of the photons emitted from the light guide reached the detector. This is a factor of ~ 100 improvement compared with the set-up described in Section 4.3.4. The same PMT detector with a quantum efficiency of 1.7%, was used.

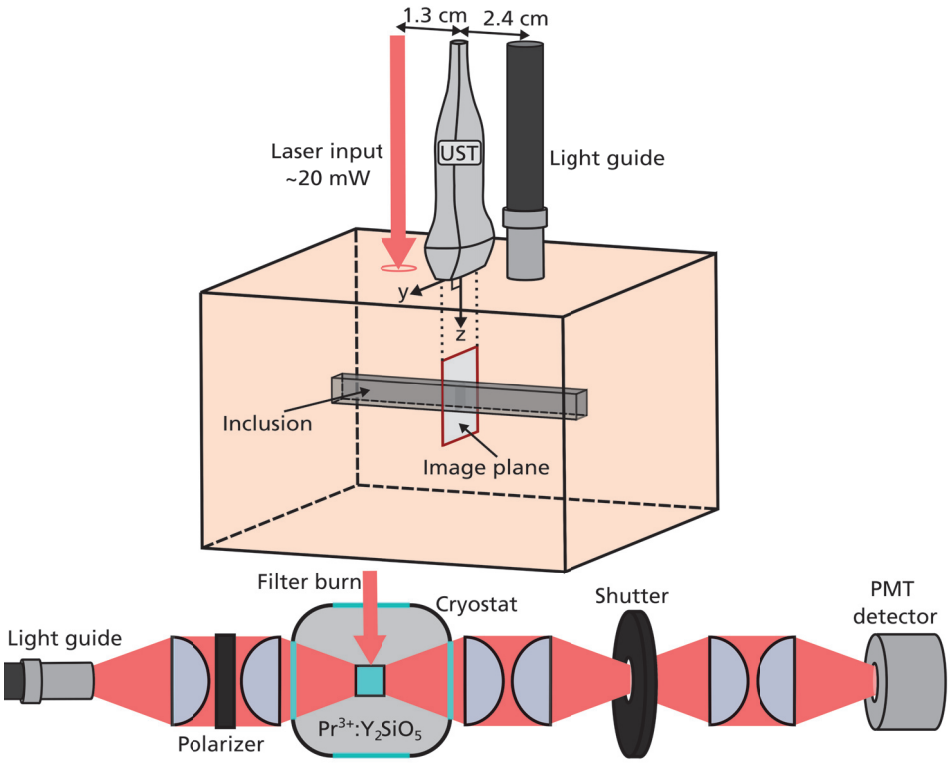

Figure 4.11: Experimental set-up used for UOT studies in reflection mode. UST, ultrasonic transducer.

The spectral filter was prepared using 3900 of the pulses described in Section 4.3.1. The crystal was cooled to a temperature of ~ 5 K. A magnetic field of the order of 10 mT was applied across the crystal to increase the hyperfine lifetimes, and thus the filter lifetime. The filter contrast in this set-up was ~ 25 – 30 dB with 80% transmission within the filter passband.

A linear array ultrasound transducer (Philips L12-3) with an electronically scanning focus was used. This allowed 2D images in the yz-plane (see Figure 4.11) to be scanned point-by-point, by synchronizing the delivery of the optical pulse to different ultrasound pulse locations in the phantom. The optical probe pulses had a peak power of 20 mW, a duration of 1 µs, and an input beam diameter of about 1 mm. The ultrasound and optical pulse repetition rate was 7.4 kHz. Typically, 37×25 image voxels separated by 0.75 mm in both the y and z directions were acquired, after which the filter was refreshed. The ultrasound frequency was 6.0 MHz. The ultrasound pulse volume and peak pressure varied depending on the imaging depth, which is not optimal since it may cause unwanted tagged signal and resolution variations across the image. Future experiments would likely benefit from better control of the ultrasound pulse shape in each image voxel. At an imaging depth of 15 mm, the ultrasound pressure distribution was Gaussian with a peak positive pressure of 3.8 MPa and dimensions of $1.9 \times 2.1 \times 0.75$ mm^3 (FWHM). At an imaging depth of 30 mm, the peak positive pressure was 3.8 MPa. The pressure distribution was Gaussian along y and z with FWHM dimensions of 2.3 mm and 1.1 mm, respectively. The pressure distribution along x (perpendicular to the ultrasound array) had a central part which was Gaussian with a FWHM of 0.7 mm. However, it also had 3.7 mm wide super Gaussian wings with a pressure of about 40% of the peak pressure.

The imaging data presented in this thesis, were obtained using a $9.5 \times 9.5 \times 4.3$ cm^3 phantom with $\mu_a \approx 0.025$ cm^{-1} and $\mu_s' \approx 7.1$ cm^{-1}. An inclusion with the dimensions $5.5 \times 5.5 \times 5.5$ mm^3, and $\mu_a \approx 0.9$ cm^{-1} was added such that it was centred at a depth of 13.5 or 29.5 mm depending on whether the phantom was imaged from the top or bottom.

Imaging results

Figure 4.12 shows data from a 2D scan of the inclusion centred at a depth of 13.5 mm in the phantom. The image was averaged 400 times to improve the CNR. The signal from a single voxel at $z = 4$ mm and $y = 0$ mm is shown in Figure 4.12(a). The slow light delay is about 1.5 µs, which is shorter than that in the set-up discussed in Section 4.3.4. The higher crystal temperature is believed to be the cause of the poorer filter performance. It should be noted that, at an imaging depth of 4 mm, the shortest path from the optical input to the light guide is about 3.8 cm in the reflection geometry used here (see Figure 4.11). The vertical black dotted lines in Figure 4.12(a) indicate the time window used to calculate the signal photons in the other parts of Figure 4.12. Data were also acquired without the ultrasound pulse present in the phantom to estimate and subtract the small background of untagged photons from the data.

The optically absorbing inclusion is seen as a decrease in the number of photons detected in Figure 4.12(b)-(d). However, there are significant signal variations across the image not caused by the inclusion, as the direct path length between the optical input and the light guide via each image voxel is not identical for all voxels. Thus, the signal decreases towards the edges of the image (along y) compared to the centre, and at greater imaging depths, as can be seen in Fig 4.12(c) and Fig 4.12(d), respectively. Methods for the removal of these unwanted signal variations to obtain an image that more accurately represents the true optical absorption of the phantom are desirable.

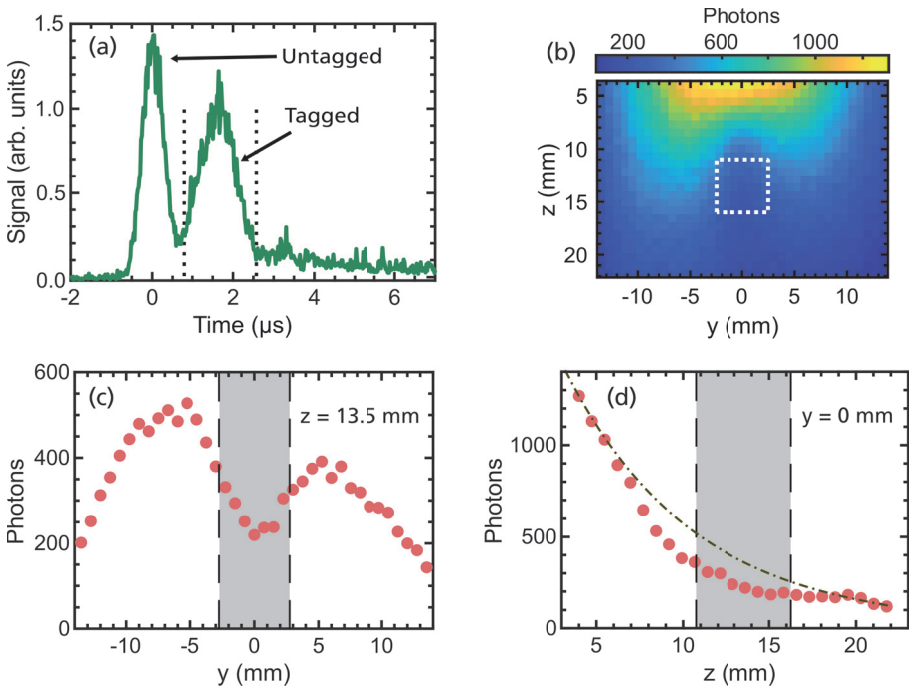

Figure 4.12: UOT measurements on a phantom with $\mu_a \approx 0.025$ cm^{-1} and $\mu_s' \approx 7.1$ cm^{-1}, containing a $55 \times 5.5 \times 5.5$ mm^3 large inclusion with $\mu_a \approx 0.9$ cm^{-1}, centred at a depth of $z = 13.5$ mm. All the data were taken at $x = 0$ mm. The average number of photons incident on the detector per probe pulse is referred to as photons on the figure axes. The data were averaged 400 times. (a) Signal from the voxel located at $y = 0$ mm and $z = 4$ mm. The vertical black dotted lines indicate the time window used to calculate the signal in the other parts of the figure. (b) 2D image, where the position of the inclusion is indicated by the white dashed square. (c) 1D scan along y at a depth of $z = 13.5$ mm (d) 1D scan along z at $y = 0$ mm. The brown dot-dashed line is an exponential function added to guide the eye, and and make it easier to see the decrease in the signal due to the inclusion. In (c) and (d), the position of the inclusion is indicated by the grey shaded area.

One method of removing these signal variations along the y direction is to mechanically move the optical input, light guide, and ultrasound transducer (with a transducer that provides ultrasound pulses along a single line). However, this approach is expected to be more time consuming than an electronically scanning ultrasound focus. Alternatively, the tissue illumination and detection geometries could be optimized to

minimize the problem along the y direction by providing a more even light distribution. For example, Kim et al. have used ring shaped illumination [79]. The model presented in **Papers III & IV**, could be used as a tool to investigate different tissue illumination and detection geometries. It may also be possible to compensate the signal variations along both the y and z directions using theoretical modelling based on the Monte Carlo method or diffusion theory. For example, it is possible to use the models presented in **Papers III & IV**, to calculate the expected UOT image in the absence of the inclusion, and use this to normalize the experimental data. This approach requires knowledge of the optical properties of the background medium, which is available for the phantoms used here. However, the feasibility of such an approach in actual biological tissues, where the background medium is not homogeneous and the optical properties are not know, would have to be investigated. Ultimately, it may be possible to develop UOT image reconstruction models based on solving the inverse problem. This has been investigated by Powell et al. [80], and is currently being investigated by David Hill in our group. A two (or multiple) wavelength imaging approach could also be considered depending on the medical application. It may be possible to normalize the data acquired at one wavelength to the data acquired at another wavelength. Still, knowledge of the scattering coefficients of the tissue at the two wavelengths used in such an approach is desirable.

Figure 4.13 shows a UOT image of the inclusion centred at a depth of 13.5 mm, that has been normalized to simulated data in the absence of the inclusion. The inclusion is much more prominent than in the unprocessed image shown in Fig 4.12(b), and the signal contrast more accurately reflects the true difference in optical absorption in the phantom.

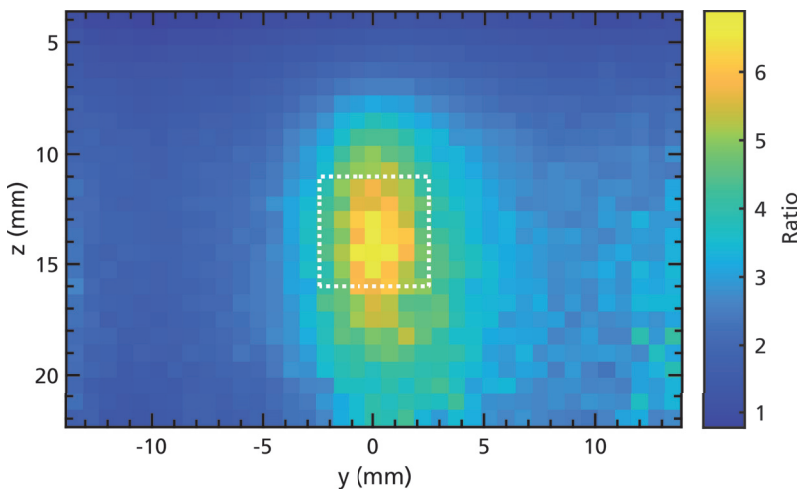

Figure 4.13: The experimental UOT image shown in Figure 4.12(b) normalized to simulated data in the absence of the inclusion. The position of the inclusion is indicated with the white dotted box.

Increasing the tagged signal using reflecting films

A simple yet effective means of increasing the UOT signal, is to place reflecting materials on the tissue surface to prevent photons from leaking across the surface. The use of reflecting films for this purpose (3M optical film, American Polarizers) was investigated. Measurements made in the reflection mode set-up shown in Fig 4.11 are presented. It should, however, be noted that measurements made in the transmission geometry (Figure 4.7) gave a similar increase in signal.

The reflecting film was cut into the shape shown in Figure 4.14(a), and placed on the surface of the phantom. Figures 4.14(b) and (c) show measurements from an imaging depth of 29.5 mm with and without the reflecting film. It can be seen that both the tagged and untagged signals are increased by a factor of ~ 3. This demonstrates that reflecting films can be used to increase the UOT signal, and should therefore be considered in the design of future UOT systems.

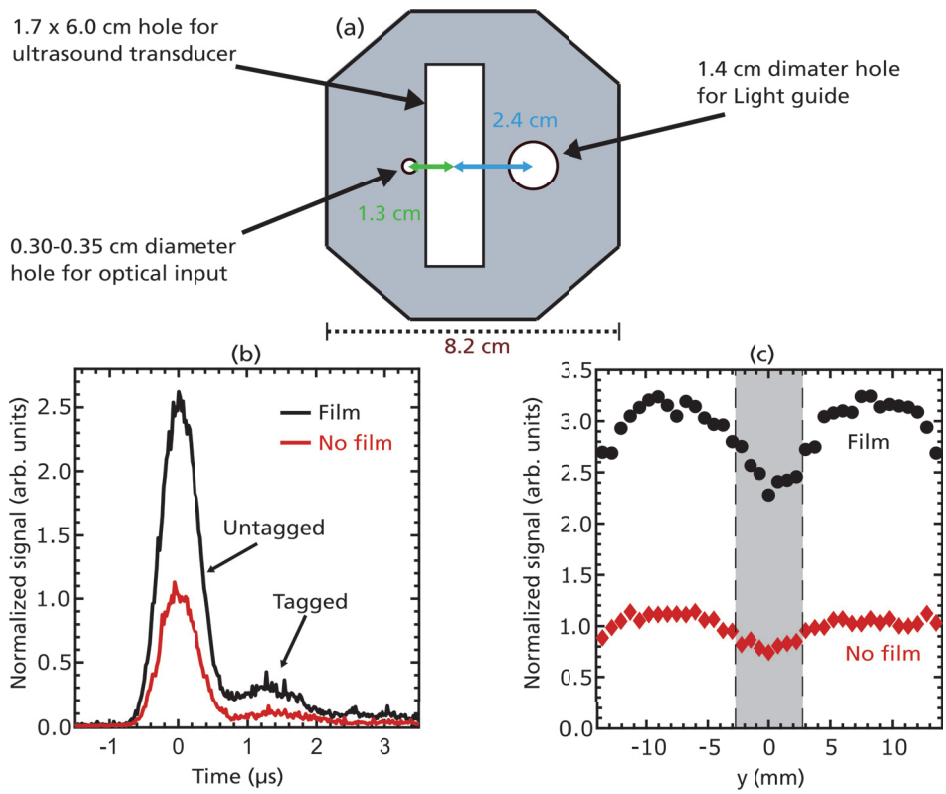

Figure 4.14: Increase in signal strength as a result of using reflecting film. (a) Schematic drawing of the reflecting film used with the set-up depicted in Figure 4.11. (b) Examples of signals obtained with and without reflecting film from a single image voxel at a depth of $z = 29.5$ mm and $y = 8.25$ mm. (c) 1D image of an inclusion at a depth of 29.5 mm. The grey shaded region indicates the position of the inclusion. The data were averaged 400 times.

4.4 Set-up improvements

The UOT set-up could be significantly improved to enable imaging at greater depths and/or faster imaging and/or to improve the ability to measure smaller differences in optical absorption. Suggestions for potential improvements to the system are presented below.

The quantum efficiency of the detector was measured and found to be 1.7% for a beam filling the whole detector area. This is lower than the efficiency specified by the manufacturer, and is believed to be due photocathode degradation due to overexposure. PMT detectors with a specified quantum efficiency of 15% are, however, available. A silicon photomultiplier (also known as multi-pixel photon counter), cooled to reduce the dark count rate, may also be suitable as a detector. The improvement in signal using such a detector should be a factor of ~ 10.

The set-up presented in Section 4.3.5 had a transmission of 6% from the output of the light guide to the detector. The polarizer in the set-up had an unpolarized transmission of 35%. The spectral hole burning materials presented in Chapter 5 should provide good filter contrast, regardless of the input polarization, and the polarizer could simply be removed. Neither the lenses nor the crystal in the current set-up have anti-reflection coatings for 606 nm. Adding anti-reflection coatings should lead to some signal improvement, although the exact amount is unclear. We expect to be able to achieve similar or higher etendue compared with the light guide using a custom design UOT cryostat recently delivered to our department. The available improvement in signal should be a factor of ~ 10.

Optical probe pulses that were 1 µs long with a 20 mW peak power, delivered at a repetition rate of 7.4 kHz were used in UOT imaging experiments presented in this thesis. At this rate, $\sim 5 \times 10^{14}$ photons are delivered per second. If the laser beam is expanded to 1 cm^2, the number of input photons per second can be increased to $\sim 10^{18}$ and still be with the medical safety limit of 300 mW/cm^2 for average radiation at 800 nm [65]. The signal improvement should be a of factor of ~ 2000, but the number of photons could be further increased by increasing the area of the laser beam illuminating the tissue. In the scheme using 1 µs long optical pulses to scan the UOT image point-by-point, 8 W of laser power would be needed to reach the medical limit, assuming a probe repetition rate of 25 kHz and a 1 cm^2 beam area. It should be noted that it is not possible to probe at higher rates as this would result in two ultrasound pulses in the tissue simultaneously. Alternatively, it is possible to use longer laser pulses with lower peak power to follow the ultrasound pulse as it propagates through the tissue, and thus scan a 1D line for each ultrasound pulse. This is commonly done in the UOT experiments presented in the literature. In such a scheme, the laser peak

power required to reach the medical safety limit is lower.

The findings presented here indicate that it should be possible, and straight-forward, to increase the signal by a factor of ~ 200 000 compared with the current UOT imaging measurements, which, combined with the novel high-contrast filter materials presented in Chapter 5, should result in significantly improved imaging capabilities.

4.5 Potential medical applications

Ultrasound optical tomography has currently not demonstrated *in vivo* capabilities in human tissues. Further research is required before it is clear what the performance of a future UOT device could be, and for which applications UOT would add significant value over other existing imaging modalities. In the Quantum Information Group in Lund, we believe that UOT can have several potentially impactful applications, especially when combined with spectral hole burning filters, due to the large projected imaging depths presented in **Paper VI** (Figure 4.4) and **Paper I** (Figure 4.9). In this section, different applications for UOT are discussed speculatively.

4.5.1 Breast tumour imaging

Breast cancer is the most commonly diagnosed cancer worldwide with about 2.3 million new cases in 2020 [81]. Diagnosis and screening is commonly performed using mammography, which uses ionizing X-ray radiation to form images. Functional contrast can be provided by diffuse optical tomography, but with limited spatial resolution [1], or photoacoustic tomography, which provides sub-millimetre spatial resolution at a few centimetre depth [3].

UOT in a transmission geometry should be well suited to breast imaging, and has lower filter contrast requirements compared to a reflection geometry, as previously discussed. The results presented in **Paper I** (see Figure 4.9) indicate that it may be possible to detect acousto-optic signals with an SNR of ~ 20 in ~ 1 ms through ~ 12 cm thick beast tissue using a $4 \times 4 \times 2$ mm^3 sized ultrasound pulse (half pressure). It should thus be possible to measure at any location in the breast, and a 2D image containing 100 voxels could, for example, be measured in ~ 0.1 s. It is unclear what the image spatial resolution would be due to the somewhat peculiar ultrasound pulse shape used (see **Paper I**). However, the resolution would not be as good as for photoacoustic tomography, but better than for diffuse optical tomography. The image spatial resolution could be improved by decreasing the volume of the ultrasound pulse. However, this would decrease the tagged signal strength, and therefore require

longer measurement times to achieve the same signal SNR.

There is a spread in the optical properties of breast tumour tissue reported in the literature. Generally, there seems to be a rather significant change in optical properties between healthy tissue and tumour tissue. For example, Tromberg et al. measured a factor ~ 2 difference in the optical absorption coefficient [82], which should provide a measurable contrast between tumour and no tumour in a UOT image. Grosenick et al. have reported an increase in the reduced scattering of ~ 20% for carcinomas compared to healthy breast tissue [83]. Theoretical calculations similar to those presented in **Paper VI** (Figure 4.4) would be useful to understand the UOT techniques potential to detect breast tumours.

4.5.2 Brain imaging

Human brain imaging is a sought after application, both for diagnosing brain diseases, such as stroke, and to better understand how the brain functions. UOT may be an interesting technique for such applications. However, the skull bone presents a major challenge for ultrasound-based techniques due to its acoustic attenuation (absorption, scattering, and reflection) and waveform distortion. The acoustic attenuation increases with ultrasound frequency and skull bone thickness. The thinnest part is usually the temporal bone with a thickness of ~ 4 mm [84], which thus appears to be a suitable location for delivering ultrasound into the brain. UOT has the advantage compared to ordinary ultrasound imaging that the ultrasound pulse only has to propagate once, and not twice through skull. For UOT methods such as single-shot off-axis holography, lower ultrasound frequencies can be used. Lui et al., for example, used a 1 MHz ultrasound frequency for their UOT measurements through a human skull [8]. Their ultrasound field was distorted, and attenuated to $10-20\%$ in the presence of a $3-5$ mm thick skull. The lowest ultrasound frequency that can be used in a UOT set-up with spectral hole burning filters, depends on the homogeneous linewidth, and other spectroscopic properties of the rare-earth filter material and transition. Filter materials with transition wavelengths within the tissue optical window that support the use of a 1 MHz ultrasound frequency still has to be identified. The spectral filter results presented in Section 5.6.7, however, indicate that a high-contrast filter for an ultrasound frequency of $\sim 2-3$ MHz may be possible. To better understand the spectral hole burning method's usefulness for human brain imaging, experimental studies of how to optimally focus ultrasound in this frequency range through the skull are of interest.

Chapter 5

Spectral hole burning materials for biomedical applications

So far, UOT experiments have been performed using Pr^{3+}:Y_2SiO_5 [9] and Tm^{3+}:YAG filters [27–29, 85]. The Pr^{3+}:Y_2SiO_5 filters used in the studies presented in Chapter 4 provide ~ 30 dB tagged/untagged contrast, but are less suitable for practical applications due to the high optical attenuation by biological tissues at the 606 nm operating wavelength. Tm^{3+}:YAG filters have demonstrated 14 dB filter contrast [27]. The transition wavelength of 793 nm is close to the isosbestic point of Hb and HbO_2, and could therefore be suitable for measuring relative blood volume in tissues where haemoglobin is the dominant absorber. Additional filters at wavelengths further away from the isosbestic point are required to measure tissue oxygen saturation. It is also desirable to improve the filter contrasts in order to achieve a better image CNR (see Section 4.2) and ultimately advance the technique towards *in vivo* measurements. This chapter summarizes our investigations of novel spectral hole burning materials for high-contrast UOT filtering at wavelengths suitable for imaging deep inside tissue.

Several rare-earth-ion-doped materials and transitions may be suitable filter candidates. Figure 5.1 shows a so-called Dieke diagram of the available transitions for triply ionized rare-earths in LaF3 within and near the first tissue optical window. The challenge lies in identifying a suitable combination of rare-earth element, and crystal host. Several of the transitions shown in Figure 5.1 may be considered. The transitions shaded green could be interesting for UOT filtering, since the energy gap to the lower-lying level is sufficiently large for phonon relaxation rates to potentially be suppressed in a low-maximum-phonon-energy host. The grey transitions will almost certainly be limited by rapid phonon relaxation, and are thus not suitable for UOT filtering. These 12 potential transitions, and a large number of crystal hosts, together

offer many potential combinations.

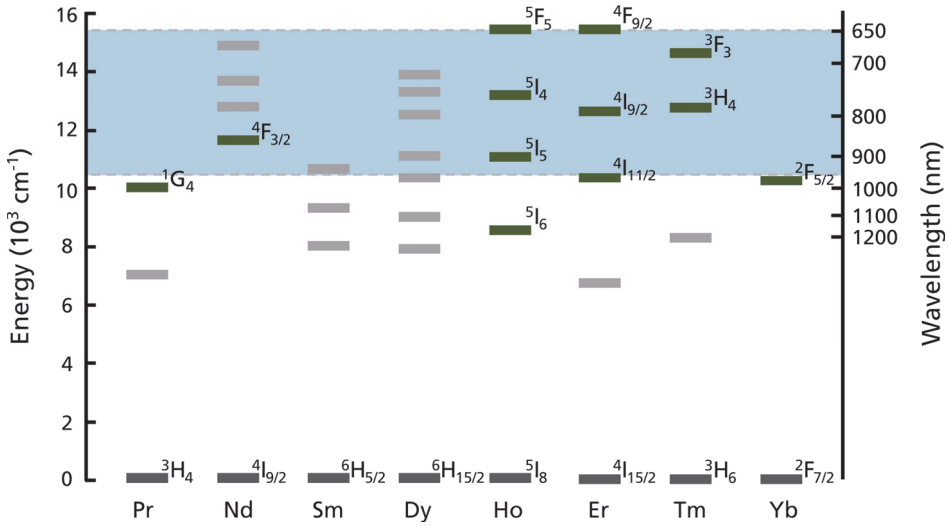

Figure 5.1: Dieke diagram showing the approximate wavelengths of available transitions for triply ionized rare-earth elements in LaF_3 within and near the first tissue optical window ($650-950$ nm). The transition wavelengths vary slightly with the host material. Europium, cerium, gadolinium, and terbium have no transitions within the optical window and are therefore not included in the figure. Promethium is radioactive and is therefore also omitted. The figure was generated using data from Carnall et al. [86, 87].

5.1 Filter material requirements

Apart from a transition wavelength within the tissue optical window, a rare-earth material for UOT filtering must fulfil several other requirements, as illustrated in Figure 5.2(a). Since the tagged and untagged photons are close in frequency (a few MHz), it must be possible to burn ~ 1 MHz bandwidth spectral filters in the inhomogeneous absorption profile of the material. The filter should ideally have minimal attenuation of tagged photons inside the passband, while maximally attenuating the untagged photons outside the passband, and a steep frequency roll-off.

The homogeneous linewidth Γ_h affects the filter frequency bandwidth and roll-off, and attenuation of tagged photons in the passband. The homogeneous linewidth of the dopant ions must be significantly less than the desired spectral width of the filter. Materials with $\Gamma_h \sim 100$ kHz or less are thus primarily of interest for UOT filters.

The peak optical absorption coefficient must be sufficiently high to achieve the desired attenuation outside the filter passband. For example, it can be calculated that an absorption coefficient of 7 cm^{-1} is required to obtain 60 dB attenuation with a 2 cm long crystal. Therefore, materials with an absorption coefficient > 7 cm^{-1} are pri-

marily of interest. However, longer crystals could be considered for materials with a lower absorption coefficient. Light will be guided through the crystal via total internal reflection.

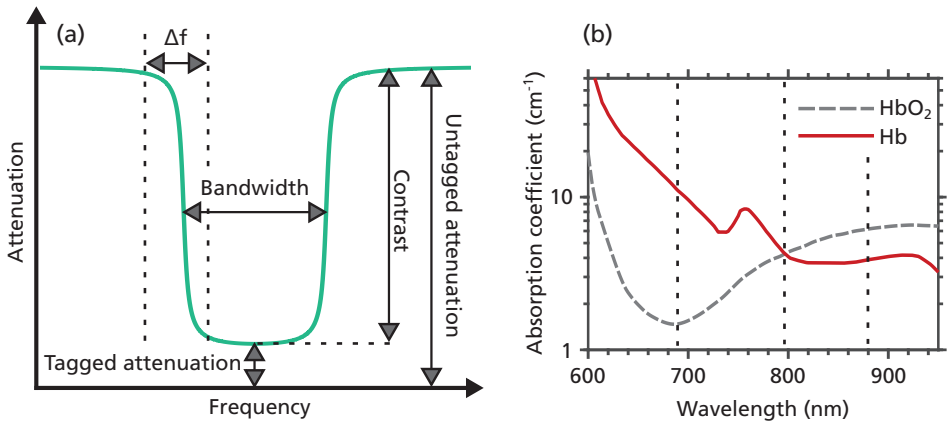

Figure 5.2: (a) A UOT filter material must be capable of supporting ~ 1 MHz bandwidth filters with a sharp roll-off, i.e. narrow Δf, low tagged attenuation and high untagged attenuation. (b) Absorption coefficients for Hb and HbO_2. The dashed vertical lines show the approximate filter wavelengths of thulium- and neodymium-doped materials.

The lifetime of the spectral hole is important, since it determines how often the filter must be refreshed. Generally, materials with spectral hole lifetimes of several seconds or more were considered. However, the ratio between the filter preparation time and the available UOT measurement time before the filter needs to be refreshed is the more relevant figure of merit. If this ratio is < 1, most of the time can be allocated to acquiring the UOT image, and the CNR will not be significantly degraded. Materials with filter preparation times shorter than the filter lifetime are thus desirable.

To highlight the effect of population decay on the filter transmission, we can consider a UOT filter that is burnt at a frequency where the absorption coefficients before and immediately after burning are α_B and zero, respectively. The absorption coefficient recovers with a single time constant τ. The absorption coefficient at the filter frequency as a function of time $\alpha_{pass}(t)$ is then described by:

$$\alpha_{pass}(t) = \alpha_B(1 - e^{-t/\tau}) \tag{5.1}$$

The transmission in the filter passband T_{pass} for a certain filter crystal length L_c can be expressed:

$$T_{pass} = e^{-\alpha_{pass}(t)L_c} \tag{5.2}$$

Figure 5.3 shows the transmission over time through a 1 cm long filter crystal with an absorption coefficient of $\alpha_B = 15\ cm^{-1}$ for time constants, τ, of 10 s and 100 s. It is

clear from this figure that the filter transmission degrades to a point where the filter must be refreshed on time scales shorter than the lifetime of the metastable states that store the population that make up the spectral filter.

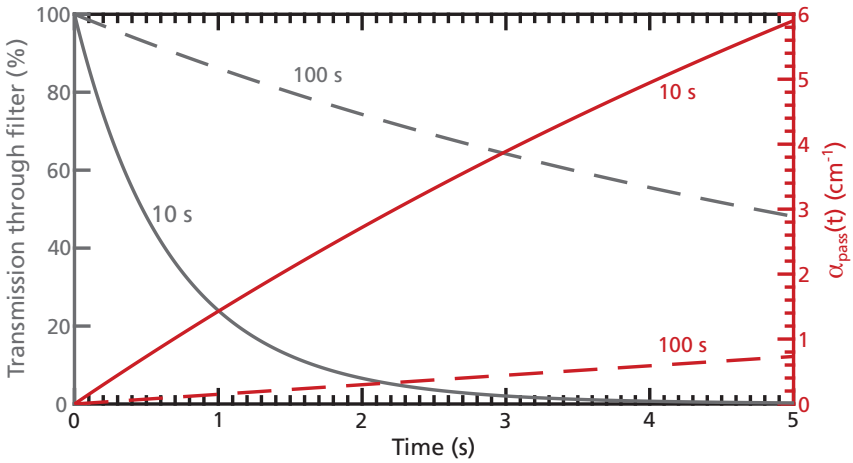

Figure 5.3: Decay of transmission and recovery of $\alpha_{\text{pass}}(t)$ at the filter centre frequency for $\tau = 10$ s and $\tau = 100$ s. It was assumed that $\alpha_{\text{B}} = 15$ cm^{-1} before burning, and zero immediately after burning, and $L_{\text{c}} = 1$ cm.

Figure 5.3 also shows that a large fraction of the population at the filter burn frequency must be transferred to a storage state, otherwise the filter transmission will be low. In other words, it must be possible to burn deep spectral holes in the materials. If ~ 5% of the population remains in the passband, the transmission will be ~ 50% in the above example. Long-lived spectral holes do not necessarily mean that it is possible to burn deep holes. With each excitation of an ion, there might be a rather small probability that it will decay to the storage state. The excitation process must then be repeated several times before the ion is successfully transferred to the storage state. The branching ratio into the storage states is thus important.

Several important spectroscopic properties must therefore be characterized in order to determine whether a rare-earth-ion-doped material is suitable for UOT. The spectroscopic properties of a few thulium- and neodymium-doped materials presented in the literature are presented below. Thulium-doped into lanthanum trifluoride (LaF_3) appears to fulfil the above discussed requirements, and the experimental characterization of this material is also described.

5.2 Neodymium-doped materials

Neodymium-doped materials have four transitions within the tissue optical window, see Figure 5.1. However, only the $^4I_{9/2}$-$^4F_{3/2}$ transition at ~880 nm has shown interesting properties. The other transitions likely have broad homogeneous linewidths due to a short excited state lifetime caused by rapid phonon relaxation to the lower lying levels. The ~880 nm transition provides sensitivity to tissue oxygenation as shown in Figure 5.2(b). A decrease in oxygenation results in a decrease in the absorption coefficient (for a fixed blood volume).

Neodymium has an odd number of electrons, and therefore has half-integer electron spin. Each crystal field level is at least doubly degenerate. The levels can be split by applying an external magnetic field, which allows spectral holes to be burnt into these electronic Zeeman levels. There are several naturally occurring isotopes of neodymium, 80% without nuclear spin, and 20% with nuclear spin ($I = 7/2$) [88]. The isotopes with nuclear spin possess hyperfine structure, and thus additional shelving states for spectral hole burning applications.

Based on the spectroscopic data available on neodymium-doped crystals in the literature, neodymium-doped yttrium orthovanadate, Nd^{3+}:YVO_4, appears to be an interesting candidate for UOT. The material has a high peak absorption coefficient of ~ 40 cm^{-1} [89]. Homogeneous linewidths of ~ 10 kHz have been measured at 1.5 K for a magnetic field of ~ 1000 mT [90]. Deep spectral holes have been burnt resulting from population storage in the electronic Zeeman levels at 2.8 K with a magnetic field of 300 mT. However, these spectral holes contained a decay component of 18 ms [91]. Due to this short lifetime, the present work was instead focused on thulium-doped materials. However, Liang et al. recently showed that spectral holes with a decay component of ~ 200 ms could be burnt in an isotopically pure $^{142}Nd^{3+}$:YVO_4 crystal cooled to 1.5 K [92]. Spectral hole lifetimes could potentially be further increased by doping with $^{143}Nd^{3+}$ or $^{145}Nd^{3+}$, which are the neodymium isotopes with nuclear spin, as spectral holes could be burnt into the hyperfine levels. This has been shown for Nd^{3+}:Y_2SiO_5 [93], and could also be investigated for isotopically pure Nd^{3+}:YVO_4, to enable the use of the material in UOT.

5.3 Thulium-doped materials

Figure 5.4 shows the relevant energy structure for the thulium system. The $^3H_6$-$^3F_3$ and $^3H_6$-$^3H_4$ transitions have wavelengths within the tissue optical window at around 690 and 790 nm, respectively. As mentioned above, the 790 nm transition is close to the isosbestic point of Hb and HbO_2. The 690 nm transition provides

good sensitivity to tissue oxygenation, as can be seen in Figure 5.2(b). The tissue absorption coefficient at 690 nm increases as the oxygenation decreases (for a fixed blood volume). The thulium wavelength pair could potentially be used to achieve an oxygenation-sensitive UOT system, possibly in combination with the neodymium transition at 880 nm. The $^3H_5$ level is conventionally known to be relatively short-lived and is thus not included in the subsequent discussion. The $^3F_4$ level is often called the bottleneck level, and commonly has lifetimes of ~ 10 ms.

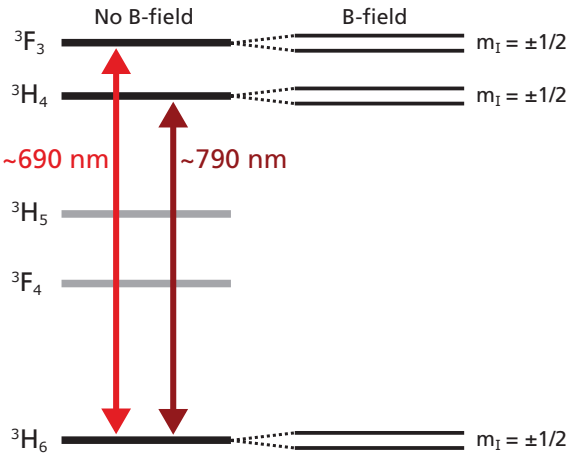

Figure 5.4: Approximate energy level structure of a Thulium-doped crystal. The figure only shows the lowest energy crystal field level in each electronic state.

There is only one naturally occurring isotope of thulium with nuclear spin $I = 1/2$. In the absence of a magnetic field, the two nuclear states are degenerate, and there is no hyperfine structure. However, applying a magnetic field splits each level into two spin states ($m_I = \pm 1/2$) via the enhanced nuclear Zeeman interaction [94–96]. It should be noted that this splitting is generally different for the different levels, although they are illustrated as being identical in Figure 5.4. This allows the burning of spectral holes due to population storage in the nuclear states. The lifetime of the nuclear states are dependent on temperature and magnetic field strength/direction. The selection rule $\Delta m_I = 0$ is relaxed to various degree in thulium-doped materials and strongly depend on the magnetic field direction due to different spin-state mixing [97].

5.3.1 The $^3H_6$-$^3H_4$ transition

The low-temperature spectroscopic properties of the $^3H_6$-$^3H_4$ transition of Tm^{3+} have been presented in the literature for a wide range of host materials. Several of these hosts exhibit properties indicating that they may be suitable candidates for UOT applications. The $^3H_6$-$^3H_4$ transition in Tm^{3+}:YAG has already been used for UOT

with a filter contrast of ~ 14 dB [27]. It is therefore interesting to investigate this transitions further, to better understand its potential for filtering applications. YAG, $LiNbO_3$, and Y_2SiO_5 hosts are discussed in the remainder of this subsection based on the spectroscopic data available in the literature. Spectroscopic data from measurements by our group on the LaF_3 host are presented mainly in Section 5.6.

Tm^{3+}:YAG

Tm^{3+}:YAG is one of the more well studied rare-earth materials at cryogenic temperatures, and has also been considered for other applications within quantum information science [98] and radio frequency signal analysis [26]. A homogeneous linewidth of 3 kHz has been measured in 0.17%Tm^{3+}:YAG at 1.5 K with a magnetic field of 43.8 mT [99], and Laudereau reported a linewidth of 44 kHz at 3 K for a doping concentration of 2% [100]. This is an acceptable linewidth for application in UOT. The absorption coefficient is 27 cm^{-1} for a doping concentration of 2% [28]. Spectral hole lifetimes longer than 100 s are possible [95]. However, based on the results of previous UOT experiments using Tm^{3+}:YAG, it appears that burning deep filters with high transmission in the passband in a centimetre-sized crystal with a doping concentration of 2% is challenging [29].

Tm^{3+}:Y_2SiO_5

Spectroscopic studies of thulium-doped Y_2SiO_5 have been presented by Venet et al. [96], and by Equall [101]. Rare-earth-ions replace yttrium in the crystal lattice in two different sites of $C1$ symmetry. The Y_2SiO_5 host is frequently used doped with Eu^{3+}, Er^{3+}, or Pr^{3+}, but is not optimal for Tm^{3+} to obtain narrow homogeneous linewidths due to the small energy gap to the nearest crystal field level of $^3H_6$. The linewidths for sites 1 and 2 are 66 and 241 kHz, respectively. This limits the usefulness of Tm^{3+}:Y_2SiO_5 for applications in quantum information science, but the linewidth of site 1 is sufficiently narrow for UOT. The absorption coefficient for a doping concentration of 0.1% is 11 cm^{-1} along the D_2 axis, but a factor ~ 10 lower along D_1. Venet et al. reported that it was possible to burn deep spectral holes, and spectral hole lifetimes of 1.6 s were measured with a 6.6 mT magnetic field. The results presented by both Venet et al. and Equall, thus demonstrate that Tm^{3+}:Y_2SiO_5 is a promising material for UOT filtering.

Tm^{3+}:$LiNbO_3$

Measurements on Tm^{3+}-doped congruent $LiNbO_3$ have been presented by Thiel et al. [102, 103]. The homogeneous linewidth was reported to be ~ 10 kHz at 1.5 K with a magnetic field of ~ 35 mT, and 65 kHz at 3 K in zero magnetic field, which is expected to be sufficiently narrow for UOT. The absorption coefficient was 15 cm^{-1} with a dopant concentration of 0.1%, which is high for materials doped with this concentration of Tm^{3+}. Spectral hole lifetimes were found to be ~ 45 s at 1.7 K for a magnetic field of ~ 35 mT along the crystal *c*-axis. The spectral hole depth achievable is somewhat unclear, and this requires further investigation. Tm^{3+}-doped stoichiometric $LiNbO_3$ has also been suggested to potentially have further improved properties by C. W. Thiel at Montana State University, USA (in personal communication). However, no experimental data are currently available. In our opinion, Tm^{3+}:$LiNbO_3$ is an interesting candidate for a UOT filter material, and we plan to perform spectroscopic measurements on this material in the near future.

5.3.2 The $^3H_6$-$^3F_3$ transition

The T_1 lifetime of the $^3F_3$ level in most Tm^{3+}-doped materials is expected to be short due to non-radiative decay caused by multi-phonon relaxation to the lower-lying $^3H_4$ manifold, as described in Section 3.5. Commonly used host materials such as Y_2SiO_5 and YAG have rather high maximum phonon energies, leading to expected $^3F_3$ lifetimes of the order of 100 ns or less. This implies T_1-limited homogeneous linewidths > 1 MHz, which is not feasible for UOT filters.

To the best of the author's knowledge, the only spectroscopic measurements on the $^3H_6$-$^3F_3$ transition relevant for applications in UOT have been performed by Macfarlane and Dejneka [104]. The results of their spectral hole burning studies indicated that the homogeneous linewidth of the $^3H_6$-$^3F_3$ transition in 0.02% Tm^{3+}:LaF_3 is much smaller than 1 MHz at 1.5 K, which is interesting and warrants further studies.

5.4 Rare-earth spectroscopy set-up

The typical experimental set-up used for spectroscopic measurements on thulium-doped crystals in the present work is shown in Figure 5.5. However, different cryostats, lasers, and detectors, etc., were used. A laser with a narrow linewidth (< 100 kHz) was used to provide light at the desired wavelength. The absolute laser frequency was recorded using a wavemeter. A Faby-Perot interferometer was used to calibrate wider (~ 10 – 100 GHz) frequency scans. An acousto-optic modulator (AOM) was used for

pulse shaping. A reference detector recorded the light before the crystal. Polarization optics and lenses were used to set the desired polarization and laser beam size at the crystal, which was mounted inside a cryostat. A magnetic field of up to 1 T could be applied across the crystal. A gating AOM was used after the cryostat to suppress excitation pulses when necessary, to avoid saturating the transmission detector, which detects the light transmitted through the crystal.

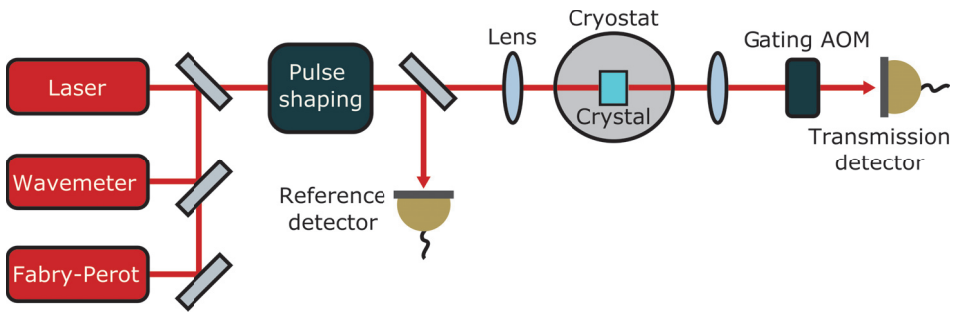

Figure 5.5: General experimental set-up used for spectroscopic measurements on Tm^{3+}-doped crystals.

5.5 The $^3H_6$-$^3F_3$ transition of thulium in low phonon energy hosts

Paper V presents measurements on five different thulium-doped materials, carried out in collaboration with the Cone and Thiel group at Montana State University, USA. Fluorides and alkali lead halides were chosen as the crystal hosts for this study due to their relatively low maximum phonon energies, which should translate into lower phonon relaxation rates, and thus potentially increased $^3F_3$ lifetimes and narrower spectral holes. Table 5.1 summarizes the results.

Table 5.1: Results of spectroscopic measurements on the $^3H_6$-$^3F_3$ transition of Tm^{3+} in crystals with low maximum phonon energy. There are two sites in Tm^{3+}:CaF_2 with C_{3V} and C_{4V} symmetry [105].

Material	Wavelength	Hole width	T_1 lifetime
Tm^{3+}:KPb_2Br_5	698.637 nm	~ 20 MHz	99.9 µs
Tm^{3+}:LaF_3	689.556 nm	380 kHz	1.31 µs
Tm^{3+}:BaY_2F_8	688.78 nm	10.9 MHz	0.69 µs
Tm^{3+}:$YLiF_4$	685.07 nm	8.4 MHz	-
Tm^{3+}:CaF_2 C_{3V}	694.502 nm	-	1.30 µs
Tm^{3+}:CaF_2 C_{4V}	682.156 nm	25.9 MHz	0.61 µs

Spectral hole widths of ~ 10 MHz were observed in Tm^{3+}:BaY_2F_8, Tm^{3+}:$YLiF_4$ and

Tm^{3+}:CaF_2 (C_{4V} site), indicating that these materials are unsuitable for UOT filtering. Hole burning spectroscopy on Tm^{3+}:CaF_2 (C_{3V} site) was prevented by laser tunability problems, and the fluorescence signal was to weak to measure the T_1 lifetime in Tm^{3+}:$YLiF_4$. A laser with a much broader linewidth had to be used to reach the transition wavelength in Tm^{3+}:KPb_2Br_5. The ~20 MHz hole width measured in this material was limited by the laser linewidth. However, the long T_1 lifetime in Tm^{3+}:KPb_2Br_5, suggests that it may be possible to significantly decrease the hole width by narrowing the laser linewidth. The burning of 380 kHz wide holes was possible in Tm^{3+}:LaF_3, indicating that the material is a potential candidate for UOT filtering, and motivating further spectroscopic studies.

5.6 Thulium-doped LaF_3

Lanthanum trifluoride can be described as a trigonal unit cell with lattice parameters $a = 0.72$ nm and $c = 0.74$ nm, and exhibits three-fold ($C3$) rotation symmetry about the crystal c-axis [106, 107]. LaF_3 is uniaxial with the optical axis coinciding with the c-axis, and the refractive index in the visible and near-infrared wavelength regions is about 1.6. Rare-earth dopants replace lanthanum in sites of two-fold $C2$ symmetry. In total, there are three magnetically non-equivalent sites. Figure 5.6 illustrates how the Tm^{3+}:LaF_3 samples were oriented in the spectroscopic measurements presented in this work, i.e., the c-axis and one of the $C2$ axes were both aligned with sides of the cuboid samples. The samples had Tm^{3+} doping concentrations of about 0.1%, 0.5%, and 1%.

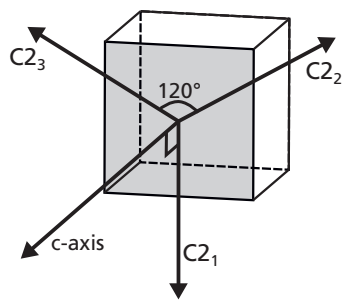

Figure 5.6: Orientation of the Tm^{3+}:LaF_3 samples on which spectroscopic investigations were performed. The crystal c-axis and one of the $C2$ axes were aligned with sides of the cuboid cut samples.

5.6.1 Crystal field level structure

Knowledge of the energy of the lowest-to-lowest transition is generally sufficient for UOT, and the energy of the other crystal field levels may be considered less important. From an atomic physics perspective it may, however, be useful to know the splitting to nearby crystal field levels, since this can help improve our understanding of the mechanisms that limit the homogeneous linewidth and spectral hole lifetimes. The energy level structure of Tm^{3+}:LaF_3 at liquid helium temperature was measured by Carnall et al. already in 1970 [108]. **Paper V** presents both absorption spectra around 685 – 690 nm and the fluorescence spectrum from $^3H_4$ used to obtain the crystal field structures of the $^3F_3$ and $^3H_6$ levels, respectively. Because thulium ions occupy sites of low symmetry in LaF_3, $2J+1$ spectral lines should be observed in the absorption spectra, corresponding to transitions from the lowest energy crystal field level of $^3H_6$ to each of the $2J+1$ crystal field levels in the $^3F_3$ Stark manifold. However, only 6 lines were observed in the present work. The energies measured in this work and by Carnall et al. [108] are summarized in Table 5.2.

Table 5.2: Observed energy structure of the $^3H_6$, $^3H_4$, and $^3F_3$ levels measured in this work (**Paper V**) and by Carnall et al. [108].

Level	This work (cm^{-1})	Carnall et al. [108] (cm^{-1})
$^3H_6$	0	0
	69.3	67
	95.0	-
	124.1	118
	136.4	-
	159	-
	185	-
	207	-
	228	-
	241	-
	274	-
	343	-
	373	-
$^3H_4$	12 554.6	12 561
$^3F_3$	14 502.1	14 508
	14 533.7	14 539
	14 548.0	14 554
	14 549.2	14 569
	14 582.9	14 588
	14 591.0	14 596

5.6.2 Inhomogeneous optical absorption

The $^3H_6$-$^3F_3$ and $^3H_6$-$^3H_4$ transitions have wavelengths of 689.556 and 796.521 nm, respectively. These transitions are strongly polarized perpendicular to the crystal *c*-axis. The absorption coefficient of light propagating along the *c*-axis, is therefore the same regardless of input polarization, which is beneficial when filtering depolarized light, as in UOT.

The inhomogeneous absorption of the $^3H_6$-$^3F_3$ transition was obtained by measuring the optical transmittance through the crystal while frequency scanning the laser around the transition wavelength, and converting it to the absorption coefficient using the Beer-Lambert law. A peak absorption coefficient of 15.2 cm^{-1} was measured for the sample containing 0.5% Tm^{3+}, as shown in Figure 5.7(a). This is sufficient for UOT, since a 1.2 cm long crystal (which is a reasonable size to grow, see Ref. [109] and Section 5.6.7), should theoretically provide ~ 80 dB optical attenuation.

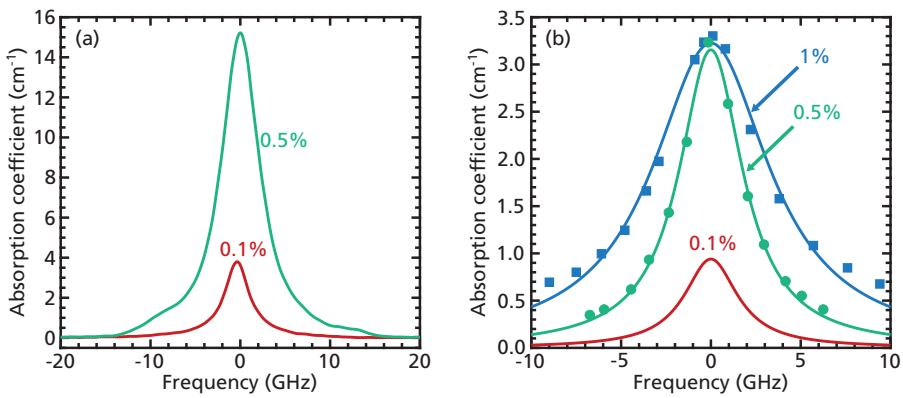

Figure 5.7: (a) Inhomogeneous absorption profile of the $^3H_6$-$^3F_3$ transition and (b) inhomogeneous absorption profile of the $^3H_6$-$^3H_4$ transition. The solid blue and green lines in (b) are Lorentzian fits to the data (symbols). The inhomogeneous absorption profile for the $^3H_6$-$^3H_4$ transition in 0.1% Tm^{3+}:LaF_3 (red line) was plotted based on the peak absorption coefficient and linewidth given by Macfarlane [107].

The $^3H_6$-$^3H_4$ transition, however, had a significantly lower peak absorption coefficient of 3.2 cm^{-1} for a doping concentration of 0.5%, as can be seen in Figure 5.7(b). The data were collected using the optical nutation technique described, for example, by Vega et al. [110], where the initial and final transmission of a single-frequency, constant-intensity laser pulse are compared to calculate the absorption coefficient. Increasing the doping concentration from 0.5% to 1.0% unfortunately only doubled the inhomogeneous linewidth without increasing the peak absorption coefficient. To achieve ~ 80 dB attenuation, a 5.8 cm long crystal would be required. As mentioned above, long crystals can be used, as light will be guided via total internal reflection. However, based on these results, our group plans to investigate other hosts instead,

for example $LiNbO_3$, where the $^3H_6$-$^3H_4$ peak absorption coefficient is higher.

5.6.3 Optical homogeneous linewidth: Temperature dependence

The homogeneous linewidth can be determined using a technique known as photon echo spectroscopy. Photon echoes are similar to spin echoes in nuclear magnetic resonance. The technique has been well described in the literature, see, for example, [111], and therefore, only a brief description is given here. A short laser pulse creates coherence between the ground and excited states for ions within a narrow bandwidth of the inhomogeneous absorption profile. Initially the ions are in phase, but they dephase due to their different resonance frequencies. At a time τ_{12} after the first pulse, a second short laser pulse is delivered, which reverses the dephasing due to the different resonance frequencies. At a time τ_{12} after the second pulse, the ions rephase, and emit a burst of radiation called a photon echo. The ability of the ions to rephase depends on their T_2 coherence time. The T_2 coherence time can be obtained by measuring the decrease of the intensity of the emitted echo as a function of the time between the excitation pulses τ_{12}. The homogeneous linewidth can be calculated from T_2 using Equation (3.1).

The temperature dependence of the optical homogeneous linewidth of the $^3H_6$-$^3F_3$ transitions in 1%Tm^{3+}:LaF_3 was measured using photon echoes with results presented in Figure 5.8. The data were fitted to a model describing linewidth broadening due to direct phonon transitions to a nearby crystal field level [112–114]:

$$\Gamma = \Gamma_0 + \alpha_c (e^{\frac{\Delta}{kT}} - 1)^{-1} \tag{5.3}$$

where, Γ_0 is the ultimate linewidth at absolute zero temperature, Δ the energy separation to the crystal field level, and α_c the coupling coefficient. The parameters extracted from the fit were $\Delta = 25.5$ cm^{-1}, $\Gamma_0 = 170$ kHz, and $\alpha_c = 0.76$ GHz. The energy separation to the nearest crystal field level in $^3F_3$ is 31.6 cm^{-1} (see Table 5.2). These results thus support that resonant phonon absorption to the adjacent crystal field level in $^3F_3$ contribute mostly to linewidth broadening in the investigated temperature range. No clear change in the homogeneous linewidth was observed when applying a 100 mT magnetic field. Homogeneous linewidths down to 117 kHz (T_1-limited linewidth) were measured in the 0.1%Tm^{3+}:LaF_3 sample (see the thesis by Marsh [41]). Thulium concentration thus appears to affect the linewidth. The results provide useful information on the temperature required to use Tm^{3+}:LaF_3 in UOT. It can be seen from Figure 5.8 that the homogeneous linewidth of the $^3H_6$-$^3F_3$ transition is not significantly decreased at temperatures lower than 3 K, but is rapidly increased at temperatures higher than 3 K. Temperatures of ~ 3 K are achievable with comparatively compact high-etendue commercial close-cycle cryostats.

It must be noted that a day-to-day variation in the homogeneous linewidth measured at a specific temperature of almost 10% was observed in the 1% sample. This is larger than the uncertainty in the homogeneous linewidth obtained from a typical echo decay measurement, and indicates systematic error. In general, the random error is often smaller than the systematic error in many of the spectroscopic measurements presented in this thesis. The error bars due to random error are often of similar size or smaller than the symbols displayed in the plots. An accuracy better than 10% is not necessary when characterizing the spectroscopic properties of a material for UOT.

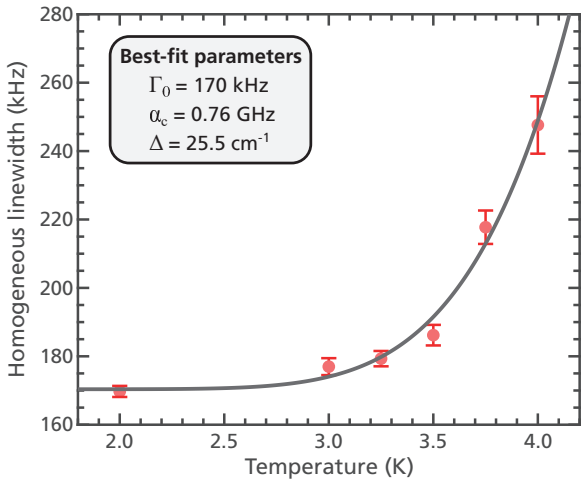

Figure 5.8: Temperature dependence of the homogeneous linewidth of the $^3H_6$-$^3F_3$ transitions in 1%Tm^{3+}:LaF_3 in zero magnetic field. The error bars on the experimental data represents the 95% confidence interval. The solid black line is a fit to Equation (5.3). The best-fit parameters are shown in the insert.

Macfarlane have previously reported a homogeneous linewidth of 45 kHz for the $^3H_6$-$^3H_4$ transition 0.1%Tm^{3+}:LaF_3 at 1.5 K [99]. We measured a homogeneous linewidth of about 65 kHz in 1%Tm^{3+}:LaF_3 at 2.17 K. The linewidth was decreased to ~ 30 kHz when applying magnetic field of 100 mT. In general, the homogeneous linewidth of the $^3H_6$-$^3H_4$ transition is narrow enough for applications in UOT.

5.6.4 Lifetimes of $^3H_4$ and $^3F_4$

If a spectral hole is burnt in the $^3H_6$-$^3F_3$ transition, ions will decay from the $^3F_3$ to the $^3H_4$ level on a timescale of ~ 1 µs. A fraction $(1-\beta)$ of the population will decay from $^3H_4$ to $^3H_6$. The remaining fraction β will branch to $^3F_4$, before subsequently decaying to $^3H_6$. As mentioned above, the $^3H_5$ level is assumed to be very short-lived compared to the $^3H_4$ and $^3F_4$ levels, and is therefore not included in the analysis in

this section.

Time-resolved spectral hole burning measurements are useful for determining population relaxation dynamics. A spectral hole is first burnt, and thereafter probed using frequency scanning laser pulses at different time delays. The area of the spectral hole is proportional to the difference in population between the $^3H_6$ and $^3F_3$ levels, and the lifetimes of the levels involved can therefore be extracted directly from the spectral hole decay. However, since the population of the $^3F_3$ level decays rapidly, this level should not be easily observable in a spectral hole decay. A double exponential decay is therefore expected with time constants corresponding to the $^3H_4$ and $^3F_4$ lifetimes. The expression for the time-dependent hole area can be derived from rate equations as:

$$\frac{\Delta\alpha(t)}{\Delta\alpha(0)} = e^{-\frac{t}{T_A}} + \frac{\beta T_B}{T_B - T_A}\left(e^{-\frac{t}{T_B}} - e^{-\frac{t}{T_A}}\right) \tag{5.4}$$

where T_A and T_B are the lifetimes of $^3H_4$ and $^3F_4$, respectively, $\Delta\alpha(t)$ is the time-dependent hole area, and $\Delta\alpha(0)$ is the initial hole area.

Measurements of a spectral hole decay are shown in Figure 5.9. The expected double exponential decay was observed, and lifetimes of 3.4 ± 0.2 and 15.7 ± 0.5 ms were obtained for the $^3H_4$ and $^3F_4$ levels, respectively, with $\beta = 39 \pm 2\%$. Hong et al. have previously reported a $^3F_4$ fluorescence lifetime of 15.6 ms measured at room temperature [109], which is in good agreement with the present results. Huang et al. reported a $^3H_4$ fluorescence lifetime of 2.1 ms at room temperature [115]; the reason for the discrepancy is not known.

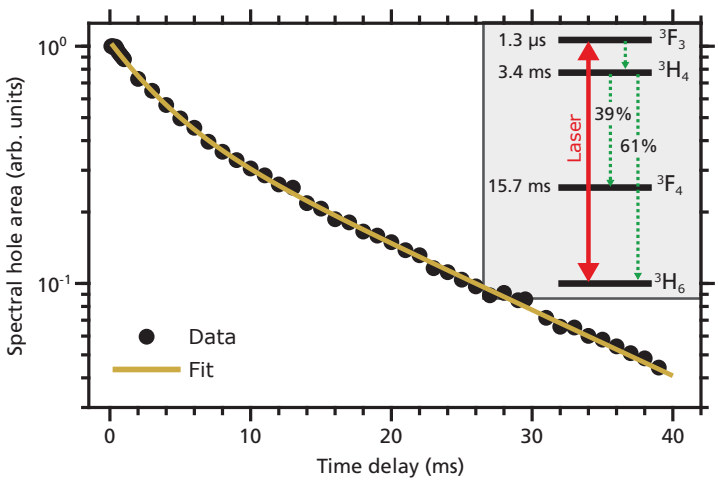

Figure 5.9: Transient spectral hole area decay in 0.1% Tm^{3+}:LaF_3 at a temperature of 4 K. The spectral hole was burnt on the $^3H_6$-$^3F_3$ transition using a 50 µs duration pulse. Frequency scanned pulses were thereafter used to read out the spectral hole at different time delays. The lifetimes of $^3H_4$ and $^3F_4$, and the branching ratio shown in the insert were obtained by fitting the data to Equation (5.4).

5.6.5 Hole burning in a magnetic field: Zeeman splitting

The degeneracy of the nuclear spin states is lifted in the presence of a magnetic field (see Figure 5.4). Spectral holes can then be burnt into the nuclear states. The splitting of the ground and excited states can be deduced from the side hole and antihole structure obtained from spectral hole burning measurements (see Section 3.3). The splitting depends on the magnetic field strength and orientation. For a field applied along the crystal *c*-axis, the sites are magnetically equivalent (see Figure 5.6), and the splitting should be identical for all sites. If the magnetic field is applied along an arbitrary direction, for example, in the plane perpendicular to the *c*-axis, the sites are not magnetically equivalent, and the splitting for the different sites may differ.

Examples of spectral holes burnt in both the $^3H_6$-$^3F_3$ and $^3H_6$-$^3H_4$ transitions with a magnetic field applied along the crystal *c*-axis are shown in Figure 5.10. The laser beam was propagating parallel to the *c*-axis, and the polarization was aligned parallel to one of the *C*2 axes. One side hole pair and three anti-hole pairs are expected in a system with two ground states and two excited states, however, this was not observed in the data. The presence of weak side structure (indicated by the red dashed arrows in Figure 5.10) indicates additional interactions, commonly referred to as superhyperfine interactions [116], meaning that the thulium ion transition also involves the spin-flip of a host nucleus. The fluorine nucleus has a large gyromagnetic ratio of about 40.1 MHz/T [117], and this is expected to be similar, also in the LaF_3 lattice [116]. Indeed, side structure splitting at about 40.1 MHz/T can be observed in the hole burning spectrum in Figure 5.10(b). The other weak structures also contain the ≈ 40 MHz/T component. For example, the difference in frequency between the weak and strong side hole pairs in Figure 5.10(a) is $55.6 - 15.4 = 40.2$ MHz/T.

The stronger side structure is due to the splitting typically expected in thulium systems as illustrated in Figure 5.4. The side holes directly give a splitting of the excited states Δe of 56 MHz/T and 147 MHz/T for the $^3F_3$ and $^3H_4$ levels, respectively. The strong antiholes at 34 MHz/T appear in the spectra for both transitions, and is thus the $^3H_6$ ground state splitting Δg. The antihole pair expected at $\pm(\Delta e + \Delta g)$ to the main hole was not observed in the hole burning spectra. The absence of these antiholes indicate that the transitions where $\Delta m_I = 0$ are stronger compared to the transitions where $\Delta m_I \neq 0$ [97].

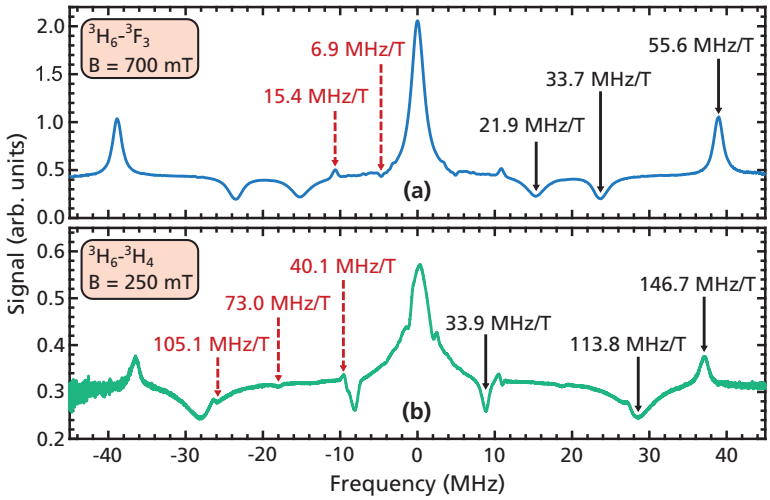

Figure 5.10: Transmission through spectral holes burnt in 1%Tm^{3+}:LaF_3 with a magnetic field along the crystal c-axis for (a) the $^3H_6$-$^3F_3$ transition (b) the $^3H_6$-$^3H_4$ transition.

5.6.6 Hole burning in a magnetic field: Hole lifetimes

The lifetimes of the nuclear states were measured for different magnetic field strengths and orientations by burning spectral holes, and subsequently reading them out using frequency scanning laser pulses at different time delays. As mentioned above, the decay of the spectral hole area gives the population dynamics. The magnetic field was applied either parallel to the crystal c-axis, perpendicular to the c-axis and parallel to one of the $C2$ axes, or perpendicular to both the c-axis and one of the $C2$ axes.

The results are presented in Figure 5.11. A single exponential decay is expected when the magnetic field is applied parallel to the c-axis since the field projections on all the rare-earth sites are equal. However, a double-exponential decay was observed and used to fit the data, and short and long lifetimes are therefore presented in Figure 5.11(a). The lifetimes are ~ 40 s and ~ 250 s for a magnetic field of 1 T. A third weaker decay component with a lifetime of a few seconds was also observed for a magnetic field of 1 T. The reason for the additional decay components is not known and warrants further studies.

For a magnetic field applied perpendicular to the crystal c-axis and either parallel or perpendicular to one of the $C2$ axes, there are two magnetically in-equivalent subsites. The laser beam was propagating perpendicular to the c-axis with the polarization aligned parallel to one of the $C2$ axes in the present experiments. A double-exponential decay is expected, which was also observed in the data. Spectral holes were found to persist of the order of an hour for a magnetic field applied perpendic-

ular to the crystal c-axis as can be seen in Figure 5.11(b) and (c), which should allow for long UOT measurement times after filter preparation.

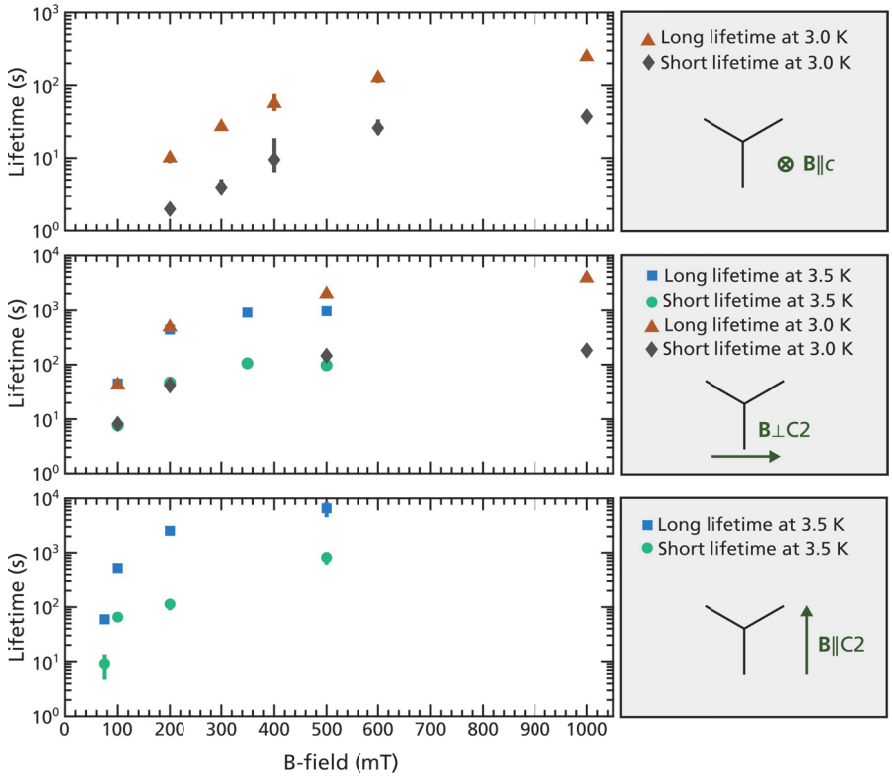

Figure 5.11: Dependence of nuclear spin-state lifetimes on magnetic field. (a) Lifetimes in 1%Tm^{3+}:LaF_3 for a field applied along the c-axis. (b) Lifetimes in 0.5%Tm^{3+}:LaF_3 for a field applied perpendicular to both the c-axis and one of the $C2$ axes. (c) Lifetimes in 0.5%Tm^{3+}:LaF_3 for a field applied perpendicular to the c-axis and parallel to one of the $C2$ axes. The error bars represents the 95% confidence interval from the fits, and are smaller than the symbols for most data points.

5.6.7 High-contrast spectral holes

Based on the 15 cm^{-1} optical absorption coefficient, long spectral hole lifetimes, and 170 kHz linewidth measured for the $^3H_6$-$^3F_3$ transition of Tm^{3+}:LaF_3, the material appears to be a suitable candidate for UOT filtering. However, the ultimate test would be to prepare high-contrast UOT filters of the material. This would require a crystal with a large optical depth, and a $10 \times 10 \times 10$ mm^3 ~ 1% Tm^{3+}:LaF_3 was therefore acquired (from MEGA Materials s.r.l.).

The experimental set-up used for the preparation and characterization of high-contrast spectral holes in 1% Tm^{3+}:LaF_3 is shown in Figure 5.12. The crystal was mounted in-

side the cryostat at 3.0 K, and a 1.0 T magnetic field was applied along the crystal *c*-axis. The crystal had a few internal cracks. To avoid propagating the laser beam through the cracks, an input beam diameter of 2 mm ($1/e^2$) was used. The laser was frequency stabilized to a Fabry-Perot cavity (ORC-Cubic, Menlo Systems) using the Pound-Drever-Hall method. The specified cavity drift and finesse are < 50 kHz/day and ~ 7000, respectively. The laser linewidth when locked to the cavity has not been measured, but is believed to be much narrower than the 170 kHz homogeneous linewidth of the ions on a time scale of ~ 1 s, and should therefore not contribute significantly to the measured spectral hole shapes.

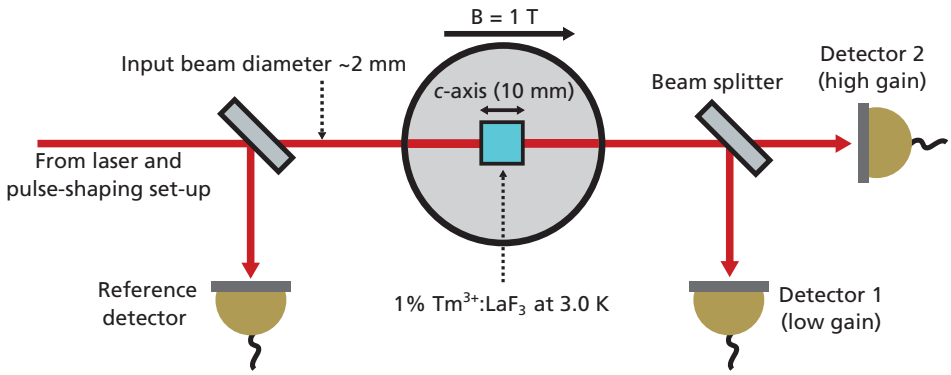

Figure 5.12: Experimental set-up used to prepare and characterize high contrast spectral holes in Tm^{3+}:LaF_3.

Spectral holes were read out using frequency chirped pulses while recording the transmission through the crystal. A set-up with a single transmission detector does not have the dynamic range required to read out high-contrast spectral holes. Therefore, two detectors were used (as shown in Figure 5.12). Detector 1 was used with a low gain to detect light with frequencies around the centre frequency of the spectral hole, but was not able to detect light with frequencies of a few MHz from the spectral hole centre. Detector 2 was used with high gain to detect light with frequencies outside the passband of the spectral hole, but saturated for frequencies near the centre of the spectral hole. The traces obtained from the two detectors were spliced together, and the frequency regions where the signal from detector 1 was in the noise floor, and where detector 2 saturated were discarded. The full transmission was obtained by tuning the laser wavelength a few of nanometre away from the transition, where the ions do not absorb light, and scanning the laser frequency 20 GHz. This allowed the calculation of the optical attenuation due to the crystal.

Two spectral holes prepared at ±5 MHz can be seen in Figure 5.13(a). This is a suitable filter structure for UOT measurements using a ultrasound pulse with a 5 MHz centre frequency. The following laser pulse sequence was used to prepare the spectral holes,

where the frequencies are given relative to the zero frequency in Figure 5.13(a). The laser centre frequency was first shifted by +22 MHz, and 600 pulses were delivered with a 3.0 MHz linear frequency chirp around this centre frequency. The pulse duration was 500 µs, and the power 20 mW. This resulted in an antihole at a frequency of 0 MHz (see Figure 5.10). The spectral holes were thereafter prepared using pulses with a 1.5 MHz linear frequency chirp with a duration of 250 µs, and a power of 5 mW. The laser centre frequency was first shifted by +5 MHz and 200 pulses were delivered. The laser centre frequency was then shifted by −5 MHz and another 200 pulses were delivered. This was repeated a total of three times, i.e., a total of 600 pulses were used to create each spectral hole. There was no temporal separation between any of the pulses, and thus 300 ms was allocated to preparing the antihole at 0 MHz, and 150 ms to preparing each filter. The total duration of the burn pulse sequence was thus 600 ms. Four frequency-chirped pulses were used to read out the spectral holes in Figure 5.13(a). The pulses were scanning from −16 MHz to +1 MHz, +1 MHz to −16 MHz, −1 MHz to +16 MHz, and +16 MHz to −1 MHz, had a duration of 0.75 ms, and were separated by 5 ms. The first read-out pulse was emitted 50 ms after the final burn pulse. This delay is about three time longer than the $^3F_4$ lifetime, and the observed hole is therefore due solely to population storage in the nuclear states.

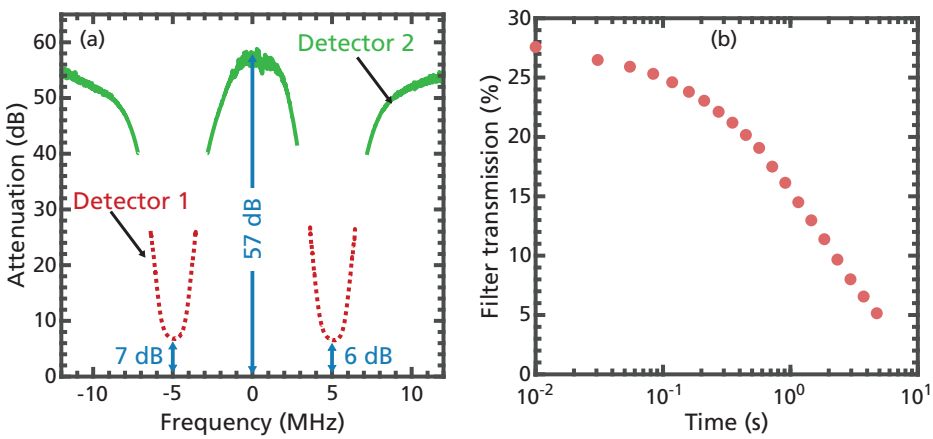

Figure 5.13: (a) High-contrast spectral holes prepared in the $^3H_6$-$^3F_3$ transition of Tm^{3+}:LaF_3 at 690 nm. The red dotted line is the signal from detector 1 (low gain) and the solid green line the signal from detector 2 (high gain). (b) Decay of the spectral hole peak transmission over time when a magnetic field of 1 T was applied along the crystal c-axis. The transmission decayed to half of its initial value in about 1 s. Note that the time scale is logarithmic.

It can be seen from Figure 5.13(a) that the attenuation at the centre frequencies of the two spectral holes was about 6 and 7 dB, respectively, corresponding to a transmission of $\sim 20-25\%$. The attenuation at 0 MHz was about 57 dB. Thus, the filter contrast was about 50 dB, which is a very promising result for UOT filtering using the $^3H_6$-$^3F_3$ transition in Tm^{3+}:LaF_3. The sharp frequency roll-off seen in Figure 5.13(a), indicates

that high contrast filters may be prepared for smaller frequency separations, which are desirable for certain medical applications. For example, the attenuation at 2.5 MHz was about 45 dB. It should be noted that the filtering contrast at 2.5 MHz could potentially be increased by instead optimizing the pulse sequence used to prepare the spectral holes for this particular frequency.

No antihole structure was observed when burning spectral holes near the centre of the inhomogeneous profile, and the attenuation was limited to 57 dB. The presented measurement results are therefore believed to have been limited to an attenuation of 57 dB by light at a frequency outside the inhomogeneous profile, for example, from amplified spontaneous emission from the laser system. Conventional optical filters may mitigate this problem and would have to be investigated. The spectral holes shown in Figure 5.13(a) were prepared at about 3 GHz from the centre of the inhomogeneous absorption profile. In future experiments, it would be interesting to investigate the filter contrast closer to the centre of inhomogeneous absorption profile where the optical depth is greater, as this may improve the attenuation outside the spectral hole.

In future experiments, our group plans to investigate the spectral hole contrast of scattered light. As a first estimate, the attenuation in dB of light incident on the crystal at an angle θ to the crystal c-axis is expected to decrease by a factor $\cos^2(\theta)$. However, this must be confirmed experimentally. It should be noted that θ is the internal angle in the crystal, which is smaller than the incident angle, due to refraction.

The decay of the transmission through the spectral hole was measured by preparing a single high-contrast spectral hole, and using frequency-chirped read-out pulses at different time delays. The results are presented in Figure 5.13(b). The transmission decayed to half its initial value in about 1 s, which can roughly be regarded as the UOT measurement time available before the filter must be refreshed. The decay of the filter transmission is known, and can be compensated for in the UOT data. The initial preparation of the spectral hole requires the removal of a much larger number of ions compared to the case when the filter is refreshed, for example, after decaying for 1 s. After initial filter preparation, a significantly lower number of filter refresh pulses could thus potentially be interleaved with the UOT probe pulses to remove the small fraction of ions that has decayed to fill the spectral hole. In such a scheme, most of the measurement time could thus be allocated to acquiring the UOT signal rather than preparing the filter, but this must be further investigated.

The lifetime of the nuclear states can also be increased by about two orders of magnitude, by instead applying the magnetic field perpendicular to the crystal c-axis (see Section 5.6.6). The filter decay times can therefore be significantly extended compared to the results in Figure 5.13(b), which we plan to investigate in the future. In

the set-up shown in Figure 5.12, it was only possible to apply the magnetic field along the *c*-axis, and no measurements with the magnetic field perpendicular to the *c*-axis could be carried out. Changing the direction of the magnetic field may, however, affect the branching ratio of the levels involved. This could increase or decrease the spectral hole peak transmission, and therefore the spectral hole contrast.

5.7 Conclusions

The spectroscopic investigations presented in this chapter show that the $^3H_6$-$^3F_3$ transition in Tm^{3+}:LaF_3 at 690 nm is a promising candidate for UOT filtering. The peak absorption coefficient was found to be 15.2 cm^{-1} for a thulium doping concentrations of 0.5%, which is sufficient to obtain great optical depths using 1 cm sized crystals. For light propagating along the crystal *c*-axis, the absorption is the same regardless of the input polarization. The de-polarized UOT signal could thus preferably be filtered along this direction. The measured linewidth of ~ 170 kHz shows that spectral holes with the ~ MHz bandwidth required for UOT could be burnt. The spectral hole lifetimes observed in a magnetic field, were longer than the spectral hole preparation times, which should allow most of the UOT image sequence to be allocated to probing the tissue rather than preparing the filter. The 50 dB spectral hole contrast demonstrated in theses studies is a promising first step towards improved UOT based on spectral hole burning filters. Further optimization of the burn sequence, and/or increasing the optical depth of the crystal, and/or changing the orientation of the magnetic field may further improve the contrast.

The $^3H_6$-$^3H_4$ transition in Tm^{3+}:LaF_3 at 797 nm was measured and found to have an peak absorption coefficient of 3.2 cm^{-1} for thulium doping concentrations of 0.5% and 1%. This is somewhat low for UOT applications, and further studies of the $^3H_6$-$^3H_4$ transition in thulium in other host may therefore be of interest.

Chapter 6

Summary and future outlook

The aim of the research presented in this thesis was to further develop the UOT technique using spectral hole burning filters, and investigate its ultimate potential for optical contrast imaging deep inside the human body.

The experimental and theoretical investigations presented in **Papers I, III, & IV**, were all aimed at characterizing and modelling the tagged and untagged components of the UOT signal. The experiments were performed in a set-up with low signal collection efficiency, and a laser power significantly lower than the medical safety limit. However, by matching the measured and calculated signals in tissue phantoms, a better understanding was obtained of the way in which the signal strength depends on various set-up parameters. This allowed predictions of how an optimized UOT set-up could perform in actual tissues. The results suggest that imaging depths of several centimetres should be possible with UOT based on spectral hole burning. The Monte-Carlo-based model presented in **Papers III & IV** can be used to simulate the UOT signal from first principles, and showed good agreement with experimental measurements. Although the model must be further validated for a larger parameter space, this is a promising step towards a virtual lab for UOT. Our group plans to use/develop this model to simulate UOT imaging for specific medical applications, such as human breast and brain imaging, and to improve UOT image reconstruction.

The contrast-to-noise ratios of the many different methods of detecting the UOT signal presented in the literature were compared (**Paper VI**). The results suggest that greater imaging depths can be achieved with the spectral hole burning method than with other methods such as single-shot off-axis holography, speckle contrast, and photorefractive detection. It was thus concluded that the spectral hole burning method has considerable potential for UOT at greater depths. However, the filter contrast

achieved in UOT experiments at wavelength suitable for biomedical applications ($\sim 650-950$ nm) is 14 dB, which is considerably lower than the 30 and 80 dB contrast used in the calculations presented in **Paper VI**.

The experiments presented in **Paper V** were therefore aimed at identifying novel spectral hole burning materials for UOT at wavelengths in the $\sim 650-950$ nm range with improved filter contrast. This study focused particularly on the $^3H_6$-$^3F_3$ transition in thulium-doped crystal hosts. The results showed that by choosing hosts with a low maximum photon energy, spectral hole burning could be enabled on transitions that conventionally exhibit poor hole burning properties. Tm^{3+}:LaF_3 was also identified as an interesting candidate for UOT.

Further spectroscopic studies were also presented on the $^3H_6$-$^3F_3$ and $^3H_6$-$^3H_4$ transitions in Tm^{3+}:LaF_3, at 690 and 797 nm, respectively. Spectral holes in the $^3H_6$-$^3F_3$ transition were shown to have a contrast of 50 dB for a collimated laser beam, which is an encouraging result for future UOT based on spectral hole burning. Further studies should be carried out to investigate the filter contrast for scattered light. The filter contrast may, for example, be further improved by optimizing the filter burn sequence and/or the magnetic field direction, and/or by using crystals with greater optical depth.

The comparatively low absorption coefficient measured for the $^3H_6$-$^3H_4$ transition in Tm^{3+}:LaF_3 showed that it is less suitable for UOT. Future spectroscopic studies of thulium in other host are therefore planned, in particular, thulium-doped stoichiometric $LiNbO_3$.

The findings presented here indicate that UOT based on spectral hole burning may become a useful imaging modality in medicine. It will be interesting to further investigate and develop Tm^{3+}:LaF_3 so that it can be used in *in vivo* applications. This novel filter material also has the added benefit of being compatible with the Ti:shappire laser system at our department in Lund, which provides more than an order of magnitude more laser probe power compared with the system used for UOT at 606 nm. I believe that this system, combined with the recently acquired custom-designed UOT cryostat, and a detector with higher quantum efficiency, will provide interesting results in the years to come.

Appendix A

System design

This appendix briefly describes two projects that the author of this thesis has been involved in related to system design. First, the design of an optical pulse shaping system is presented. Thereafter, the feasibility of using a temperature insensitive fibre interferometer as a reference for laser frequency stabilization is discussed.

A.1 Optical pulse shaping system

A UOT system based on spectral hole burning filters should preferably include an optical pulse shaping system that can be used to generate laser pulses with specific intensity and frequency scans. An acousto-optic modulator (AOM) in a double-pass configuration is capable of the required pulse shaping, and such system was therefore designed. The system was designed to be compatible with the group's Ti:sapphire laser (SolsTiS, M Squared Lasers). This means that it must handle a laser power of 3 W, and it should be usable for the full 688 – 990 nm tuning range of the laser. Spectral hole burning setups in UOT are typically bulky, and it is desirable to minimize each part of a set-up. Efforts were therefore made to design a very compact pulse shaping system. Before presenting the system design, a short introduction to AOMs will be given.

A.1.1 Acousto-optic modulators

The basic principles and applications of acousto-optic modulators have been well described in the literature, see, for example, [118]. In an AOM, an RF signal drives a

piezoelectric transducer attached to a crystal, which generates an acoustic wave propagating through the crystal. The acoustic wave periodically alters the reflective index of the crystal. A laser beam incident on this refractive index grating close to the so-called Bragg angle, is diffracted into a pattern of diffraction orders. The efficiency of the diffraction process depends on the RF power delivered to the AOM, and the laser power can therefore be modulated by changing the RF power. A diffraction efficiency into the +1st order beam of above 50% can often be achieved with sufficiently high RF power. Because the refractive index grating is travelling through the crystal, the different diffraction orders will be Doppler-shifted by multiples of the acoustic frequency. The laser frequency can therefore be modulated by changing the acoustic frequency. However, if the acoustic frequency is changed, so is the diffraction angle. For applications where frequency scanning pulses are needed, but spatial beam walk is detrimental, a double-pass configuration can be used. The +1st order diffracted beam is then passed through the AOM a second time, and the change in the direction of the first and second pass cancels out. This also leads to an optical frequency shift of twice the AOM drive frequency.

A.1.2 Double-pass AOM system

Double-pass set-ups can be implemented in a few different ways. For example, the input beam and the twice shifted output beam can be separated using a polarizing beam splitter and a quarter-wave plate [119]. Alternatively, a bow-tie configuration with spatially non-overlapping input and output beams can be used. This approach has frequently been employed in the Quantum Information Group in Lund [120]. However, these bow-tie set-ups have an optical focus inside the AOM, which is not compatible with the Ti:sapphire laser system, as the high laser intensity may damage the AOM. The design was therefore instead based around a modified version of the bow-tie configuration suggested by Lars Rippe, as shown in Figure A.1. A collimated laser beam is sent through the AOM. A lens with a focal length of f is placed at a distance f after the AOM. The beam is focused between two mirrors positioned at a the distance of $f - d/2$ after the lens, where d is the distance between the mirrors. All diffraction orders except for the +1st order are blocked after each pass through the AOM. The bow-tie configuration allows the input an output beams to be separated.

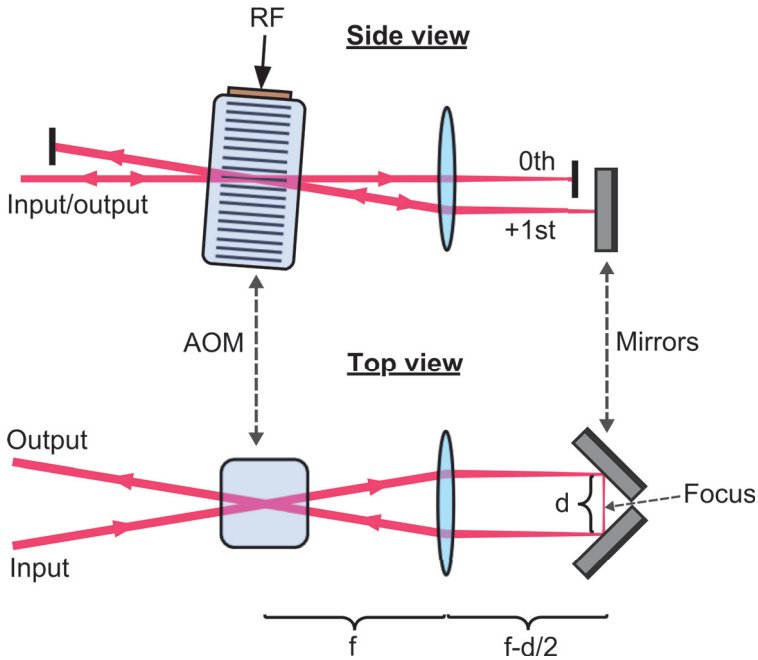

Figure A.1: Schematic of the bow-tie double-pass configuration used in the present work.

A photograph of the top view of the finished double-pass AOM system, where the beam path is indicated by dashed red lines, is shown in Figure A.2. The input and output laser beams are fibre-coupled. The fibres (end-capped PM630-HP FC/APC, Thorlabs) have core-less end-caps to reduce the laser intensity at the air-to-glass interface to avoid fibre damage. Fibre collimators with achromatic lenses (PAF2-A4B, Thorlabs) are used to be compatible with the broad wavelength tuning range of the laser system. The AOM (AOMO 3100-125, Gooch & Housego) has a centre frequency of 100 MHz, and is driven with an RF power of up to 1.2 W. To minimize back-reflections in the coaxial cable a 3 dB attenuator is used before the AOM. An achromatic lens with a focal length of 50 mm is positioned after the AOM and focuses the beam between the two mirrors M1 and M2. A mirror positioned after the lens reflects the 0th order beam into a copper pipe (the beam path is illustrated with the dotted green line in Figure A.2). The full laser power is dumped into this copper pipe when there is no RF signal applied to the AOM. A heat pipe is therefore mounted below the copper pipe and attached to a heat sink to minimize heating of the set-up. A knife blade is positioned between the mirrors M1 and M2 to block the +2nd order diffracted beam. Therefore, only the +1st order diffracted beam reaches mirror M2 and is reflected back through the AOM. An aperture blocks the unwanted diffraction orders after the second pass through the AOM. A polarizer assures a high polarization

purity to the output fibre. A lid can be used to fully enclose the set-up (not shown in Figure A.2). The foot print of the base plate is 12×20 cm^2, which is much smaller than any other double-pass set-up encountered by the author.

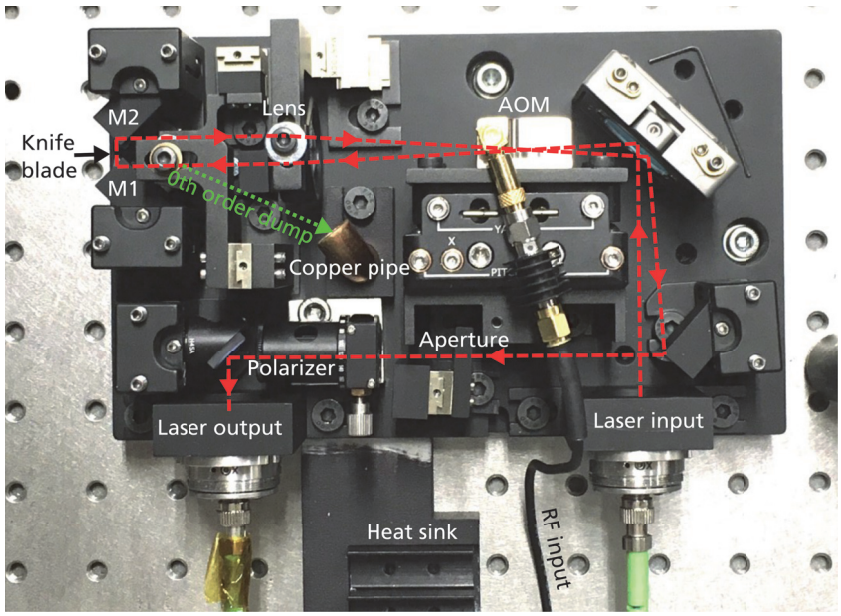

Figure A.2: Photograph of the double-pass AOM system. The approximate beam path is indicated by the dashed red line. The dotted green line indicates the path of the 0th order beam, which is reflected into the copper pipe.

The set-up performance was characterized at an optical wavelength of 690 nm. The peak double-pass efficiency of the AOM was measured as about 70% (at the RF saturation power), and the coupling efficiency to the output fibre was around 65%. The optical frequency was tuned by ±30 MHz before the power out of the output fibre had decreased by a factor of 2.

A.2 Temperature insensitive fibre interferometer

A laser with a narrow linewidth and low drift is required in a UOT system based on spectral hole burning filters. The laser linewidth during the preparation of the UOT filter should ideally be narrower than the homogeneous linewidth of the ions. The laser frequency drift must be significantly less than the bandwidth of the filter during the UOT image acquisition. The Ti:sapphire laser system available in Lund has a short-term linewidth of < 50 kHz, which is sufficient for UOT. However, the frequency drift over second time scales had to be reduced.

An unbalanced fibre interferometer (one interferometer arm is longer than the other) can be used as the reference for laser frequency stabilization [121–123]. This was investigated by Saskia Bondza as part of her Master's thesis project [124], for which I was the co-supervisor. The motivation to investigate a fibre interferometer was that it may potentially be a compact, robust, and low cost set-up.

However, both the refractive index and physical length of optical fibres are sensitive to temperature. The fractional frequency drift $\delta f_L / f_L$ due to temperature of a laser locked to a fibre Mach-Zehnder interferometer is [123]:

$$\delta f_L / f_L = \frac{1}{n_1 l_1 - n_2 l_2} \left[\left(l_1 \frac{\partial n_1}{\partial T} + n_1 \frac{\partial l_1}{\partial T} \right) - \left(l_2 \frac{\partial n_2}{\partial T} + n_2 \frac{\partial l_2}{\partial T} \right) \right] dT \qquad \text{(A.1)}$$

where l_1 and l_2 are the lengths of the fibres in the two interferometer arms, and n_1 and n_2 are the refractive indices of the fibre cores. The frequency fluctuations can be reduced by stabilizing the temperature to minimize dT. However, a 1 mK change in temperature corresponds to a frequency change of a few MHz if identical ordinary single-mode fibres are used in both interferometer arms. Precise temperature control is thus needed to achieve the required sub-MHz frequency drift. Fibres with different thermal sensitivity of the optical path length can also be used to minimize the value inside the brackets, and thus reduce frequency drift due to temperature, which is the approach we chose to investigate.

The optical-path length change with temperature was therefore measured for single-mode fibres with different coatings, and thus different thermal sensitivity. The experimental method had, to our knowledge, not been used previously. The method and measurement results are presented in **Paper II**.

Fibres with straight cleaved ends were used as low-finesse cavities. The reflectance from the fibre ends is ~ 3%, yielding a finesse of ~ 0.6. The fibre length was measured. Light was coupled into the fibre, which was placed in a thermally insulated box. The ambient temperature of the box was ramped, and the almost sinusoidal interference fringes observed in the light reflected from the fibre due to the change in optical path length were recorded, and used to derive the thermal sensitivity of the optical path length.

Measurements results of the change in the optical path length with temperature for single acrylate, dual acrylate, copper, and aluminium coated fibres were presented. In particular, the results showed that the optical path length of aluminium coated fibres (AIS4.3/125/175A, Fiberguide Industries) was a factor of 1.88 more sensitive to temperature compared to single acrylate coated fibres (630HP, Thorlabs). An unbalanced fibre interferometer with an optical-path difference that is insensitive to temperature fluctuations may thus be constructed by using an aluminium coated fibre in the short

arm, and a single acrylate coated fibre in the long arm of the interferometer. The length of the long arm should be a factor of 1.88 longer than the short arm.

Since the optical components required to construct such temperature insensitive interferometer operating over the full 688 – 990 nm tuning range of our Ti:sapphire laser are not currently available, the scheme was not further investigated. Further details can be found in the thesis by Saskia Bondza [124].

References

[1] J. P. Culver, V. Ntziachristos, M. J. Holboke, and A. G. Yodh. Optimization of optode arrangements for diffuse optical tomography: A singular-value analysis. *Opt. Lett.*, 26(10):701–703, 2001.

[2] L. V. Wang and S. Hu. Photoacoustic Tomography: In Vivo Imaging from Organelles to Organs. *Science*, 335(6075):1458–1462, 2012.

[3] L. Lin, P. Hu, C. M. Appleton, K. Maslov, L. Li, R. Zhang, and L. V. Wang. Single-breath-hold photoacoustic computed tomography of the breast. *Nature Communications*, 9:2352, 2018.

[4] S. Na, J. J. Russin, L. Lin, X. Yuan, P. Hu, K. B. Jann, L. Yan, K. Maslov, J. Shi, D. J. Wang, C. Y. Liu, and L. V. Wang. Massively parallel functional photoacoustic computed tomography of the human brain. *Nature Biomedical Engineering*, 453:1–9, 2021.

[5] J. Gunther and S. Andersson-Engels. Review of current methods of acousto-optical tomography for biomedical applications. *Front. Optoelectron.*, 10:211–238, 2017.

[6] D. S. Elson, R. Li, C. Dunsby, R. Eckersley, and M.-X. Tang. Ultrasound-mediated optical tomography: a review of current methods. *Interface Focus*, 1: 632–648, 2011.

[7] A. Walther, L. Rippe, L. V. Wang, S. Andersson-Engels, and S. Kröll. Analysis of the potential for non-invasive imaging of oxygenation at heart depth, using ultrasound optical tomography (UOT) or photo-acoustic tomography (PAT). *Biomed. Opt. Express*, 8(10):4523–4536, 2017.

[8] Y. Liu, R. Cao, J. Xu, H. Ruan, and C. Yang. Imaging through highly scattering human skulls with ultrasound-modulated optical tomography. *Opt. Lett.*, 45 (11):2973–2976, 2020.

[9] H. Zhang, M. Sabooni, L. Rippe, C. Kim, S. Kröll, L. V. Wang, and P. R. Hemmer. Slow light for deep tissue imaging with ultrasound modulation. *Applied Physics Letters*, 100:131102, 2012.

[10] A. Kinos, Q. Li, L. Rippe, and S. Kröll. Development and characterization of high suppression and high étendue narrowband spectral filters. *Appl. Opt.*, 55: 10442–10448, 2016.

[11] S. L. Jacques. Optical properties of biological tissues: a review. *Physics in Medicine and Biology*, 58(11):R37–R61, 2013.

[12] L. A. Sordillo, Y. Pu, S. Pratavieira, Y. Budansky, and R. R. Alfano. Deep optical imaging of tissue using the second and third near-infrared spectral windows. *Journal of Biomedical Optics*, 19(5):1 – 6, 2014.

[13] S. Prahl. Optical Absorption of Hemoglobin. 1999. URL `http://omlc.ogi.edu/spectra/hemoglobin/`.

[14] G. M. Hale and M. R. Querry. Optical constants of water in the 200-nm to 200-μm wavelength region. *Appl. Opt.*, 12(3):555–563, 1973.

[15] S. Prahl. Light Absorption by Water. 2017. URL `https://omlc.org/spectra/water/`.

[16] S.-R. Kothapalli, S. Sakadzic, C. Kim, and L. V. Wang. Imaging optically scattering objects with ultrasound-modulated optical tomography. *Opt. Lett.*, 32(16):2351–2353, 2007.

[17] M. Gross, P. Goy, B. C. Forget, M. Atlan, F. Ramaz, A. C. Boccara, and A. K. Dunn. Heterodyne detection of multiply scattered monochromatic light with a multipixel detector. *Opt. Lett.*, 30(11):1357–1359, 2005.

[18] M. M. Qureshi, J. Brake, H.-J. Jeon, H. Ruan, Y. Liu, A. M. Safi, T. J. Eom, C. Yang, and E. Chung. In vivo study of optical speckle decorrelation time across depths in the mouse brain. *Biomed. Opt. Express*, 8(11):4855–4864, 2017.

[19] D. D. Duncan, S. J. Kirkpatrick, and R. K. Wang. Statistics of local speckle contrast. *J. Opt. Soc. Am. A*, 25(1):9–15, 2008.

[20] D. A. Boas and A. K. Dunn. Laser speckle contrast imaging in biomedical optics. *Journal of Biomedical Optics*, 15(1):1 – 12, 2010.

[21] K. H. Wedepohl. The composition of the continental crust. *Geochimica et Cosmochimica Acta*, 59(7):1217–1232, 1995.

[22] A. Kinos. *Light-Matter Interaction and Quantum Computing in Rare-Earth-Ion-Doped Crystals*. Ph.D. thesis, Lund University, 2018.

[23] A. Kinos, D. Hunger, R. Kolesov, K. Mølmer, H. de Riedmatten, P. Goldner, A. Tallaire, L. Morvan, P. Berger, S. Welinski, et al. Roadmap for rare-earth quantum computing. *arXiv preprint arXiv:2103.15743*, 2021.

[24] S. P. Horvath, C. Shi, D. Gustavsson, A. Walther, A. Kinos, S. Kröll, and L. Rippe. Slow light frequency reference cavities - proof of concept for reducing the frequency sensitivity due to length fluctuations. *New Journal of Physics*, 2022.

[25] S. Cook, T. Rosenband, and D. R. Leibrandt. Laser-Frequency Stabilization Based on Steady-State Spectral-Hole Burning in Eu^{3+}:Y_2SiO_5. *Phys. Rev. Lett.*, 114:253902, 2015.

[26] L. Ménager, I. Lorgeré, J.-L. Le Gouët, D. Dolfi, and J.-P. Huignard. Demonstration of a radio-frequency spectrum analyzer based on spectral hole burning. *Opt. Lett.*, 26(16):1245–1247, 2001.

[27] Y. Li, P. Hemmer, C. Kim, H. Zhang, and L. V. Wang. Detection of ultrasound-modulated diffuse photons using spectral-hole burning. *Opt. Express*, 16:314862–14874, 2008.

[28] Y. Li, H. Zhang, C. Kim, K. H. Wagner, P. Hemmer, and L. V. Wang. Pulsed ultrasound-modulated optical tomography using spectral-hole burning as a narrowband spectral filter. *Applied Physics Letter*, 93:011111, 2008.

[29] C. Venet, M. Bocoum, J.-B. Laudereau, T. Chaneliere, F. Ramaz, and A. Louchet-Chauvet. Ultrasound-modulated optical tomography in scattering media: flux filtering based on persistent spectral hole burning in the optical diagnosis window. *Opt. Lett.*, 43:3993–3996, 2018.

[30] R. Hull, J. Parisi, R. M. Osgood Jr., H. Warlimont, G. Liu, and B. Jacquier. *Spectroscopic Properties of Rare Earths in Optical Materials*. Springer, 2005.

[31] R. W. Equall, Y. Sun, R. L. Cone, and R. M. Macfarlane. Ultraslow optical dephasing in Eu^{3+}:Y_2SiO_5. *Phys. Rev. Lett.*, 72:2179–2182, 1994.

[32] T. Böttger, C. W. Thiel, R. L. Cone, and Y. Sun. Effects of magnetic field orientation on optical decoherence in Er^{3+}:Y_2SiO_5. *Phys. Rev. B*, 79:115104, 2009.

[33] J. M. Kindem, J. G. Bartholomew, P. J. T. Woodburn, T. Zhong, I. Craiciu, R. L. Cone, C. W. Thiel, and A. Faraon. Characterization of $^{171}Yb^{3+}$:YVO_4 for photonic quantum technologies. *Phys. Rev. B*, 98:024404, 2018.

[34] F. Könz, Y. Sun, C. W. Thiel, R. L. Cone, R. W. Equall, R. L. Hutcheson, and R. M. Macfarlane. Temperature and concentration dependence of optical dephasing, spectral-hole lifetime, and anisotropic absorption in Eu^{3+}:Y_2SiO_5. *Phys. Rev. B*, 68:085109, 2003.

[35] R. Oswald, M. G. Hansen, E. Wiens, A. Y. Nevsky, and S. Schiller. Characteristics of long-lived persistent spectral holes in Eu^{3+}:Y_2SiO_5 at 1.2 K. *Phys. Rev. A*, 98:062516, 2018.

[36] L. Vestergaard Hau, S. E. Harris, Z. Dutton, and C. H. Behrooz. Light speed reduction to 17 metres per second in an ultracold atomic gas. *Nature*, 397: 594—598, 1999.

[37] M. M. Kash, V. A. Sautenkov, A. S. Zibrov, L. Hollberg, G. R. Welch, M. D. Lukin, Y. Rostovtsev, E. S. Fry, and M. O. Scully. Ultraslow group velocity and enhanced nonlinear optical effects in a coherently driven hot atomic gas. *Phys. Rev. Lett.*, 82:5229–5232, 1999.

[38] R. W. Boyd, D. J. Gauthier, and A. L. Gaeta. Applications of Slow Light in Telecommunications. *Opt. Photon. News*, 17(4):18–23, 2006.

[39] J. S. Toll. Causality and the dispersion relation: Logical foundations. *Phys. Rev.*, 104:1760–1770, 1956.

[40] C. Kittel and P. McEuen. *Kittel's Introduction to Solid State Physics*. John Wiley & Sons, 2018.

[41] A. D. Marsh. *Exploration of Rare-Earth Ion Transitions and Host Materials for Spectral Hole Burning Applications and Quantum Information Science*. Ph.D. thesis, Montana State University, 2021.

[42] Y. V. Orlovskii, R. J. Reeves, R. C. Powell, T. T. Basiev, and K. K. Pukhov. Multiple-phonon nonradiative relaxation: Experimental rates in fluoride crystals doped with Er^{3+} and Nd^{3+} ions and a theoretical model. *Phys. Rev. B*, 49: 3821–3830, 1994.

[43] F. S. Ermeneux, C. Goutaudier, R. Moncorgé, Y. Sun, R. L. Cone, E. Zannoni, E. Cavalli, and M. Bettinelli. Multiphonon relaxation in YVO_4 single crystals. *Phys. Rev. B*, 61:3915–3921, 2000.

[44] F. Auzel. A fundamental self-generated quenching center for lanthanide-doped high-purity solids. *Journal of Luminescence*, 100(1):125–130, 2002.

[45] F. A. Marks, H. W. Tomlinson, and G. W. Brooksby. Comprehensive approach to breast cancer detection using light: photon localization by ultrasound modulation and tissue characterization by spectral discrimination. In *Photon Migration and Imaging in Random Media and Tissues*, volume 1888, pages 500 – 510. International Society for Optics and Photonics, SPIE, 1993.

[46] L. Wang and X. Zhao. Ultrasound-modulated optical tomography of absorbing objects buried in dense tissue-simulating turbid media. *Appl. Opt.*, 36:7277–7282, 1997.

[47] M. Kempe, M. Larionov, D. Zaslavsky, and A. Z. Genack. Acousto-optic tomography with multiply scattered light. *J. Opt. Soc. Am. A*, 14:1151–1158, 1997.

[48] S. Lévêque, A. C. Boccara, M. Lebec, and H. Saint-Jalmes. Ultrasonic tagging of photon paths in scattering media: parallel speckle modulation processing. *Opt. Lett.*, 24(3):181–183, 1999.

[49] J. Li, G. Ku, and L. V. Wang. Ultrasound-modulated optical tomography of biological tissue by use of contrast of laser speckles. *Appl. Opt.*, 41(28):6030–6035, 2002.

[50] L. J. Nowak and W. Steenbergen. Reflection-mode acousto-optic imaging using a one-dimensional ultrasound array with electronically scanned focus. *Journal of Biomedical Optics*, 25(9):1 – 14, 2020.

[51] Y. Liu, Y. Shen, C. Ma, J. Shi, and L. V. Wang. Lock-in camera based heterodyne holography for ultrasound-modulated optical tomography inside dynamic scattering media. *Applied Physics Letters*, 108(23):231106, 2016.

[52] T. W. Murray, L. Sui, G. Maguluri, R. A. Roy, A. Nieva, F. Blonigen, and C. A. DiMarzio. Detection of ultrasound-modulated photons in diffuse media using the photorefractive effect. *Opt. Lett.*, 29(21):2509–2511, 2004.

[53] F. Ramaz, B. C. Forget, M. Atlan, A. C. Boccara, M. Gross, P. Delaye, and G. Roosen. Photorefractive detection of tagged photons in ultrasound modulated optical tomography of thick biological tissues. *Opt. Express*, 12(22):5469–5474, 2004.

[54] P. Lai, X. Xu, and L. V. Wang. Ultrasound-modulated optical tomography at new depth. *Journal of Biomedical Optics*, 17(6):1 – 6, 2012.

[55] S. Sakadžić and L. V. Wang. High-resolution ultrasound-modulated optical tomography in biological tissues. *Opt. Lett.*, 29(23):2770–2772, 2004.

[56] G. Rousseau, A. Blouin, and J.-P. Monchalin. Ultrasound-modulated optical imaging using a high-power pulsed laser and a double-pass confocal Fabry–Perot interferometer. *Opt. Lett.*, 34(21):3445–3447, 2009.

[57] S. G. Resink and W. Steenbergen. Tandem-pulsed acousto-optics: an analytical framework of modulated high-contrast speckle patterns. *Physics in Medicine and Biology*, 60(11):4371–4382, 2015.

[58] Y. Suzuki, P. Lai, X. Xu, and L. Wang. High-sensitivity ultrasound-modulated optical tomography with a photorefractive polymer. *Opt. Lett.*, 38(6):899–901, 2013.

[59] M. Gross, M. Lesaffre, F. Ramaz, P. Delaye, G. Roosen, and A. C. Boccara. Detection of the tagged or untagged photons in acousto-optic imaging of thick highly scattering media by photorefractive adaptive holography. *Eur Phys J E Soft Matter*, 28:173–182, 2009.

[60] L. Sui, R. A. Roy, C. A. DiMarzio, and T. W. Murray. Imaging in diffuse media with pulsed-ultrasound-modulated light and the photorefractive effect. *Appl. Opt.*, 44(19):4041–4048, 2005.

[61] S. Farahi, G. Montemezzani, A. A. Grabar, J.-P. Huignard, and F. Ramaz. Photorefractive acousto-optic imaging in thick scattering media at 790 nm with a $Sn_2P_2S_6$:Te crystal. *Opt. Lett.*, 35(11):1798–1800, 2010.

[62] D. Hill. Tagged light simulator. Bitbucket (2021) [retrieved 17 March 2022], `https://bitbucket.org/qilund/tagged-light-simulator`.

[63] Y. Huang, M. Cua, J. Brake, Y. Liu, and C. Yang. Investigating ultrasound–light interaction in scattering media. *Journal of Biomedical Optics*, 25(2):1 – 12, 2020.

[64] S. A. Prahl. A Monte Carlo model of light propagation in tissue. In *Dosimetry of Laser Radiation in Medicine and Biology*, volume 10305, pages 105 – 114. International Society for Optics and Photonics, SPIE, 1989.

[65] A. N. S. I. Standard, Z136. 1. American National Standard for the Safe Use of Lasers, American National Standards Institute, Inc., New York, 1993.

[66] Y. Liu, P. Lai, C. Ma, X. Xu, A. A. Grabar, and L. V. Wang. Optical focusing deep inside dynamic scattering media with near-infrared time-reversed ultrasonically encoded (TRUE) light. *Nat Communications*, 6:5904, 2015.

[67] R. Beach, M. D. Shinn, L. Davis, R. W. Solarz, and W. F. Krupke. Optical absorption and stimulated emission of neodymium in yttrium orthosilicate. *IEEE Journal of Quantum Electronics*, 26(8):1405–1412, 1990.

[68] R. W. Equall, R. L. Cone, and R. M. Macfarlane. Homogeneous broadening and hyperfine structure of optical transitions in Pr^{3+}:Y_2SiO_5. *Phys. Rev. B*, 52: 3963–3969, 1995.

[69] K. Holliday, M. Croci, E. Vauthey, and U. P. Wild. Spectral hole burning and holography in an Pr^{3+}:Y_2SiO_5 crystal. *Phys. Rev. B*, 47:14741–14752, 1993.

[70] Y. Sun. *Spectroscopic Properties of Rare Earths in Optical Materials Chapter 7*. Springer Series in Material Science, 2005.

[71] M. Tian, T. Chang, K. D. Merkel, and W. Randall. Reconfiguration of spectral absorption features using a frequency-chirped laser pulse. *Appl. Opt.*, 50(36): 6548–6554, 2011.

[72] M. Di. *Preparation of Materials for Deep Tissue Imaging with Slow Light*. Master's thesis, Lund University, 2018.

[73] R. Cubeddu, A. Pifferi, P. Taroni, A. Torricelli, and G. Valentini. A solid tissue phantom for photon migration studies. *Physics in Medicine and Biology*, 42(10): 1971–1979, 1997.

[74] D. Khoptyar, A. A. Subash, S. Johansson, M. Saleem, A. Sparén, J. Johansson, and S. Andersson-Engels. Broadband photon time-of-flight spectroscopy of pharmaceuticals and highly scattering plastics in the VIS and close NIR spectral ranges. *Opt. Express*, 21(18):20941–20953, 2013.

[75] L. Spinelli, M. Botwicz, N. Zolek, M. Kacprzak, D. Milej, P. Sawosz, A. Liebert, U. Weigel, T. Durduran, F. Foschum, A. Kienle, F. Baribeau, S. Leclair, J.-P. Bouchard, I. Noiseux, P. Gallant, O. Mermut, A. Farina, A. Pifferi, A. Torricelli, R. Cubeddu, H.-C. Ho, M. Mazurenka, H. Wabnitz, K. Klauenberg, O. Bodnar, C. Elster, M. Bénazech-Lavoué, Y. Bérubé-Lauzière, F. Lesage, D. Khoptyar, A. A. Subash, S. Andersson-Engels, P. Di Ninni, F. Martelli, and G. Zaccanti. Determination of reference values for optical properties of liquid phantoms based on intralipid and india ink. *Biomed. Opt. Express*, 5(7):2037–2053, 2014.

[76] L. V. Wang. Rapid modeling of diffuse reflectance of light in turbid slabs. *J. Opt. Soc. Am. A*, 15(4):936–944, 1998.

[77] P. Taroni, G. Quarto, A. Pifferi, F. Abbate, N. Balestreri, S. Menna, E. Cassano, and R. Cubeddu. Breast tissue composition and its dependence on demographic risk factors for breast cancer: Non-invasive assessment by time domain diffuse optical spectroscopy. *PLOS ONE*, 10:1–16, 2015.

[78] X. Xu, H. Liu, and L. V. Wang. Improving the imaging ability of ultrasound-modulated optical tomography with spectral-hole burning. In *Advances in Photonics of Quantum Computing, Memory, and Communication IV*, volume 7948, pages 9 – 16. International Society for Optics and Photonics, SPIE, 2011.

[79] C. Kim, K. H. Song, K. Maslov, and L. V. Wang. Ultrasound-modulated optical tomography in reflection mode with ring-shaped light illumination. *Journal of Biomedical Optics*, 14(2):1 – 3, 2009.

[80] S. Powell, S. R. Arridge, and T. S. Leung. Gradient-based quantitative image reconstruction in ultrasound-modulated optical tomography: First Harmonic Measurement Type in a Linearised Diffusion Formulation. *IEEE Transactions on Medical Imaging*, 35(2):456–467, 2016.

[81] H. Sung, J. Ferlay, R. L. Siegel, M. Laversanne, I. Soerjomataram, A. Jemal, and F. Bray. Global Cancer Statistics 2020: GLOBOCAN Estimates of Incidence and Mortality Worldwide for 36 Cancers in 185 Countries. *CA: A Cancer Journal for Clinicians*, 71(3):209–249, 2021.

[82] B. J. Tromberg, N. Shah, R. Lanning, A. Cerussi, J. Espinoza, T. Pham, L. Svaasand, and J. Butler. Non-Invasive In Vivo Characterization of Breast Tumors Using Photon Migration Spectroscopy. *Neoplasia*, 2(1):26–40, 2000.

[83] D. Grosenick, H. Wabnitz, K T. Moesta, J. Mucke, P. M. Schlag, and H. Rinneberg. Time-domain scanning optical mammography: II. optical properties and tissue parameters of 87 carcinomas. *Physics in Medicine and Biology*, 50(11): 2451–2468, 2005.

[84] S. Na and L. V. Wang. Photoacoustic computed tomography for functional human brain imaging. *Biomed. Opt. Express*, 12(7):4056–4083, 2021.

[85] X. Xu, S.-R. Kothapalli, H. Liu, and L. V. Wang. Spectral hole burning for ultrasound-modulated optical tomography of thick tissue. *J. Biomed. Opt.*, 15: 066018, 2010.

[86] W. T. Carnall, H. Crosswhite, and H. M. Crosswhite. Energy level structure and transition probabilities in the spectra of the trivalent lanthanides in LaF_3. Technical report, Argonne National Lab.(ANL), Argonne, IL (United States), 1978.

[87] W. T. Carnall, G. L. Goodman, K. Rajnak, and R. S. Rana. A systematic analysis of the spectra of the lanthanides doped into single crystal LaF_3. *The Journal of Chemical Physics*, 90(7):3443–3457, 1989.

[88] E. Zambrini Cruzeiro, A. Tiranov, I. Usmani, C. Laplane, J. Lavoie, A. Ferrier, P. Goldner, N. Gisin, and M. Afzelius. Spectral hole lifetimes and spin population relaxation dynamics in neodymium-doped yttrium orthosilicate. *Phys. Rev. B*, 95:205119, 2017.

[89] S. R. Hastings-Simon, M. Afzelius, J. Minář, M. U. Staudt, B. Lauritzen, H. de Riedmatten, N. Gisin, A. Amari, A. Walther, S. Kröll, E. Cavalli, and M. Bettinelli. Spectral hole-burning spectroscopy in Nd^{3+}:YVO_4. *Phys. Rev. B*, 77:125111, 2008.

[90] Y. Sun, C. W. Thiel, R. L. Cone, R. W. Equall, and R. L. Hutcheson. Recent progress in developing new rare earth materials for hole burning and coherent transient applications. *Journal of Luminescence*, 98(1):281–287, 2002. Proceedings of the Seventh International Meeting on Hole Burning, Single Molecules and Related Spectroscopies: Science and Applications.

[91] M. Afzelius, M. U. Staudt, H. de Riedmatten, N. Gisin, O. Guillot-Noël, P. Goldner, R. Marino, P. Porcher, E. Cavalli, and M. Bettinelli. Efficient optical pumping of zeeman spin levels in Nd^{3+}:YVO_4. *Journal of Luminescence*, 130(9):1566–1571, 2010.

[92] P.-J. Liang, X. Liu, P.-Y. Li, Z.-Q. Zhou, C.-.F Li, and G.-C. Guo. Spectroscopic investigations of $^{142}Nd^{3+}$:YVO_4 for quantum memory applications. *J. Opt. Soc. Am. B*, 37(6):1653–1658, 2020.

[93] E. Zambrini Cruzeiro, A. Tiranov, J. Lavoie, A. Ferrier, P. Goldner, N. Gisin, and M. Afzelius. Efficient optical pumping using hyperfine levels in $^{145}Nd^{3+}$:Y_2SiO_5 and its application to optical storage. *New Journal of Physics*, 20(5):053013, 2018.

[94] A. Abragam and B. Bleaney. Enhanced nuclear magnetism: some novel features and prospective experiments. *Proceedings of the Royal Society of London. A. Mathematical and Physical Sciences*, 387(1793):221–256, 1983.

[95] L. Veissier, C. W. Thiel, T. Lutz, P. E. Barclay, W. Tittel, and R. L. Cone. Quadratic zeeman effect and spin-lattice relaxation of Tm^{3+}:YAG at high magnetic fields. *Phys. Rev. B*, 94:205133, 2016.

[96] C. Venet, B. Car, L. Veissier, F. Ramaz, and A. Louchet-Chauvet. Deep and persistent spectral holes in thulium-doped yttrium orthosilicate for imaging applications. *Phys. Rev. B*, 99:115102, 2019.

[97] A. Louchet, J. S. Habib, V. Crozatier, I. Lorgeré, F. Goldfarb, F. Bretenaker, J.-L. Le Gouët, O. Guillot-Noël, and Ph. Goldner. Branching ratio measurement

of a Λ system in Tm^{3+}:YAG under a magnetic field. *Phys. Rev. B*, 75:035131, 2007.

[98] T. Chanelière, J. Ruggiero, M. Bonarota, M. Afzelius, and J-L Le Gouët. Efficient light storage in a crystal using an atomic frequency comb. *New Journal of Physics*, 12(2):023025, 2010.

[99] R. M. Macfarlane. Photon-echo measurements on the trivalent thulium ion. *Opt. Lett.*, 18(22):1958–1960, 1993.

[100] J.-B. Laudereau. *Acousto-optic imaging : challenges of in vivo imaging*. Ph.D. thesis, Université Pierre et Marie Curie - Paris VI, 2016.

[101] R. W. Equall. *Photon echo studies of rare-earth-activated materials for optical memory and signal processing devices*. Ph.D. thesis, Montana State University, 1995.

[102] C. W. Thiel, Y. Sun, T. Böttger, W. R. Babbitt, and R. L. Cone. Optical decoherence and persistent spectral hole burning in Tm^{3+}:$LiNbO_3$. *Journal of Luminescence*, 130(9):1598–1602, 2010.

[103] Y. Sun, C. W. Thiel, and R. L. Cone. Optical decoherence and energy level structure of 0.1%Tm^{3+}:$LiNbO_3$. *Phys. Rev. B*, 85:165106, 2012.

[104] R. M. Macfarlane and M. J. Dejneka. Spectral hole burning in thulium-doped glass ceramics. *Opt. Lett.*, 26(7):429–431, 2001.

[105] N. M. Strickland and G. D. Jones. Site-selective spectroscopy of Tm^{3+} centers in CaF_2:Tm^{3+}. *Phys. Rev. B*, 56:10916–10929, 1997.

[106] A. Zalkin, D. H. Templeton, and T. E. Hopkins. The atomic parameters in the lanthanum trifluoride structure. *Inorganic Chemistry*, 5(8):1466–1468, 1966.

[107] R. M. Macfarlane. Spectral hole burning in the trivalent thulium ion. *Opt. Lett.*, 18(10):829–831, 1993.

[108] W. T. Carnall, P. R. Fields, J. Morrison, and R. Sarup. Absorption Spectrum of Tm^{3+}:LaF_3. *The Journal of Chemical Physics*, 52(8):4054–4059, 1970.

[109] J. Hong, L. Zhang, M. Xu, and Y. Hang. Optical characterization of Tm^{3+} in LaF_3 single crystal. *Infrared Physics and Technology*, 82:50–55, 2017.

[110] D. S. Vega, P. B. Rambow, and M. Tian. Optical nutation in an optically thick and inhomogeneously broadened atomic ensemble. *J. Opt. Soc. Am. B*, 35(6): 1374–1378, 2018.

[111] G. Grynberg, A. Aspect, and C. Fabre. *Introduction to quantum optics: from the semi-classical approach to quantized light*. Cambridge university press, 2010.

[112] D. E. McCumber and M. D. Sturge. Linewidth and Temperature Shift of the R Lines in Ruby. *Journal of Applied Physics*, 34(6):1682–1684, 1963.

[113] R. M. Macfarlane. Direct process thermal line broadening in Tm:YAG. *Journal of Luminescence*, 85(4):181–186, 2000.

[114] T. Böttger, C. W. Thiel, R. L. Cone, Y. Sun, and A. Faraon. Optical spectroscopy and decoherence studies of Yb^{3+}:YAG at 968 nm. *Phys. Rev. B*, 94: 045134, 2016.

[115] S. Huang, S. T. Lai, L. Lou, W. Jia, and W. M. Yen. Upconversion in LaF_3: Tm^{3+}. *Phys. Rev. B*, 24:59–63, 1981.

[116] R. Wannemacher, R. M. Macfarlane, Y. P. Wang, D. Sox, D. Boye, and R. S. Meltzer. Nuclear spin-flip sidebands in optical spectral holeburning and fluorescence line narrowing of the Er^{3+} ion. *Journal of Luminescence*, 48-49:309–312, 1991.

[117] R. K. Harris, E. D. Becker, S. M. Cabral de Menezes, R. Goodfellow, and P. Granger. NMR nomenclature. Nuclear spin properties and conventions for chemical shifts (IUPAC Recommendations 2001). *Pure Appl. Chem.*, 73(11): 1795–1818, 2001.

[118] B. E. Saleh and M. C. Teich. *Fundamentals of photonics*. John Wiley & sons, 2019.

[119] E. A. Donley, T. P. Heavner, F. Levi, M. O. Tataw, and S. R. Jefferts. Double-pass acousto-optic modulator system. *Review of Scientific Instruments*, 76(6): 063112, 2005.

[120] L. Rippe. *Quantum computing with naturally trapped sub-nanometre-spaced ions*. Ph.D. thesis, Lund University, 2006.

[121] J. Kong, V. G. Lucivero, R. Jiménez-Martínez, and M. W. Mitchell. Long-term laser frequency stabilization using fiber interferometers. *Review of Scientific Instruments*, 86(7):073104, 2015.

[122] F. Kéfélian, H. Jiang, P. Lemonde, and G. Santarelli. Ultralow-frequency-noise stabilization of a laser by locking to an optical fiber-delay line. *Opt. Lett.*, 34 (7):914–916, 2009.

[123] Y. T. Chen. Use of single-mode optical fiber in the stabilization of laser frequency. *Appl. Opt.*, 28(11):2017–2021, 1989.

[124] S. Bondza. *Design of a Temperature Insensitive Fiber Interferometer for Long-Term Laser Frequency Stabilization using Metal Coated Fibers*. Master's thesis, Lund University, 2019.

Scientific publications

Author contributions

Paper I: Characterization and modeling of acousto-optic signal strengths in highly scattering media

David Hill and I performed the main UOT experiments together (I did not participate in the ultrasound and phantom characterization). I analyzed the experimental data. I wrote most of the manuscript.

Paper II: A simple experimental method for measuring the thermal sensitivity of single-mode fibers

I suggested that we should investigate using an optical fiber interferometer as the reference for stabilizing the frequency of our UOT laser system. This lead to a Master's project by Saskia Bondza, for which I was the co-supervisor. Saskia did all the experimental work. I contributed to discussions regarding the analysis, and manuscript.

Paper III: Acousto-optic interaction strengths in optically scattering media using high pressure acoustic pulses

David Hill and I performed the experiments together. David did all the theoretical modelling and experimental data analysis. I contributed to discussions regarding the analysis, and the manuscript.

Paper IV: First principle simulation package for arbitrary acousto-optic interaction in scattering materials

David Hill and I performed the experiments together. David did the analysis and wrote the manuscript.

Paper V: Suppression of Non-Radiative Relaxation in Tm^{3+}-doped Materials for Oxygenation-Sensitive Ultrasound-Optical Tomography

I suggested that Tm^{3+} :LaF_3 could be an interesting candidate for UOT filtering. I visited the Cone and Thiel lab and took part in the experiments on Tm^{3+} :LaF_3. I contributed to discussions regarding the analysis, and the manuscript.

Paper VI: Comparison of contrast-to-noise ratios of different detection methods in ultrasound optical tomography

I analyzed the contrast-to-noise ratio of the detection methods. I wrote the manuscript. David Hill performed the Monte-Carlo simulations.

Printed by Media-Tryck, Lund 2022 NORDIC SWAN ECOLABEL 3041 0903

LUND UNIVERSITY
Faculty of Engineering, LTH
Department of Physics
Division of Atomic Physics

ISBN 978-91-8039-224-2 (print)
978-91-8039-223-5 (pdf)
ISSN 0281-2762
Lund Reports on Atomic Physics, LRAP 580 (2022)